Torsional Properties of DNA Probed with Magnetic (Torque) Tweezers

Franziska Kriegel

Dissertation
an der Fakultät für Physik
der Ludwig–Maximilians–Universität
München

vorgelegt von
Franziska Kriegel
aus Erlangen

München, den 6. Oktober 2017

Erstgutachter: Prof. Dr. Jan Lipfert
Zweitgutachter: Prof. Dr. Martin Zacharias
Tag der mündlichen Prüfung: 7.12.2017

Zusammenfassung

Die Natur hat eine einzigartige Struktur entwickelt um die DNS, unser Erbgut, zu schützen und zu übertragen. Für die Entdeckung dieser komplexen Struktur wurde 1962 der Nobelpreis vergeben. Die DNS trägt die Information unseres Erbguts in ihrer Sequenz. Die sich im Inneren der DNS befindlichen Basen charakterisieren das Genom und sind geschützt durch das doppelsträngige Rückgrat. Um auf die Information zurückgreifen zu können, muss die Doppelhelix geöffnet, sozusagen entwunden werden. Für diesen Vorgang müssen Drehkräfte wirken. Aus diesem Grund werden biologische Prozesse, wie Replikation und Transkription, durch Drehmomente reguliert. Die Topologie, die eine DNS annimmt, ist daher für das Leben essentiell und zudem streng reguliert durch eine Gruppe von Enzymen – den Topoisomerasen. Topoisomerasen sind so bedeutsam, dass ihre Entnahme aus der Zelle, nach kurzer Zeit den Zelltod zur Folge hat. Dieses Verfahren wird in der Medizin oft angewendet, um Krebszellen zu bekämpfen und zu töten. Folglich ist es von herausragender Bedeutung, das Verhalten von DNS unter der Wirkung von Drehkräften zu untersuchen und zu verstehen. Einige Einzelmolekültechniken wurden in den letzten Jahren entwickelt, um an Molekülen im pN Bereich zu ziehen oder zu drehen. Verhältnismäßig neu ist die Möglichkeit das Drehmoment einzelner Moleküle, unter anderem der DNS, direkt zu messen. Die *Magnetische Pinzette* ist hierbei die prominenteste Technik.

Bisher konnte man bei direkten Drehmomentmessungen nur je ein Molekül nach dem anderen studieren. Diese Einzelbetrachtung erschwert das Erheben von Statistiken ungemein. In dieser Arbeit stelle ich eine vereinfachte und temperaturkontrollierte Version der *Magnetischen Pinzette* vor, die außerdem mehrere Moleküle gleichzeitig messen kann, um Dreheigenschaften der DNS zu untersuchen. Ich zeige, dass sowohl die *Frei Drehbaren Magnetischen Pinzetten* als auch die *Magnetischen Drehmoment Pinzetten*, unter den richtigen Bedingungen – zum Beispiel den magnetischen Kugeln – für parallele Messungen verwendet werden können. Außerdem zeige ich, dass die Kraftkalibrierungen in beiden Verfahren gleich sind. Dieser Umstand erlaubt es, diese direkt in den *Magnetischen Drehmoment Pinzetten* anzuwenden ohne vorab die *Frei Drehbaren Magnetischen Pinzetten* zu etablieren. Mit diesen Ergebnissen habe ich eine multiple Form der *Magnetischen Drehmoment Pinzette* entwickelt und somit Ausdehnungs- und Drehmomentmessungen von DNS gemacht, die eine Untersuchung der Struktur des Moleküls ermöglichen. Der Einfluss von äußeren Faktoren, wie zum Beispiel der Salzgehalt oder die Temperatur auf Dreheigenschaften des Moleküls, sind höchst relevant für biologische Prozesse. Mit den vorab genannten Ergebnissen und Verbesserungen in der Technik habe ich diese Fragestellungen systematisch genau untersucht. Zuerst habe ich die intrinsische Drehsteifigkeit (bei großen Zugkräften, die Biegeeffekte unterdrücken) der DNS unter verschiedenen Salzkonzentrationen analysiert. Ein Ergebnis dieser Untersuchung ist, dass diese salzunabhängig ist. Die effektive Drehsteifigkeit wird bei kleineren Zugkräften gemessen, sodass Drehenergie in Biegeenergie übergeht. Die effektive Drehsteifigkeit nimmt mit erhöhter Salzkonzentration ab, was allerdings als reiner Biegeeffekt verstanden wird. Dieselben Daten konnten wir mit Molekulardynamischen Simulationen vergleichen und kommen zu dem Schluss, dass das Modell der asymmetrischen, anisotropischen, drehbaren, wurmartigen Kette, die beste Übereinstimmung liefert. Die salzabhängige Studie und der Vergleich mit den Simulationen zeigen, dass Drehung und Biegung auch intrinsisch in DNS gekoppelt sind. Neben der Kontrolle der Salzkonzentration in Lösung, entwickelte ich eine Objektivheizung, um die Temperatur während einer Messung präzise zu regulieren. Ich studierte die Veränderung der Windung der DNS und stellte fest, dass die Entwindung mit Temperatur unabhängig von der Zugkraft ist. Vergleicht man experimentelle Ergebnisse mit theoretischen Vorhersagen in Form von Molekulardynamik Simulationen, so haben wir herausgefunden, dass der Effekt durch eine reine Konformationsänderung im DNS-Rückgrat und nicht durch das Schmelzen von Basenpaaren verursacht wird. Diese Konformationsänderung deutet darauf hin, dass sich die Torsionssteifigkeit auch bei erhöhter Temperatur ändert. Ich präsentiere erste Drehmomentmessungen bei erhöhter Temperatur und vergleiche diese mit Ergebnissen von Molekulardynamischen Simulationen.

Zusammenfassend präsentiere ich eine neuartige Methode, um das molekulare Drehmoment der DNS in einer parallelen Weise zu studieren und komme zu dem Ergebnis, dass die Zunahme der Salzkonzentration und Temperatur im biologisch relevanten Bereich, die DNS weicher macht, nicht nur im Hinblick auf die Biegung, sondern auch in der Verdrehung.

Abstract

Nature has developed an inimitably strategy to store and transfer genetic information in the sequence of the double helix of DNA, for its structure the Noble Price has been awarded in 1962. The bases, which carry the genetic information, are located in the interior of the DNA and protected by the double-stranded backbone. During DNA replication or transcription, a well-regulated molecular torque unwinds the double helix to access genes that are located within the helix. DNA topology in the cell is strictly regulated by a group of enzymes called topoisomerases. An inhibition of topoisomerase rapidly causes cell death and can be used to destroy cancer cells. An in depth understanding of the topological and torsional properties of the DNA double helix is therefore essential to life.

Single-molecule techniques have been developed over the last decade to implement precise and well controlled forces and torques on the pN level to stretch and twist molecules to extract their structural information. Methods have been further extended to directly address molecular torque in nucleic acids, such as DNA by implementing magnetic tweezers, the most prominent technique to date. So far molecular torque measurements have been limited to a "one-molecule-at-a-time" method, lacking high statistics.

In this thesis, I present a multiplexed, temperature-controlled and straightforward version of magnetic torque tweezers to probe torsional properties of DNA, such as its helical twist and its torsional stiffness. I demonstrate that both freely orbiting magnetic tweezers (FOMT) and magnetic torque tweezers (MTT) can operate in a multiplexed fashion for properly chosen measurement parameters. It is noteworthy that force calibrations in FOMT and MTT are similar, thus force calibrations can be performed directly in MTT. I developed a multiplexed version of MTT resulting in high-resolution extension-rotation and torque-rotation measurements of double-stranded DNA, giving the opportunity to extract information of structural properties. The torsional response of DNA to changes in the environment, such as salt concentration or temperature, is an important parameter in the understanding of the mechanical behavior of DNA. Implementing the previously established methods I aimed at systematically studying its (DNA's) dependence on various parameters. For this I tested different salt concentrations and found that the intrinsic torsional stiffness does not depend on salt (i.e. at stretching forces that suppress bending). The effective torsional stiffness, however, governs the respond to induced torque at smaller stretching forces, where some of the twist is topologically transformed into bending. I found that the effective torsional stiffness decreases with increasing ionic strength, which is understood by a pure decrease in bending stiffness. At the same time we could use the high-resolution data (at physiological relevant salt) to compare with coarse-grained simulations of DNA and find best agreement, when using the asymmetric, anisotropic twistable worm-like chain. The salt dependent study and the comparison with simulations underlay that bending and twisting are also intrinsically coupled in DNA. Besides controlling the salt concentration in solution, I developed a magnetic tweezers instrument with an add-on objective heating to precisely control temperature to study the change in helical twist of DNA and find that the unwinding effect is independent on stretching force. Comparing experimental results with theoretical predictions in form of all-atom molecular dynamics simulations, we unveiled that the effect is caused purely by a conformational change in the DNA backbone and not a consequence of melting of base pairs. This conformational change suggests that the torsional stiffness also changes upon increased temperature. I present preliminary torque-rotation data at increased temperature and compare those with results of coarse-grained and all-atom molecular dynamic simulations.

Taken together, I present a novel experimental concept to address molecular torque of DNA in a parallelized and straightforward fashion. Using this method I find that the increase of salt concentration and temperature, within biological relevant regimes, softens the DNA molecule not only in terms of bending but also in terms of twisting.

Chapter 1
focuses on magnetic tweezers and mechanical properties of nucleic acids. This chapter serves as an introduction to magnetic tweezers instruments and explains the differences between conventional magnetic tweezers, freely orbiting magnetic tweezers and magnetic torque tweezers. In addition, an overview on mechanical properties of nucleic acids and differences between DNA and RNA is given. This chapter is adapted from **Kriegel** *et al.* [1] published in the *Journal of Structural Biology* in 2017.

Chapter 2
provides details on the magnetic tweezers methodology. The experimental setup, the flow cell preparation, the DNA construct, the magnetic beads, and the bead selection is explained herein. Where necessary, more information on materials and methods is given in each chapter separately. This part focuses on the setup alignment in multiplexed freely orbiting magnetic tweezers and compares force calibrations from freely orbiting tweezers with magnetic torque tweezers using two types of magnetic beads, frequently used in the lab.

Chapter 3
presents a multiplexed version of magnetic torque tweezers that are used for high-resolution extension-rotation and torque-rotation measurements of double-stranded DNA. We use the novel capabilities to probe the salt dependence of torsional properties of DNA, like the buckling point, the post-buckling slope, the buckling torque, and the torsional stiffness of DNA are discussed within this chapter. This chapter is adapted from **Kriegel** *et al.* [2] published in *Nucleic Acids Research* in 2017.

Chapter 4
uses high-resolution extension- and torque-rotation data at physiological salt concentration to compare experimental data of DNA under force and torque with the symmetric, isotropic and the asymmetric, anisotropic twistable worm-like chain using a coarse-grained description of DNA and finds that bending in DNA is anisotropic and that bending and twisting are coupled in DNA. Parts of this chapter are published in *Physical Review Letters* in 2017 by Nomidis, **Kriegel**, Vanderlinden, Lipfert and Carlon [3].

Chapter 5
presents the dependence of the helical twist of DNA on temperature. The change of the helical twist of DNA is studied for several forces (< 1 pN) by combining objective heating with conventional magnetic tweezers, and is compared with all-atom molecular dynamic and coarse-grained simulations using the framework of oxDNA. This chapter is submitted as an article to *Nucleic Acids Research* by **Kriegel** *et al.* and currently under review.

Chapter 6
uses a combination of multiplexed torque tweezers and the heated objective to study the torsional behavior of DNA at increased temperatures. Preliminary extension- and torque-rotation data of DNA at physiological relevant salt conditions, suggest that the torsional stiffness of DNA decreases with increasing temperatures but not as strong as suggested previously, which is compared with and in agreement with predictions of all-atom and coarse-grained simulations.

List of Publications

Publications that are part of this thesis:

1. **Franziska Kriegel**, Niklas Ermann, and Jan Lipfert, **"Probing the mechanical properties, conformational changes and interactions of nucleic acids with magnetic tweezers"**, *J. Struc. Biol.* 197(1), 26-36 (2017)

2. **Franziska Kriegel**, Niklas Ermann, Ruaridh Forbes, David Dulin, Nynke H. Dekker, and Jan Lipfert, **"Probing the salt dependence of the torsional stiffness of DNA by multiplexed magnetic torque tweezers"**, *Nucleic Acids Res.* 45(10): 5920–5929 (2017)

3. Stefanos K. Nomidis, **Franziska Kriegel**, Willem Vanderlinden, Jan Lipfert, and Enrico Carlon, **"Twist-Bend Coupling and the Torsional Response of Double-Stranded DNA"**, *Phys. Rev. Lett.* 118, 217801 (2017)

4. **Franziska Kriegel**, Christian Matek, Tomáš Geršata, Klara Kulenkampff, Sophie Tschirpke, Martin Zacharias, Filip Lankaš, and Jan Lipfert, **"The Temperature Dependence of the Helical Twist of DNA"**, *under review at Nucleic Acids Res.*

Publications that are not part of this thesis:

5. Sabrina Simoncelli*, Samuel Johnson*, **Franziska Kriegel**, Jan Lipfert, and Jochen Feldmann **"Stretching a single dsDNA molecule with an optically trapped gold-silica Janus particle"**, *ACS Photonics* 4 (11), 2843–2851 (2017)
*contributed equally to this work

Contents

Part I

Introduction

Chapter 1

Probing the Mechanical Properties, Conformational Changes, and Interactions of Nucleic Acids with Magnetic Tweezers *

Abstract

Nucleic acids are central to the storage and transmission of genetic information. Mechanical properties, along with their sequence, both enable and fundamentally constrain the biological functions of DNA and RNA. For small deformation from the equilibrium conformations, nucleic acids are well described by an isotropic elastic rod model. However, external forces and torsional strains can induce conformational changes, giving rise to a complex force-torque phase diagram. This chapter focuses on magnetic tweezers as a powerful tool to precisely determine both the elastic parameters and conformational transitions of nucleic acids under external forces and torques at the single-molecule level. We review several variations of magnetic tweezers, in particular conventional magnetic tweezers, freely orbiting magnetic tweezers and magnetic torque tweezers, and discuss their characteristic capabilities. We then describe the elastic rod model for DNA and RNA and discuss conformational changes induced by mechanical stress. The focus lies on the responses to torque and twist, which are crucial in the mechanics and interactions of nucleic acids and can directly be measured using magnetic tweezers. We conclude by highlighting several recent studies of nucleic acid-protein and nucleic acid-small-molecule interactions as further applications of magnetic tweezers and give an outlook of some exciting developments to come.

1.1 Introduction

DNA is the carrier of genetic information in all cellular life. While much emphasis has been placed on deciphering the sequence of DNA bases, it is becoming increasingly clear that the

*This chapter was adapted from Kriegel *et al.* [1] with the permission from Elsevier Inc.

physical properties of DNA as a polymer and polyelectrolyte play critical roles in the regulation of genetic information. In eukaryotic cells, ∼2 m of DNA are packed into a ∼10 μm sized nucleus, which is achieved through numerous interactions with proteins, in particular through the hierarchical assembly of nucleosomes and higher order chromatin structures. At the same time, DNA needs to remain accessible for replication and transcription of the stored information. In addition, during linear processing of DNA, e.g. in replication, transcription, and repair, its double helical nature [4] naturally leads to rotational motion and the accumulation of torque. Accumulation of torque and the ensuing supercoiling of DNA are important factors in gene regulation; DNA stability, and packing, are tightly regulated in vivo [5–11].

With DNA being the primary carrier of genetic information, it has long been known that RNA plays critical intermediate roles in the central dogma, facilitating the transformation of genetic information into proteins as messenger-, transfer-, and ribosomal RNA. In addition to these traditional roles, it has become increasingly clear that RNA assumes many more functions in the regulation of gene expression through mechanisms such as (self-) splicing [12], riboswitches [13], RNA interference [14] , and the CRISPR/Cas pathway [15, 16]. In these contexts, too, the physical properties of RNAs play critical roles in their folding into functional structures, their dynamics and interactions [17–20]. Importantly, like in the case of DNA, the functional units in vivo often consist of both nucleic acids and proteins in tightly interacting nucleo-protein complexes.

Finally, in addition to their evolved biological roles, nucleic acids are increasingly emerging as construction materials in self-assembling nanostructures, notably as DNA and RNA "origami" structures of increasing sophistication and functionality [21–26]. Magnetic tweezers are emerging as powerful tools to investigate the mechanical properties, conformational transitions, interactions and processing of nucleic acids at the single-molecule level [27–32]. In particular, the advent of novel kinds of magnetic tweezers that allow us to directly observe torque and twist [33–40] at the level of individual molecules provides new insights and new perspectives of the fundamental properties of nucleic acids and their interactions with proteins.

In this chapter, we will first summarize and highlight recent developments in magnetic tweezers. We then go on to discuss applications, first to the properties of "bare" nucleic acids, where we emphasize the many similarities but also striking differences between DNA and RNA. Finally, we highlight recent applications to the study of small molecule binding to DNA and nucleic acid-protein interactions.

1.2 Magnetic tweezers instruments

1.2.1 The principle of a magnetic tweezers setup

In magnetic tweezers (MT), the molecules of interest are tethered between a flow cell surface and magnetic beads. Typically, an inverted microscope and monochromatic illumination are used to track the diffraction pattern of the beads using video microscopy to determine their X, Y, and Z-positions. Permanent (and in some cases electro-) magnets placed above the flow cell apply magnetic fields and thus magnetic forces and torques on the beads, which, in turn, allow stretching and twisting the molecules of interest.

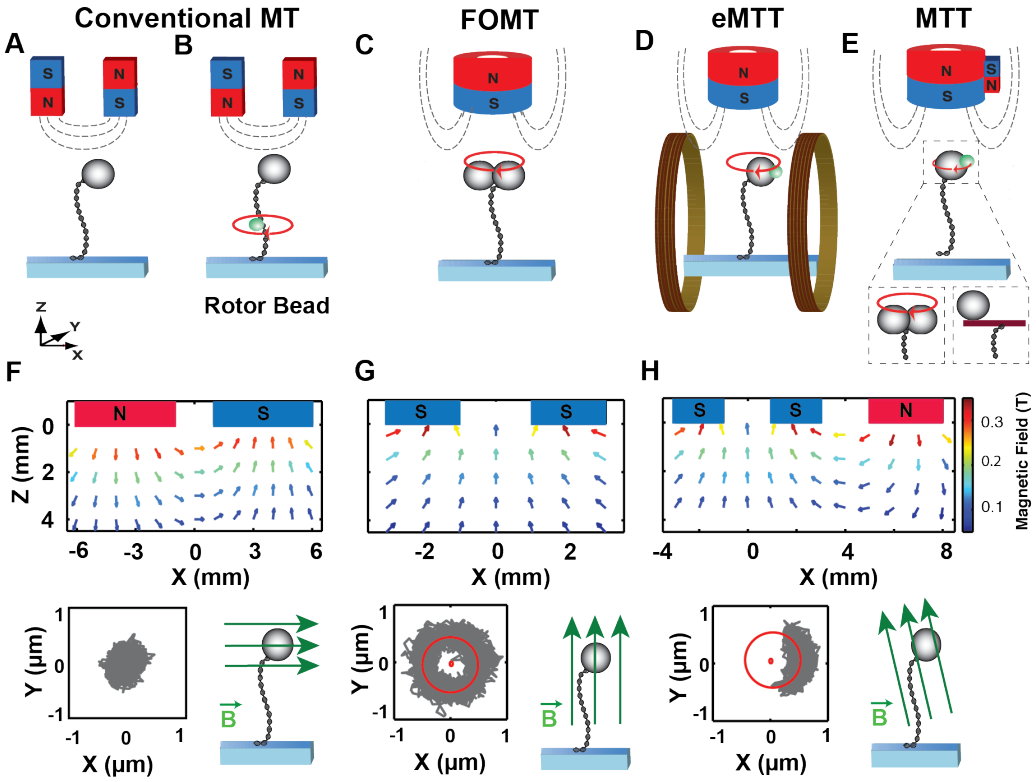

Figure 1.1: Variations of magnetic tweezers (A-E). Conventional MT consist of two cubic, permanent magnets (A,B) that produce a horizontal magnetic field (F) at the location of the magnetic bead, while cylindrical magnets (C-E) create a vertical magnetic field (G). Helmholtz coils around the cylindrical magnets (D), as in electromagnetic torque tweezers (eMTT), or an additional side magnet (E), in magnetic torque tweezers (MTT), slightly tilt the vertical magnetic field (H). The X,Y-fluctuations of the magnetic bead depend strongly on the direction of the magnetic field. The rotation of the bead about the tether axis in (F) is strongly confined and deviates barely from its equilibrium position. This stands in contrast with (G), where the rotation of the bead about the tether axis is completely unconstrained and the bead's fluctuations trace out a doughnut-like shape in the X,Y-plane. In (e)MTT, with a slightly tilted magnetic field (H), the rotation of the bead is weakly confined such that the bead does not trace out a whole circle, but an arc. The field gradients in all MT configurations shown generate (upward) pulling forces on the magnetic beads, thus stretching the molecules of interest.

1.2.2 Conventional magnetic tweezers

Conventional MT, pioneered by Croquette and coworkers [41], typically use pairs of cubic permanent magnets that produce a horizontal magnetic field at the location of the magnetic beads (Figure 1.11A,F). This MT configuration can apply precisely calibrated forces [28, 42–44] by controlling the distance between the magnets and the tethered beads, enabling force-extension measurements over a large range of forces, in particular also in the low force regime (< 0.1 pN). In addition, due to the horizontal magnetic field (Figure 1.1F), the preferred magnetization axis of the bead [45] tightly aligns with the field, strongly confining the rotational motion of the bead. Consequently, the rotation angle of the bead barely deviates from its equilibrium position, allowing the application of and precisely control twist to nucleic acid tethers. However, it is difficult to reliably detect angular changes and to measure torque in this conformation, which is the main difference to Freely Orbiting MT (FOMT) and Magnetic Torque Tweezers (MTT), see Table 1.2.

1.2.3 Freely orbiting magnetic tweezers and the rotor bead assay

In contrast to conventional MT, freely orbiting MT (FOMT) employ cylindrical magnets (Figure 1.1C) that produce a vertical field, along the tether axis. Consequently, the bead's preferred magnetization axis aligns vertically and the rotation of the bead about the tether axis is unconstrained, while there is still a controlled upward force applied to the bead that stretches the molecule. When the vertical magnet is well aligned, the bead's fluctuations in the X,Y-plane trace out a doughnut shape (Figure 1.1G) and the free rotation of the bead is only constrained by the nucleic acid tether. The doughnut-shaped fluctuation pattern of the bead's motion allows the tracking of angular changes by converting the X,Y-position to radial and angular coordinates [36]. A conceptually similar measurement strategy is the rotor bead assay (Figure 1.1B) that employs conventional magnetic tweezers to apply stretching forces and an additional fluorescent marker bead or gold nanorod in the middle of the DNA tether for angular tracking [40, 46–48]. Separating force actuation from angular tracking makes the rotor bead assay somewhat more complicated in terms of the molecular assembly than the FOMT (necessitating e.g. three attachment points for beads or other actuators, instead of two in the FOMT), yet has the advantage of providing greater flexibility in terms of the angular tracking approach and in particular enabling the use of very small particles for angular tracking, which increases the temporal resolution [40].

1.2.4 Magnetic torque tweezers

Magnetic torque tweezers (MTT) control the rotation of the magnetic beads and thus the twist of the tethered molecule, similar to conventional MT; however, they expand the capabilities of MT by enabling direct measurements of single molecule torques [33–35, 37]. The employed magnet configuration is typically similar to FOMT, with a central vertically aligned magnet. Unlike in FOMT, additional horizontal magnetic fields, either from misalignment of the central magnet [33, 35], Helmholtz coils around the cylindrical magnet [38], or through the use of a permanent side magnet [34] (Figure 1.1D,E), give rise to a weak angular trap that enables torque measurements (Figure 1.1H). The horizontal field component constrains the rotation of the bead, giving rise to an arc-shape pattern in the X,Y-plane (Figure 1.1H), and allows inducing twists in the molecule and measuring the restoring torque [33–35, 37, 38].

1.2.5 Angular tracking and the principle of torque measurements in magnetic torque tweezers

Torque measurements in MTT rely on angular tracking to detect the rotation angle of the bead about the tether axis. Figure 1.2A shows a schematic of how angular tracking in MTT enables torque measurements. At zero turns the bead is at its rotational equilibrium position θ_0 and the nucleic acid tether is torsionally relaxed. After applying N turns the molecule is twisted and the bead's angular position is shifted (slightly) from θ_0 to θ_N. This change in the mean rotation angle is detectable in MTT (Figure 1.2A, histograms) and provides information about the restoring torque exerted by the nucleic acid when twisting it: the molecular torque τ_{mol} is simply given by the change in the mean rotation angle after N turns multiplied by the angular trap stiffness (k_θ, i.e. k_{ROT}), which is in turn calibrated from the width of the thermal

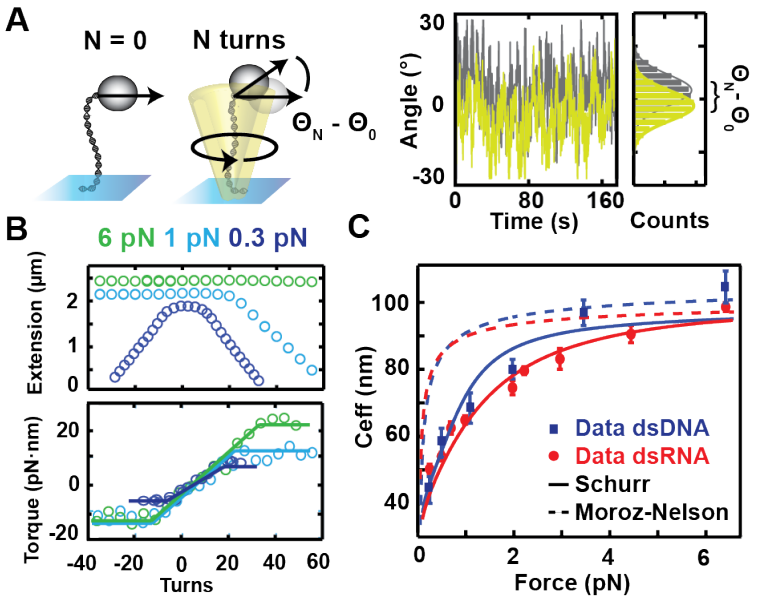

Figure 1.2: Angular tracking in MT and the torque response of dsDNA. (A) When turning the magnet and thus the beads, twist is induced in the molecule that can be measured in MTT, based on detecting changes in the rotational angle. (B) Typical extension-rotation curves for dsDNA (top) showing the extension of the DNA molecule against turns at three different forces (6 pN, 1 pN, and 0.3 pN). Also shown are the corresponding torque responses of dsDNA for the three forces (bottom). (C) The torsional stiffness (C_{eff}) of dsDNA (blue; data from [34]) and dsRNA (red; data from [49]) is force-dependent. Two models are shown: the Moroz-Nelson theory (first-order) fit to the high force data (F > 3 pN; dashed line) and the Schurr model (solid line), see main text for a description of the models.

fluctuations (where k_BT is the thermal energy) of the bead's motion:

$$\tau_{mol} = -k_\theta < \theta_N - \theta_0 > \tag{1.1}$$

and

$$k_\theta = \frac{k_BT}{Var(\theta)} \tag{1.2}$$

Several techniques have been used for angular tracking. One approach is to use cylindrical magnets plus a nanorod or two coupled magnetic beads (Figure 1.1E, inset) to which the magnetic particle is attached in order to twist the molecule [33, 37]. Additional options are to add a small fiducial marker bead to the magnetic bead (Figure 1.1E and F) [34] or to track intrinsic inhomogeneities of the beads [35, 50]. Finally, the experimentally most straightforward approach to angular tracking is to convert the X,Y-position to an angle for beads that move on a circular arc (Figure 1.1H, bottom).

1.3 Applications of magnetic tweezers

1.3.1 The "standard model" of double-stranded DNA and RNA: Nucleic acids as isotropic elastic rods

Both double-stranded DNA (dsDNA) and double-stranded RNA (dsRNA) form right-handed helices under physiological conditions, of overall similar dimensions. dsDNA naturally adopts a B-form helix, with a radius of ~1 nm, a rise per base pair of 3.4 Å[51] and a helical pitch of 10.5 base pairs per turn [52], while dsRNA takes on an A-form helix, which is somewhat shorter (2.8 Å/bp and 13 bp/turn [53]) and thicker (~1.2 nm radius). On scales significantly larger than one base pair, double-stranded nucleic acids can be well approximated as isotropic elastic rods, at least under not too large forces and torques. An isotropic elastic rod can undergo bending, stretching and twisting deformations and its elastic response is characterized by the elastic parameters bending persistence length (A), stretch (or Young's) modulus (S), torsional persistence length (C) and twist-stretch coupling (D)[54].

In recent years, all four elastic parameters were quantitatively determined for both dsDNA and dsRNA in a series of landmark single-molecule measurements, not least using a number of ingenious MT-based assays. In the next sections, we will briefly describe how the various elastic parameters have been determined. In particular, we will focus on the similarities (as might be naively expected from their similar overall structure) yet also important differences between dsDNA and dsRNA.

Bending persistence length A

For forces $\leq$ 10 pN, the measured force-extension response of nucleic acids is in excellent agreement with the (inextensible) worm-like chain (WLC) model of purely entropic stretching elasticity [49, 55–57]. The bending persistence length A for both dsDNA and dsRNA has been determined from fits of the WLC model to low-force force-extension data to be ~45 nm for dsDNA [49, 58–61] and ~57 nm for dsRNA [49, 61], in ~150 mM monovalent salt. A increases strongly for low salt (< 150 mM monovalent salt) whereas it decreases only slightly with increasing ionic strength (> 150 mM monovalent salt) of the solution [58, 60], in approximate agreement with models that split A into an intrinsic and an electrostatic component, first introduced independently by Odijk and Skolnick-Fixman (OSF) [62, 63]. However, open questions, which are beyond the focus of this review, remain: First, the detailed dependence of the persistence length on salt concentration for multi-valent ions that are not well described in the linearized Debye-Hückel theory employed by OSF [64, 65]. Second, the treatment of flexible polymers, in particular single-stranded nucleic acids [66–69], as the OSF model is strictly valid only in the stiff rod limit. Third, to what extend the other elastic parameters (in particular C and D discussed below) depend on salt. Note, that the dependence of the torsional stiffness on salt concentration is discussed in detail in Chapter 3.

Stretch modulus S

At forces $\geq$ 10 pN, enthalpic contributions to the stretching response need to be taken into account and force-extension data for both dsDNA and dsRNA are well-described by the extensible WLC model that incorporates the stretch modulus S [59, 70] up to forces $\leq$ 50 pN, where

they undergo an overstretching transition, see below. Experiments showed that the stretching modulus of dsRNA (~350 pN) is approximately three times lower compared to that of dsDNA (~1000 pN) [49, 58, 60, 61, 71]. This difference between dsDNA and dsRNA can be understood from the "springiness" of the dsRNA helix, where the bases have an inclination and for which the center line (the line connecting the centers of the base pairs) forms itself a helix, unlike for dsDNA, where the center line is almost straight [72].

Torsional persistence length C

Probing the torsional degrees of freedom (e.g. the elastic parameters C and D) requires single molecule methods capable of applying both forces and torques. MTT are ideally suited for this task, as they allow inducing and directly measuring torque. A typical torque measurement is shown in Figure 1.2B, where both the tether extension (top) and torque (bottom) are monitored as a function of the applied turns for dsDNA, at three forces, 6 pN, 1 pN and 0.3 pN. When twisting nucleic acids close to zero turns (which corresponds to the torisonally relaxed helix) there is little change in the measured extension while the torque increases linearly with applied turns. From the slope of the torque vs. turns response in the linear regime (Figure 1.2B, solid line) the effective torsional stiffness (C_{eff}) of the molecule can be determined using $C_{eff} = L_c/(2\pi N k_B T)\tau_{mol}$, where L_c is the contour length of the nucleic acid and N the applied number of turns. The effective torsional stiffness C_{eff} increases with force for both dsDNA (blue) and dsRNA (red) (Figure 1.2C). This force dependence needs to be taken into account when comparing measurements of C_{eff} that employ measurement modalities at different forces, such as MTT, FOMT, the rotor bead assay, and fluorescence polarization anisotropy [34, 36, 46, 73–76]. Moroz and Nelson (MN) have introduced an model that rationalizes why the effective twist rigidity (C_{eff}) is smaller than the microscopic rigidity (C), based on the coupling of twist and bend fluctuations, and their model allows estimating C from rotation-extension curves [77, 78]. The MN model (Figure 1.2C, dashed line) provides a reasonable description of C_{eff} as a function of force, in particular if higher order terms are included in the model [36] and if the torsional persistence length is treated as a free fitting parameter [35, 48, 76]. However, direct measurements of C_{eff} are not fully consistent with the MN predictions and reveal small, but systematic and statistically significant deviations between data and model. Fitting the MN model to the high force data, the measured values for C_{eff} at low forces (< 1-2 pN) systematically fall below the prediction of the MN model [34, 36, 79]. To account for these deviations, Schurr has recently proposed an extension of the MN model that incorporates two different (sub-) states of the dsDNA helix and provides a closer agreement with the experimentally observed data (Figure 1.2C, solid line) [80]. The Schurr model assumes that there are two states of the helix, which can interconvert in a cooperative fashion and differ slightly in their local rise per base pair and in their torsional rigidity. Such a two-state model was previously invoked to explain anomalous fluctuations of dsDNA in X-ray scattering measurements [81]. Increasing the force shifts the equilibrium of the two states to the longer and torsionally stiffer sub-state. The model features a total of five fitting parameters: The equilibrium free energy difference between the two-states, a parameter associated with the cooperativity of the transition, the difference in rise per base pair between the two states, and the torsional stiffnesses of the two sub-states. The first three parameters are obtained from a fit to small deviations from the WLC model in force-extension data and provide the relative populations of the two states as a

function of force. Finally, the torsional stiffnesses of the sub-states are fitted to the C_{eff} vs. force data. Schurr obtained values of 100 nm for the rigidity in the sub-state that is valid for high forces and 40 nm for the sub-state for low forces (for dsDNA). Those fit parameters provide a significantly better fit to the dsDNA data ($\chi^2 \sim 2$) than the original MN model ($\chi^2 \sim 13$, for a fit of the MN model over the entire force range). While the Schurr model is speculative at this time, we note that employing a similar fitting procedure, we also find a significantly improved fit to the C_{eff} vs. force data for dsRNA (Figure 1.2C, red solid line,$\chi^2 \sim 6$ vs. $\chi^2 \sim 67$ where both models are fit over the entire force range), which suggests that a similar two state transition might occur in the RNA helix. Nonetheless, the introduction of two sub-states is currently somewhat ad hoc and further evidence (e.g. from spectroscopy) is required to test and evaluate the model. Note, that the MN model is also co-plotted to C_{eff} vs. force data in Chapter 3 and 6. A discussion on MN and other models such as the twistable worm-like chain and the twist-bendible worm-like chain is given in Chapter 4.

The twist-stretch coupling D

The only coupling term between elastic deformations in the isotropic elastic rod model is the twist-stretch coupling constant D. Unlike the other elastic constants (A, S, and C), D can be both positive and negative: Positive values of D correspond to a situation where the rod shortens upon overwinding (or, equivalently, unwinds upon stretching); negative D means that the rod lengthens upon overwinding (or overwinds upon stretching). Macroscopic intuition (e.g. with wringing out a towel) suggests that overwinding should result in shortening, a behavior initially also suggested for DNA [82, 83]. However, later high-resolution single molecule measurements revealed that, surprisingly, overwinding DNA close to its equilibrium conformation results in lengthening of the molecule [84, 85]. Similar measurements on RNA revealed yet another surprise: RNA shortens when overwound [49], i.e. the twist-stretch coupling for DNA and RNA has opposite signs (Figure 1.3A), a finding that challenged existing models of nucleic acid mechanics. Several generations of models have been proposed to explain the observed twist-stretch coupling: Initial models treating DNA (or RNA) as an elastic medium with a helicity predict both molecules to shorten upon overwinding [82, 83], in disagreement with high-resolution DNA measurements. Models featuring a stiff helical backbone around a softer elastic core correctly predict the behavior for DNA, but fail for RNA [84, 86]. Similarly, a modeling approach that represents DNA and RNA at the base pair level and uses available crystal structures to determine their elastic parameters ("HelixMC") correctly predicts the twist-stretch coupling for DNA, but fails for RNA [49, 72]. Conversely, a simulation framework that coarse grains DNA and RNA at the single base level ("oxRNA/oxDNA") correctly predicts the twist-stretch for RNA, but fails for DNA [87, 88]. A correct prediction of the puzzling difference between DNA and RNA has finally been achieved using all-atom, explicit solvent molecular dynamics simulations [89]. The molecular dynamics have revealed that an increase in the inclination of bases upon overtwisting leads to a reduction in the helix radius and thus an overall extension of DNA (Figure 1.3A, blue). In contrast, for RNA the bases already exhibit significant inclination in the torsionally relaxed state; overwinding thus leaves the helix' radius approximately constant and leads to shortening of the molecule (Figure 1.3A, red) [89]. In summary, while being a relatively small effect, the twist-stretch coupling provides a compelling example how precision single-molecule measurements can provide stringent tests of current

models of nucleic acid structure and dynamics.

The "standard model" described here, is also called the symmetric, isotropic rod model and uses the above mentioned parameters to characterize nucleic acids. Chapter 4 leads then over to the asymmetric, anisotropic worm-like chain, which takes anisotropic bending along the nucleic's backbone and a coupling between bending and twisting into account.

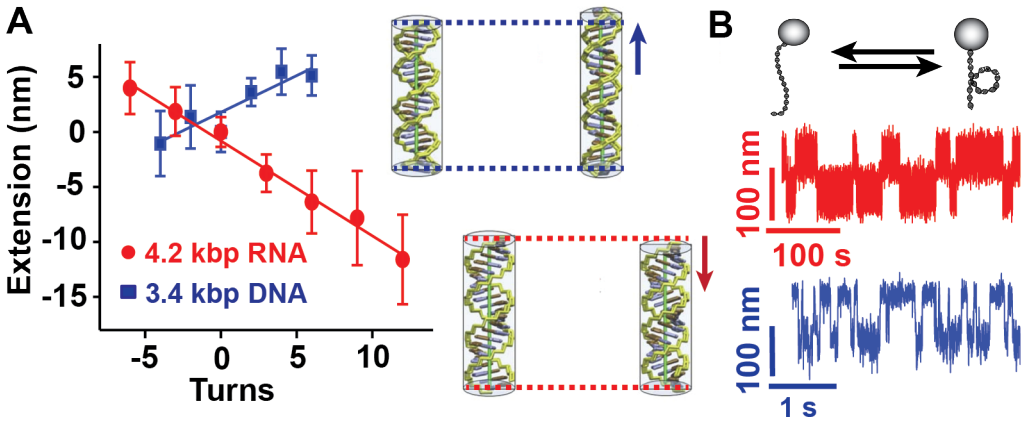

Figure 1.3: Surprising differences between dsDNA (red) and dsRNA (blue). (A) Relative change in extension vs. number of applied turns for both dsDNA and dsRNA at high force (F = 7 pN). The data reveal opposite signs for the twist-stretch coupling D [49]. The insets show the results of all-atom molecular dynamics simulations [89]: DNA lengthens when overwound whereas RNA shortens, in agreement with the experimental data. (B) Extension vs. time traces for dsDNA and dsRNA at the buckling transition. The traces reveal thermally activated transitions between a twisted, but straight and a plectonemic state. The time scale for this transition is in the millisecond range for dsDNA and on the order of seconds for dsRNA under otherwise identical conditions (F = 4 pN and 320 mM NaCl).

1.3.2 Conformational transitions induced by forces and torques

In physiological conditions and in the absence of large external forces and torques, dsDNA and dsRNA adopt B-form and A-form helix structures, respectively, with elastic properties described in detail in the above sections. However, under external forces and torques both nucleic acids can undergo conformational changes and take on various structural forms. Using single-molecule measurements, MT in particular, the force and torque responses of both dsDNA and dsRNA have been mapped out carefully, resulting in an (almost) complete description of the structural transitions in a force-torque phase diagram, see Figure 1.4A for dsDNA and Figure 1.4B for dsRNA.

Buckling transitions, the formation of plectonemes, and torque induced melting

When over- and underwound at relatively low forces, both dsDNA and dsRNA eventually release torsional stress by undergoing buckling transitions, resulting in the formation of plectonemic supercoils (Figure 1.2B). At low forces (< 1 pN), the response to positive (overwinding the helix) and negative twist (underwinding the helix) is symmetric and both dsDNA and dsRNA release torsional stress by forming positive and negative plectonemic supercoils upon over- and underwinding, respectively (see e.g. Figure 1.2B, lower curves). At higher forces (> 1 pN), the

response upon over- and underwinding becomes asymmetric: While the molecules still buckle and form plectonemes upon overwinding, underwinding leads to torque-induced melting. The critical torques for torque-induced melting have been determined to be -10 ± 1 pN·nm for dsDNA [34, 46, 90] and -11 ± 1 pN·nm for dsRNA [49], consistent with their similar base pairing energies. The critical torques and the critical supercoiling densities for buckling are very similar for both dsDNA and dsRNA [49] and reasonably well described by the simple isotropic elastic rod picture [34, 49, 91, 92] and captured by coarse-grained simulations [79, 93]. Nonetheless, open questions remain. It is generally observed that there is a linear relationship between effective tether extension and the number of applied turns past the buckling transition, where every additional turn leads to the formation of an additional coil of the plectonemes [79, 91, 93–95]. In this plectonemic regime, the torque is typically assumed to be constant and equal to the buckling torque [37, 91, 92], as indicated by the currently available experimental data [33, 34, 38] (Figure 1.2B). However, there are theoretical predictions that in the multiplectoneme regime, which will be populated particularly at low force under low salt concentrations [96], the torque will vary even in the plectonemic regime [79, 93, 95, 97]. Another open question concerns the transition dynamics: A large difference was observed in the dynamics of the buckling transition from torsionally strained, but uncoiled B-DNA/A-RNA to plectonemic nucleic acids (scB-DNA/scA-RNA). The transition at the buckling point is at least two orders of magnitude faster for dsDNA than for dsRNA, see Figure 1.3B [49].

Formation of P-DNA and P-RNA upon overwinding

If dsDNA or dsRNA molecules are overwound at stretching forces ≥ 5 pN, which are sufficient to suppress buckling until positive torque values of ≥ 35 pN·nm are reached [34, 46, 49, 98] a structural transition from B-DNA to P-DNA (A-RNA to P-RNA) occurs (see schematic in Figure 1.4). Both DNA and RNA P-form helices are proposed to adopt conformations with the bases facing outward and the highly overwound sugar phosphate backbone in the center (Figure 1.4A, insets) [99, 100]. This is similar to the conformations that Linus Pauling (incorrectly) proposed for the equilibrium structure of dsDNA in 1953 [101], hence the term "P"-DNA, and, by analogy, P-RNA. For P-DNA it is known that it has a much smaller helical twist than the B-form, experimental values range between 2.6 [99] and 2.7 [46] base pairs per turn. The contour length was found to be 1.5 [46] and 1.6 times longer [99] than B-DNA. A measured bending persistence length of 19 nm [99] and torsional persistence length of P-DNA of 20 ± 10 nm [102] suggest P-DNA to be significantly more flexible than B-DNA. At forces < 20 pN measurements showed that there is almost no change in the extension of the nucleic acids upon overwinding into the P-form regime, which is interpreted as a transition from B-/A- to a supercoiled P-form. Above 20 pN, an increase of the molecule in length as it is overwound was observed, suggesting an extended P-form. The higher the applied force the less torque is needed to drive the transition from B to P [46, 102] (Figure 1.4A).

Formation of L-DNA and L-RNA upon underwinding

Upon underwinding of dsDNA and dsRNA the formation of negative supercoiled plectonemes is favored up to a critical torque of -10 ± 1 pN·nm and -11 ± 1 pN·nm for dsDNA and dsRNA, respectively. At forces ≤ 1 pN (with the exact force depending on salt concentrations, temperature and pH) [103–105] underwinding reaches torque values sufficient to induce (partial)

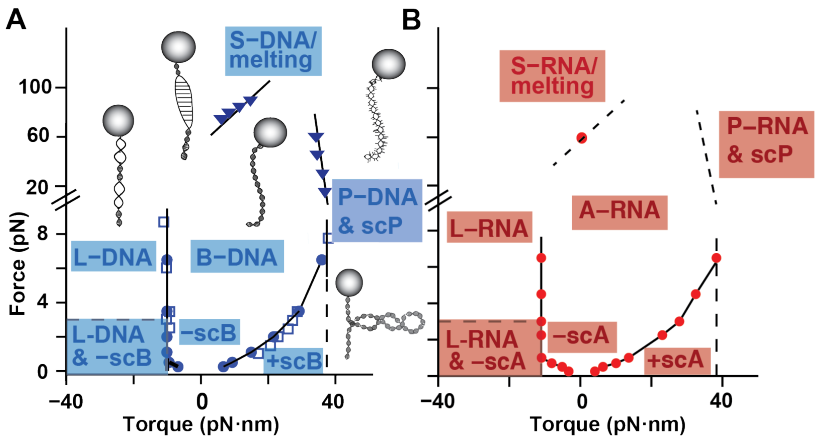

Figure 1.4: Phase diagrams for dsDNA (A) and dsRNA (B). Experimentally measured critical torques and forces are indicated by symbols. Solid lines are phase boundaries that have been mapped out by direct measurements. Dashed lines are phase boundaries that are inferred from the data. The overall phase diagrams under applied forces and torques are similar for dsDNA and dsRNA. Insets in panel (A) show illustrations of the nucleic acid conformations associated with the various phases. For a detailed description of the structures and transitions see the main text. Data points for dsRNA (red dots) are from [49]. For dsDNA, blue dots are from [34], blue squares from [90] and blue triangles from [46].

melting of the double-stranded helices. Upon adding more twist beyond the onset of the melting transition, the torque stays constant at the melting torque value over a large range of turns, up to a supercoiling density of −1.8 for dsDNA [90] and −1.9 for dsRNA [49], when, finally, a transition from the B-/A- to the L-form with an averaged left-handed twist takes place. The helical twist for both L-DNA and L-RNA was determined to be approximately −13 base pairs per turn [49, 90]. Compared to B-form DNA, the contour length was found to be 1.4 times larger, the bending persistence length 3 nm and the torsional stiffness 10 to 20 nm [90].

A more detailed analysis whether the L- form consists of melted base pairs and/or of "Z-DNA" (a left-handed form of DNA that is slightly longer and has reverse twist [90, 106] found that in a DNA sequence featuring multiple GC-repeats underwinding induces a transition to Z-DNA at approximately −3 pN·nm; however, for a random DNA sequence no sharp transition was observed [48, 107, 108]. Taken together, these data suggest that underwound DNA under sufficiently high forces and torques features a co-existence of B-, Z-form and melted DNA.

Formation of S-DNA and S-RNA upon overstretching

When pulling on torsionally unconstrained dsDNA or dsRNA with forces higher than 50 pN, B-DNA and A-RNA undergo a rapid overstretching transition, suddenly lengthening by a factor of ~1.7 and ~1.9, respectively [49, 61, 71, 109, 110]. The exact force at which the transition takes place is lower for dsRNA than for dsDNA [49, 61] and depends on ionic strength [58, 60, 71], temperature [111], GC content of the nucleic acids sequence [112] and pH [113]. Two models have been proposed for the nature of this overstretched form. One model describes the molecule with elongated base pairs, stretched but still double-stranded [71, 110], a form usually referred to as stretched or S-DNA, with (partial) melting occurring at even higher forces [112]. The helical twist of S-DNA was suggested to be 35 base pairs per right-handed turn [46, 114, 115]. The other model interprets the overstretching transition as force-induced melting and breaking

Table 1.1: Mechanical and structural parameters of various conformations of dsDNA and dsRNA. A collection of measured values for the persistence length A, the torsional stiffness C, the helical pitch and the rise per base pair are listed for A-RNA, B-DNA, P-DNA, L-DNA, S-DNA, and Z-DNA. "Relative extension" describes the contour lengths relative to the state of the nucleic acid at low forces and torques.

	A-RNA	B-DNA	P-DNA	L-DNA	S-DNA	Z-DNA
A (nm)	57	45	19	3	15 [121]	200
C (nm) at high force	100	109	20±10	10-20	No value available	No value available
Helical pitch (bp/turn)	13	10.5	2.6, 2.7	-12 to -15	35	-12
Relative extension	1	1	1.5, 1.6	1.4	1.7	1.1
Rise per bp (nm/bp)	0.28	0.34	0.54	0.48	0.58	0.37
Helicity	Right-handed	Right-handed	Right-handed	Left-handed	Right-handed	Left-handed

of the hydrogen bonds when pulling, leading to a splitting of the helix into two single-strands [60, 111, 113, 116]. In contrast, for torsionally constrained dsDNA and dsRNA, no sharp plateau but a gradual extension of the molecule is observed [49, 116, 117]. Recent results for dsDNA suggest that both force-induced strand separation and S-DNA formation can occur, depending on sequence content, temperature, and salt concentration [118–120]. Less is known about the overstretching transition for dsRNA, however, it appears plausible that similar overstretching modes exist.

An overview of experimentally determined values for the elastic properties of dsDNA and dsRNA are listed in Table 1.1; corresponding references are given in the text.

1.3.3 Interactions of nucleic acids with small-molecules and proteins

Going beyond the mechanical properties and conformational transitions of “bare” nucleic acids, MT are a powerful tool to study nucleic acid-protein and drug interactions and to dissect, e.g., the processes underlying replication, transcription, and repair of DNA and RNA, which are central to cellular and viral lifecycles. There are a number of excellent reviews of these applications of MT [11, 31, 32, 39, 122, 123]. Here, we highlight only briefly a few recent studies involving the twist dependence of small-molecule binding and the use of novel MT approaches such as FOMT to probe DNA-protein interactions.

Detecting small-molecule binding to DNA in MT

MT (and MTT [33]) have been used to measure the effect of various small molecules binding to DNA, in particular of the intercalators ethidium bromide (EtBr) and doxorubicin (DOXO), of netropsin (a minor-groove binder), and of topotecan and cisplatin, which are used as chemotherapeutics [124, 125]. Intercalators generally lengthen [110, 126–129] and unwind [124, 125] the DNA helix, as would be expected from their binding mode where an aromatic moiety is inserted between the stacked DNA bases. The length increase per intercalation event is ~3.4 Å, i.e. inserting an aromatic moiety into the DNA helix has an effect on its length similar to adding a base pair. In the process, the helix unwinds. For ethidium bromide, the unwinding angle per intercalated molecules was found to be 27° ± 1° [124], a value likely representative for other monointercalators. In contrast, it is an open question how much bis-intercalators unwind the helix. For example for YOYO-1, a frequently used bis-intercalator, literature values range from 24° to 106° unwinding per dye [130, 131], while the naive estimate from monointercalation would suggest 2 x 27° = 54°. In addition, the fact that intercalation unwinds the helix suggests that binding of intercalators is likely to be torque dependent, which is confirmed by preliminary

experiments [132] but awaits further quantification. In contrast to intercalators, minor groove binders have much smaller effects on either DNA length or twist. Netropsin was found to slightly overwind the helix upon binding [124], but it is unclear whether this is a general effect of minor groove binding.

1.3.4 Investigating nucleic acid protein interactions in FOMT

FOMT are capable of detecting changes in the tether extension, and, at the same time, they allow for angle tracking (see Table 1.2). This combination makes them particularly appealing for the study of processes that affect both the length and overall twist of the nucleic acid, e.g. upon protein binding.

RNA polymerase

A classic study employed a FOMT-like assay to monitor RNA polymerase transcribing DNA[133]. RNA polymerase was attached to the bottom of the flow cell and a magnetic bead to a DNA molecule. With additional fluorescent markers on the magnetic bead, the rotation of the bead and thus DNA while being transcribed by the enzyme was detected. It was observed that RNA polymerase rotates DNA clockwise and that the enzyme exerts torques up to > 5 pN·nm[133], in an NTP-dependent fashion. Recent studies finally indicated that RNA polymerase is able to generate upstream torques with a mean of 11.0 ± 3.7 pN·nm and downstream torques with a maximum at 10.6 ± 4.1 pN·nm, consistent with DNA melting torque [134].

Recombinases RecA and Rad51

More recent work exploited the ability to track tether length and rotation at the same time. Two studies investigated RecA (from bacteria) and the homologous Rad51 (from eukaryotes), which are proteins involved in the repair of DNA by homologous recombination [135]. To enable recombination, RecA or Rad51 proteins bind cooperatively and assemble as a filament on DNA, in the process lengthening and unwinding the double-helix. The assembly of RecA and RAD51 filaments on DNA can be monitored in real-time using FOMT [36, 136]. The studies revealed a lengthening of 0.5 nm and an unwinding angle of $\sim 45^\circ$ per RecA or RAD51 monomer [36, 136], in agreement with biochemical and structural evidence.

Nucleosomes

A similar measurement strategy was used to study the assembly and dynamics of nucleosomes on DNA. Nucleosomes consist of ~150 base pairs of DNA tightly wrapped around a histone core and are the basic packaging unit of DNA in the nucleus [7, 137]. Interactions of nucleosomes and their higher order assemblies in nucleosome fibers and ultimately chromosomes are critical processes for genome storage and regulation. The assembly of single nucleosomes (consisting of dimers of H2A, H2B, H3 and H4) and tetrasomes (involving only H3 and H4) was studied using FOMT, monitoring the change in extension and in linking number at the same time[138]. The data showed that the assembly of a single nucleosome shortens the molecule by 46 nm, which corresponds to ~146 base pairs, and induces a change in the linking number of −1.2 [138]. For tetrasomes the compaction in length was 24 nm and the change in twist −0.73 for the preferred,

Table 1.2: Comparison of the capabilities of different MT configurations. All magnet configurations exert and allow measuring forces, generally ranging from 0.1 pN to 100 pN. Tracking in X,Y and Z is possible in all cases with a resolution down to 1 nm or less. Torque can be applied in conventional MT and also in MTT. In contrast to MTT, conventional MT do not allow measuring torque. In FOMT, the bead's motion is unconstrained around its tether axis and it is free to rotate. This feature can be exploited to observe angular changes.

	Conventional MT	**FOMT**	**MTT**
Force	Apply and measure	Apply and measure	Apply and measure
X,Y,Z-tracking	Yes	Yes	Yes
Torque	Apply only	Free rotation	Apply and measure
Angle tracking	No	Yes	Yes

left-handed state [138]. Surprisingly, it was observed that tetrasomes fluctuate between a preferred left-handed state, and a right-handed conformation, separated by a linking number difference of 1.7 ± 0.1 turns, without changing the overall extension. In addition, direct torque measurements revealed that the application of weak positive torques is sufficient to drive all tetrasomes into the right-handed state (or vice versa).

(Reverse) Gyrase

Two final illustrative examples of studies employing FOMT-type instruments look at DNA (reverse) gyrase. The rotor bead assay was employed to probe the enzymatic activity of gyrase, which can introduce negative supercoils in DNA in an ATP-dependent fashion, e.g. to compact the genome, relieves strain during replication, and to promote local melting [47]. Interestingly, stepwise activity was observed showing that the unwinding takes place in multiples of two. Applying forces ranging from 0.35 pN to 1.3 pN showed that the enzymatic activity is strongly inhibited with increasing forces and revaled a kinetic intermediate [47, 139]. A FOMT-like assay was used to obtain the first single-molecule characterization of reverse gyrase, an enzyme found in hyperthermophiles that can introduce positive supercoils into DNA in an ATP-dependent fashion, an activity suggested to help increase DNA stability under elevated temperatures[140]. The single-molecule study found 5-fold higher activity than previously determined in bulk, but also revealed that relatively small forces (~0.5 pN) or torques (~ 5 pN·nm) abolish activity [140].

1.4 Summary

Yesterday's sensation is today's calibration and tomorrow's background.
Richard Feynman

Single-molecule measurements of DNA beautifully illustrate the famous quote by Richard Feynman [141]. The first stretching experiments on DNA [55, 142] ushered in the field of single-molecule nanomechanics; now the WLC-type stretching response of DNA is frequently used as a calibration of instruments or new techniques and, furthermore, currently the dominant source of background noise in single-molecule protein folding experiments that use DNA linkers [143, 144]. Similarly, the first DNA twisting experiments in MT opened up the possibility to observe torque-induced DNA supercoiling and melting at the level of individual molecules for the first time [41, 145]. Now, the asymmetric twisting response of DNA under forces > 1 pN

is routinely used to verify that magnetic beads are attached by only a single double-stranded DNA tether. In addition, high-resolution twist and torque measurements of DNA now allow us to test and to precisely calibrate models of nucleic acids [72, 89, 97]. At the same time, the intrinsic fluctuations of supercoiled DNA provide the dominant source of noise in experiments that use supercoiled DNA in MT to detect protein binding and activity; similarly, the intrinsic torsional stiffness of DNA limits the angle and time resolution in assays that employ DNA twisting for the same purpose [37, 40]. We anticipate that high-resolution single-molecule measurements will continue to inspire and test increasingly refined models of nucleic acid mechanics and structure. Outstanding questions in particular regarding the behavior under twist and torque are, inter alia, the torque in the (multi-)plectoneme regime, the discrepancy between the observed effective torsional stiffness at low forces and the predictions of the basic isotropic rod model, and the buckling dynamics of DNA and RNA. Such models form the basis of a quantitative understanding of the behavior of nucleic acids in biological contexts and of engineered nanostructures that increasingly employ DNA and RNA as building materials. Going beyond the properties of bare nucleic acids, MT will be an invaluable tool to dissect the mechanical properties and conformational transitions of nucleo-protein complexes and filaments, which are involved in many, if not all, fundamental processes of genome processing and maintenance. Examples include nucleosomes and their higher order assemblies and various filamentous structures involved in DNA processing and repair. Finally, MT measurements will increasingly contribute to our understanding of the dynamic processes and molecular machinery at the heart of the central dogma.

New and exciting applications of MT are made possible by a number of dramatic improvements of the measurement capabilities of MT based assays in the last few years. First, the ability to directly measure torque and twist has been discussed in detail in this chapter. Second, improvements in camera hardware and tracking algorithms [96, 146] have made it possible to perform massively parallel multi bead measurements, of up to 1000s of beads simultaneously[147–149]. Third, advances in camera hardware, GPU-based tracking, and novel approaches to illumination enable camera-based tracking at > kHz frequencies [32, 43, 150]. Forth, other technical improvements such as temperature control during MT measurements [103, 151], which is crucial for many biological systems, further enhance the capabilities of MT measurements. Finally, MT can be combined with other measurement modalities, such as optical tweezers[152] or fluorescence detection [96, 107, 153], enabling complementary types of measurements to, e.g., dissect the mechano-chemical of nucleic acid processing enzymes.

In conclusion, MT based measurements will continue down the path outlined in the Feynman's famous quote: Making new discoveries, enabling precision experiments, and pushing the limits of physical detection.

Acknowledgements

I thank Philipp Walker for sharing unpublished data on the DNA buckling transition and I acknowledge the tremendous research efforts by groups in the magnetic tweezers and nucleic acids communities.

Part II

Results

Chapter 2

Multiplexed Freely Orbiting Magnetic Tweezers and Force Calibrations

Abstract

DNA is a very stable and reliable macromolecule that is used for years in single-molecule measurements to test mechanical properties. Recent techniques such as freely-orbiting magnetic tweezers (FOMT) and magnetic torque tweezers (MTT) make possible to measure angular changes besides inducing force. So far molecular angular measurements are limited by a "one-molecule-at-a-time" method, lacking high statistics. This work presents a study on multiplexed FOMT using two different magnetic beads. To align the magnet assembly (used in FOMT) with the microscope, i.e. the objective's main axis, we first perform a coarse alignment method and find that this is sufficient for the smaller beads (1 μm diameter) used in this study. However, for the larger beads (2.8 μm diameter) we have to perform a fine tuning method to at least align a single magnetic bead in FOMT. By attaching a small, cylindrical side magnet to the FOMT magnet configuration, we transform the setup to multiplexed magnetic torque tweezers. Finally, we compare force calibrations performed on both beads and in both configurations and find that these are similar in FOMT and MTT.

2.1 Introduction

Magnetic tweezers (MT) are a powerful technique to study mechanical properties of - or to study interactions of proteins with - nucleic acids [1, 11, 30, 31, 122, 123]. A number of MT studies focus on bare DNA molecules to probe mechanical properties, such as the bending persistence length [49, 58–61, 124] or the torsional stiffness [38, 49, 76]. Others use MT to probe interactions of DNA with proteins [47, 133, 138] or small molecules [124, 125]. In particular freely orbiting magnetic tweezers (FOMT) that enable measuring angular changes within the DNA tether, and magnetic torque tweezers (MTT) that additionally allow inducing twist, recently established [34, 36, 38, 132]. FOMT enabled, for example, studying the assembly of nucleosomes on DNA [138] and resolved changes in the tether extension and the handedness of tetrasomes. Transcription of DNA by RNA polymerase and the related rotation of the DNA

tether was observed with the rotor bead assay, a variation of FOMT [133]. However, the handling of proteins is often complex and not easy, making protein-nucleic acid interactions more difficult to study compared to "only DNA" measurements. The more complex the biological question the more important is a reliable and good working instrument. Multiplexed measurements help to increase statistics and to then carefully probe changes in tether length and in particular in the rotation angle. Tracking of many beads in parallel is possible and presented in earlier studies , like in highly parallel conventional MT [2, 147–149]. However, a proper analysis of the behavior of many molecules in parallel in FOMT or in MTT has not been done yet.

The main difference lies in the overall magnetic field component that is predominantly vertical in both configurations (FOMT and MTT), in contrast to conventional MT with a predominantly horizontal magnetic field (see also Chapter 1 and Figure 1.1 for a comparison of the magnetic fields). In this work, a multiplexed study on FOMT is presented, taking two types of magnetic beads (typically used in MT) into account, MyOne and M270 beads. We find that coarse alignment is sufficient to have multiple MyOne beads aligned in parallel, whereas fine alignment is necessary to align at least a single M270 bead correctly in FOMT. This is contrary to MTT, where both beads can be used in a parallelized fashion. Moreover, we present that force calibrations in FOMT and MTT are similiar for both types of magnetic beads.

2.2 Materials and methods

Instrument and measurement details given here hold for all chapters of this thesis if not stated different. *

2.2.1 Magnetic tweezers setup

Measurements were performed with a home-built magnetic tweezers setup. In brief, a light emitting diode (Osram Oslon SSL, red, 165lm) is used to illuminate the sample, monochromatically from above. An oil immersion objective (60x, Plan Fluorite with correction collar, NA 0.9 or 40x, Plan Fluorite, NA 0.75, Olympus) is placed on a piezo (Pifoc, P-726.1CD and controller, E-753.1CD, Physik Instrumente) stage underneath the flow cell holder. The flow cell is imaged with a mirror (20D20ER.1, Newport) and tube lens (G322304000, Newport) onto the chip of a camera (Falcon PT-41-4M60, Dalsa). Magnets (see below) are placed on a motorized arm, using a translational motor (C-863.11-Mercury controller and M-126.PD2 motor, Physik Intsrumente) and a rotational motor (C-863.11-Mercury controller and C-150.PD motor, Physik Intsrumente) to control the magnets' rotation and position in Z. The flow cell outlet is connected to a pump (ISM832C, Ismatec) for fluid handling [154]. The setup is controlled using a computer (DELL Precision T3600) equipped with a framegrabber (PCIe-1433, National Instruments) and using software written in LabVIEW (National Instruments) described by Cnossen *et al.* [147]. The size of the field of view (FOV) is 190 x 260 μm with 60x magnification (60x, Plan Fluorite with correction collar, NA 0.9, Olympus) used for measurements with MyOne beads (streptavidin-coated 1.0 μm diameter MyOne, Life Technologies). Measurements with M270

*The section about materials and methods was adapted from Kriegel *et al.* [2]. This is an open access article distributed under the terms of the Creative Commons CC BY and adapted with permission from Oxford University Pres, Copyright ©2017.

beads (streptavidin-coated 2.8 μm diameter M270 beads, Life Technologies) were performed with 40x magnification (40x, Plan Fluorite, NA 0.75, Olympus), resulting in a FOV of 400 x 300 μm.

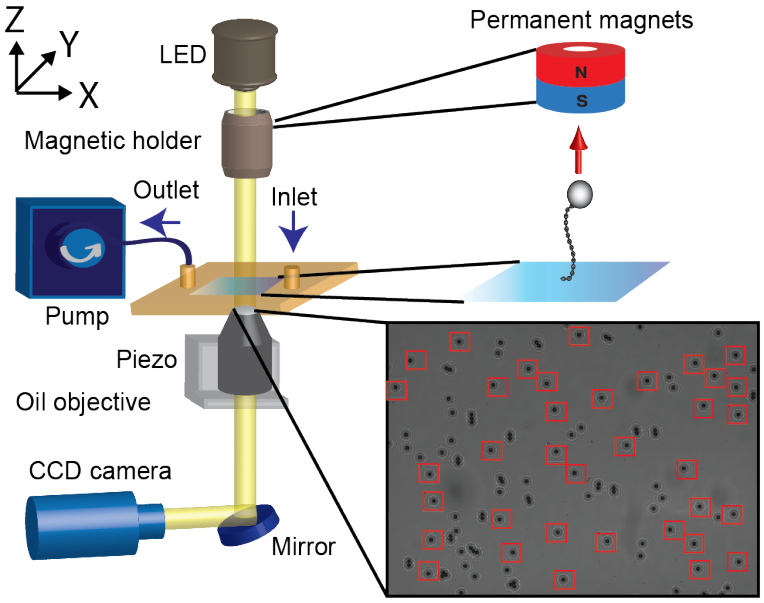

Figure 2.1: Schematic of a magnetic tweezers setup. An inverted microscope and a camera are used to image the magnetic particles attached to the DNA tethers, which are illuminated by monochromatic light from above. The objective is placed on a piezo to collect a stack of calibration images of the diffraction pattern of the bead at different magnet heights, which is in turn used to track the bead in Z. Tracking algorithms for X,Y and Z are described by Cnossen *et al.*[147]. Buffer conditions are controlled using a pump that is connected to the flow cell. The setup can be converted from conventional MT to FOMT or MTT (and vise versa) by changing the magnet configuration.

2.2.2 Preparation of the flow cell

Two glass cover slips (24 x 60 mm, Carl Roth) separated by a single parafilm layer (PARAFILM, H666.1, Carl Roth) comprise a measurement chamber and form a flow cell (FC). The upper cover slip is prepared such that it has two holes for the in- and outlet of liquids. The bottom cover slip is coated with (3-Glycidoxypropyl)trimethoxysilane (abcr GmbH). First the FC is supplied with anti-digoxigenin (100 μg/mL in 1x PBS; Roche) and incubated for at least one hour. Remaining liquid is removed by excessive flushing with ~500 μL phosphate buffered saline (PBS; Sigma-Aldrich). Second, BA (BlockAid™ Blocking Solution, Thermoscientific), a solution to passivate the FC is inserted for at least an hour. Remaining solution is removed by flushing with ~500 μL PBS buffer. After excessive flushing of the flow cell, the DNA-bead solution is introduced and allowed to bind for ten minutes (MyOne beads) or 50 seconds (M270 beads). Unbound beads are removed from the flow cell by flushing with ~500 μL PBS.

2.2.3 DNA construct and beads for MT measurements

Measurements used a 7.9-kbp DNA construct as previously described [34]. Specific and torsionally constrained coupling of the DNA to magnetic beads (streptavidin-coated 1.0 μm diameter MyOne or 2.8 μm diameter M270 beads; Life Technologies) and the flow cell surface was achieved through ligation with ~600-bp PCR-generated DNA fragments, comprising multiple biotin- and digoxigenin-modified dUTP moieties (Jena Bioscience), respectively. The DNA construct was first coupled to the streptavidin-coated beads by incubating 5 ng of the DNA construct with 2 μL of MyOne (or 5 μL M270) beads in a final volume of 20 μL of PBS for 12 minutes (5 minutes for M270 beads). The DNA-bead solution was subsequently diluted into 100 μL PBS and introduced into the flow cell. Finally, 60 μL of the DNA-bead solution are inserted to the FC at 170 μL/min. After 7 minutes (40 seconds for M270 beads) unbound beads are removed by flushing with PBS buffer at 400 μL/min for 2 minutes (1 minute for M270 beads). Then, the magnet holder with magnets used in conventional magnetic tweezers (next paragraph) are introduced to the setup to exert stretching forces (2 pN for MyOne beads and 4 pN for M270 beads).

2.2.4 Bead selection with conventional magnetic tweezers

To verify that selected beads are bound to a single, torsionally constrained DNA tether, several tests were performed using conventional MT that employed a pair of cubic permanent magnets (5 x 5 x 5 mm3; W-05-N50-G, Supermagnete), oriented in a vertical configuration [42] with a spacing of 1 mm. Force calibrations in conventional MT were performed as described in reference [44] and are not part of this work. First, the external magnets are moved vertically to exert alternating forces of ~5 pN (to fully stretch the molecule) and < 0.01 pN (close to zero force) in order to test the contour length of the tethers. The measured change in extension is expected to be approximately the contour length of the DNA double-strand. Next, magnets are rotated counterclockwise by 20 turns at high (5 pN) tension to test for multiple tethers: At forces > 1pN, DNA does not form plectonemic supercoils upon unwinding (corresponding to counterclockwise rotation), but melts instead [99] and no decrease in the extension is expected for single DNA tethers. In contrast, if a bead is attached via two or more double-stranded DNA molecules, the molecules will form braids if the bead is rotated, causing a decrease in the molecule's extension, independent of stretching force. To select for beads that are coilable (i.e. with a fully double-stranded backbone and attached via multiple attachment points at both ends) magnets are rotated by 20 turns in both directions at 0.6 pN to check for DNA supercoiling, which is seen in a decrease in the detected extension. Finally, the flow cell is flushed with ~500 μL of the appropriate measurement buffer (here PBS).

2.2.5 Freely orbiting magnetic tweezers

Preparation of the FC and bead selection is generally performed with conventional MT. For FOMT studies, the magnet assembly used in conventional MT is replaced by a stack of ring-shaped magnets (R-06-02-02-G, Supermagnete) to induce a predominantly vertical magnetic field. This stack consists of three ring magnets with an outer diameter of 6 mm, an inner diameter of 2 mm and a height of 2 mm per magnet. Magnets where not brought closer to the FC than 3 mm. For the force calibration and the analysis of the X,Y-fluctuations in freely orbiting

magnetic tweezers (FOMT), measurements were performed at 3, 3.5, 4, 4.5 and 5 mm distance for 600 seconds for MyOne beads and 1200 seconds for M270 beads, corresponding to measurements several times longer than the characteristic time of the system. The characteristic time (τ_C) is defined through the quotient of the friction coefficient (γ) of the solution and the stiffness of the trap (k) in which the bead is captured. This, in turn depends on the viscosity of the solution, the radius of the bead and the applied force. At 1.5 pN, τ_C is approximately 76 seconds for MyOne beads (1 μm diameter) and 250 seconds for M270 beads (2.8 μm diameter) [36] for these conditions.

2.2.6 Magnetic torque tweezers

To further transform the instrument to magnetic torque tweezers (MTT) a side magnet is added to the stack of cylindrical magnets used in FOMT. This side magnet is a cylindrical magnet with a diameter of 3 mm and a height of 6 mm (S-03-06-N, Supermagnete). To determine the trap stiffness of each individual bead in MTT the X,Y-fluctuations were measured for 600 seconds at each magnet height (3, 3.5, 4, 4.5 and 5 mm). Additionally at each force (i.e. magnet height) six rotations at 0.1 turn per second were performed. The measurement frequency is 60 Hz.

2.3 Results and discussion

2.3.1 Setup alignment in freely orbiting magnetic tweezers

From the geometry of the magnets used in FOMT, with an inner diameter of 2 mm, we expect the perfect aligned situation (no radial field component) if the objective's main axis is in line with the magnet's main axis. To find this configuration, we take advantage of the beads characteristic transverse fluctuations in the X,Y-plane that trace out a doughnut-like shape for a purely vertical magnetic field when recording several characteristic times of the system (see also Chapter 1 and Figure 1.1G).

"Coarse Alignment": To start, one can take advantage of the light path of the microscope to align the magnet with the objective. A light emitting diode (LED), which is placed just above the motorized arm that carries the magnet, emits parallel light through the magnet configuration (see Figure 2.1). The instrument offers the opportunity to change the relative position of magnet and objective by moving the arm, which carries the magnet holder and the light emitting diode, in X and Y direction. By varying the X and Y position we place the magnets and thus the diode such that we record maximal light intensity (on average) over the FOV ("light alignment"). To check the effect of the magnetic field on the magnetic particles, we then record the fluctuations of all beads within the FOV and analyze their movement in the XY-plane at a fixed magnet height (here 3 mm). The aim is to have as many beads as possible fulfilling closed circular traces, i.e. doughnut-shapes, within the FOV.

"Fine Alignment": By varying the position of the arm (using micrometer screws with $<$100 μm accuracy) that carries the magnet and the diode, one can maximize the number of aligned beads (i.e. beads that trace out a full circle when recording the XY-fluctuations at a given force for several times of the characteristic time of the system) within the field of view (FOV). However, when plotting the recorded X,Y-trace of a particular bead binned in a heat

map, we find that a full circle in the X,Y-plane not necessarily determines the position of perfect alignment, i.e. fluctuations in a harmonic potential. To find a perfect aligned bead that fulfills the criteria to rotate about the tether axis in a harmonic distribution, it is best to focus on a single bead instead of many in parallel. To further adjust the fluctuations of a single bead, one can re-locate the bead's position relative to the magnetic field by trans-locating the position of the whole flow cell (FC) using micrometer screws with <10 μm accuracy.

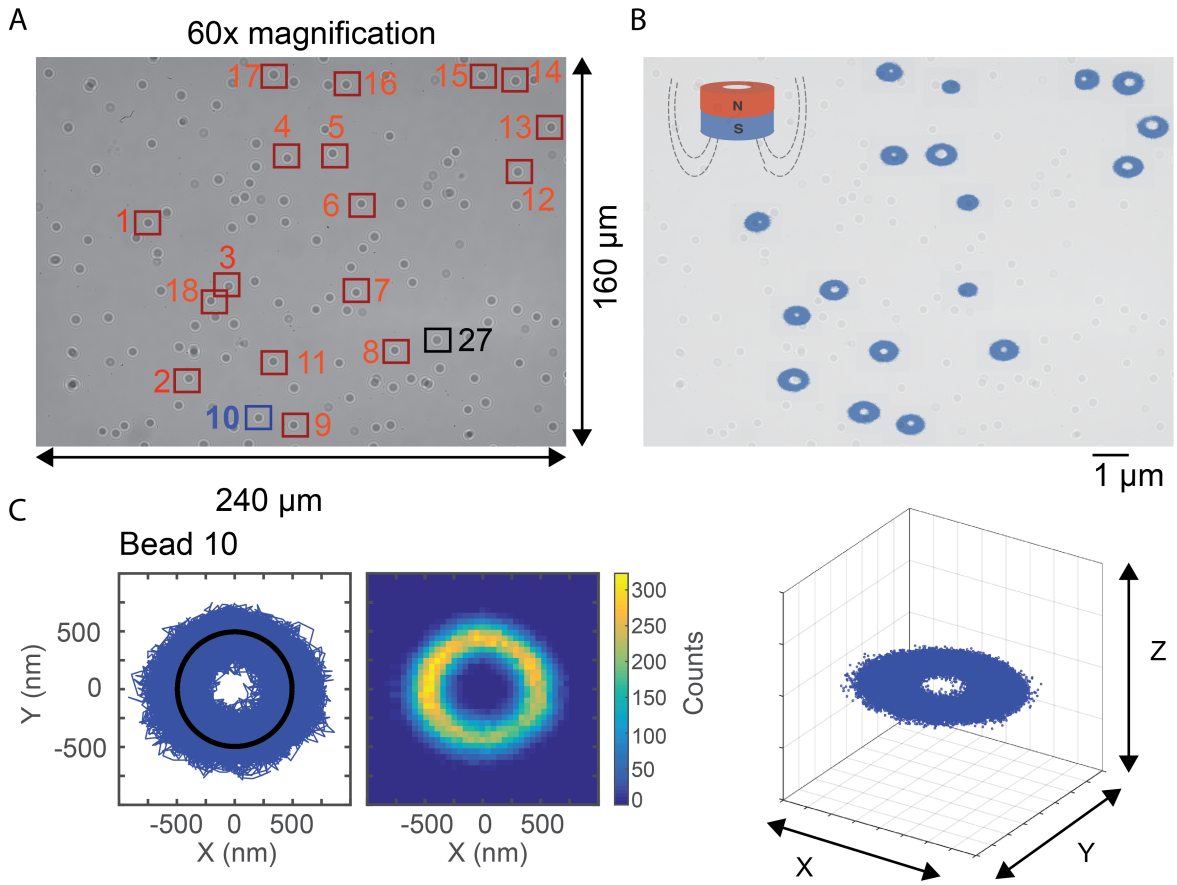

Figure 2.2: (A) Multiplexed field of view in magnetic tweezers using 60x magnification. Red squares indicate beads that were preselected using conventional MT to check for tether length, coilable molecules and against multiple tether. Indicated in black is the reference bead. (B) Measured fluctuations in the X,Y-plane of 7.9 kbp DNA attached to MyOne beads in PBS at 3 mm magnet height in FOMT. Fluctuations shown, were recorded for 600 seconds. Scale bar shows one micrometer and refers to the magnified fluctuations of the beads (blue). No smoothing was performed on the data. (C) X,Y-fluctuations for one particular bead (Bead 10 in A, blue). The heat map shows that the fluctuations of the bead are harmonically distributed around the tether axis. A 3D plot with 1 μm scaling in each dimension shows that Z is unaffected by the radial fluctuations.

For both procedures (**"Coarse Alignment"** and **"Fine Alignment"**) a careful and systematic protocol is recommended. Once the position of the arm that carries the magnet configuration and the LED results in a maximal number of aligned beads, the position can be fixed. There is no need to change this position when changing the magnet assembly back to a conventional MT configuration. Notably, to maximize the amount of aligned beads within the FOV, due to a large bead-to-bead variation [45], it is recommended to perform fine alignment just before every measurement in FOMT.

2.3.2 Multiplexed freely orbiting magnetic tweezers

Studying MyOne beads

Figure 2.2 illustrates FOMT data for 7.9 kbp DNA and MyOne beads at 3 mm magnet distance. Several magnetic beads are tracked in parallel (Figure 2.2A) within the FOV (240 μm x 160 μm). Red squares indicate beads that were preselected in conventional MT, i.e. beads that are tethered with a single and coilable DNA molecule. The black square indicates the reference bead, which is a bead unspecific stuck to the surface. The recorded data and movement of the reference bead is subtracted from the recorded data of all beads to correct for i.e. drift in further analysis. Shown in Figure 2.2B are the recorded fluctuations of the beads in the X,Y-plane after **"Coarse Alignment"**.

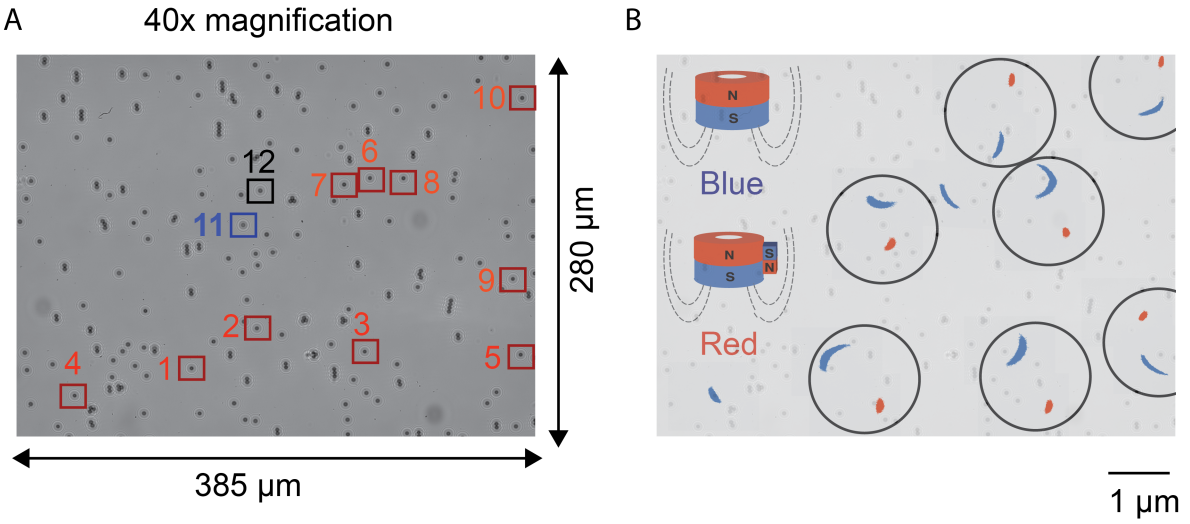

Figure 2.3: (A) Multiplexed field of view in magnetic tweezers using 40x magnification. Red squares indicate beads that were preselected using conventional MT to check for tether length, coilable molecules and against multiple tether. Indicated in black is the reference bead. (B) Measured fluctuations in the X,Y-plane of 7.9 kbp DNA attached to M270 beads in PBS at 3 mm magnet height in FOMT (blue) and MTT (red). Insets illustrate the used magnet configuration. Fluctuations shown were recorded for 1200 seconds. Scale bar shows one micrometer and refers to the magnified fluctuations shown (blue for FOMT and red for MTT). Data performed on the same bead (FOMT and MTT) is taken together in the black circle. No smoothing was performed on the data.

Fluctuations of all measured beads are indicated in blue and expanded for illustration. We can conclude that several beads (here MyOne) trace out a full circle, independent of their position within the FOV. The transverse fluctuations vary from bead-to-bead, in particular, in the size of the radius, which is understood by the attachment point between the DNA molecule and the magnetic bead, which is not controlled during sample preparation. Performing a 2D binning on the recorded data of the X,Y-trace allows plotting an illustration of the data in a heat map. We find that Bead 10 (Figure 2.2C) and Bead 11 fluctuate in a harmonic potential around the tether axis (middle column), whereas there is some asymmetry in the radial fluctuations for all other beads. Bead 10 and Bead 11 are located close to each other within the FOV (Figure 2.2A) leading to the assumption that the perfect aligned position (no radial field component) is located there. Note, that performing such a binning is necessary in order to figure out whether the bead fluctuates in a harmonic potential (Figure 2.2C, middle column) or not. However,

bead-to-bead variations are large, such that the results of the X,Y-fluctuations of different beads at the same position were never identical. This result is further established in a study about multiplexed magnetic torque tweezers and is further discussed in Chapter 3. We understand this effect in the overall magnetic content of the beads, i.e the beads anisotropy [45]. Figure 2.2C, right column shows a 3D plot of the recorded fluctuations of Bead 10, that fluctuates in a harmonic potential. Notably, the trace of the magnetic particle is almost unaffected along the tether extension (i.e. the Z-axis), leading to the conclusion that the fluctuations occur purely around the tether axis, i.e. the predominant vertical magnetic field.

Studying M270 beads

The position of the magnet holder determines the strength as well as the direction of the magnetic field across the FOV relative to the objective. Previously, we defined a position of the magnet relative to the objective that results in a maximum number of aligned MyOne beads. Therefore, we continue with this setup configuration and perform a measurement with 7.9 kbp DNA attached to M270 beads and again observe the fluctuations at 3 mm magnet distance. Shown in Figure 2.3A are the preselected beads with conventional MT. In Figure 2.3B the fluctuations of the beads are displayed offset and expanded for illustration (blue colors). None of the beads traces out a full circle. Instead, all beads trace out arc-like shapes. The recorded fluctuations are not oriented in the same direction, such that we can conclude that this is not an effect of the magnetic field but from the beads magnetization itself [45]. Further, we continue to focus on one particular bead (here Bead 11, indicated in blue in Figure 2.3A).

We carefully change the relative position of the magnetic bead to the magnet, as explained previously (**“Fine Alignment”**) and observe the fluctuations in the X,Y-plane. An optimization of the relative position of the bead via **“Fine Alignment”** enables us to align a single bead, i.e. to make a bead perform a full circle, see Figure 2.4. M270 beads are very sensitive to the position of the external, permanent magnet. Careful alignment is required to align a single M270 bead (see Figure 2.4A), while a perfect alignment is barely reached, as seen from the deviation of the fluctuations from a harmonic distribution (see Figure 2.4C). Other than for MyOne beads the X,Y-movement of M270 beads is affected in Z (Figure 2.4D). This effect is not observed for all beads and has no consequences on force calibrations as will be discussed in Section 2.3.4.

In order to vary stretching forces, the distance between magnet and bead is changed [42]. If the bead’s main axis is perfectly aligned with the magnetic field, i.e. no radial field component (definition of “perfect alignment”), a change of the magnet height is supposed to not change the magnetic field direction, but only the strength. With increasing the distance between magnet and flow cell, the force acting on the magnetic bead decreases. This leads to increased fluctuations of the bead around the tether axis, i.e the variance of the radius increases (see also the next section about force calibrations). Figure 2.5A, shows the radial fluctuations of Bead 11 at different magnet heights (3 mm, 3.5 mm, 4 mm, 4.5 mm and 5 mm). Note, that the fluctuations in Figure 2.5A have been centered for clarity, such that they fit perfectly on top of each other, indicating that the radius of the X,Y-fluctuations stays constant, while the magnitude of the fluctuations increase.

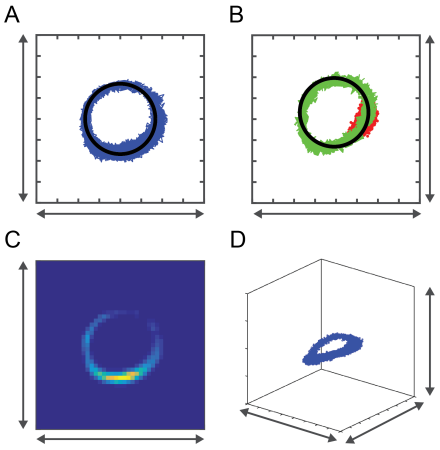

Figure 2.4: (A) Fluctuations of a single aligned M270 bead in FOMT. (B) The same bead in MTT (red). Green displays the bead's trace when turning the magnet assembly six times at 0.1 turn per second. (C) Data as in A, plotted in a heat map. (D) The same data as in A and C, plotted in 3D. Measurements were performed in PBS buffer. Magnets were placed at 3 mm distance to the FC surface. Arrows indicate 2 μm and measurements were performed for 1200 seconds.

In fact, when changing the magnet height from for example 3 to 3.5 mm, the previously aligned bead does not trace out a full circle in the X,Y-plane anymore (see Figure 2.5B). Instead, **"Fine Alignment"** is necessary to align the exact same bead on the doughnut-shape pattern by displacing the magnet arm relative to the objective (**"Fine Alignment"**) in the order of 50 to 100 μm.

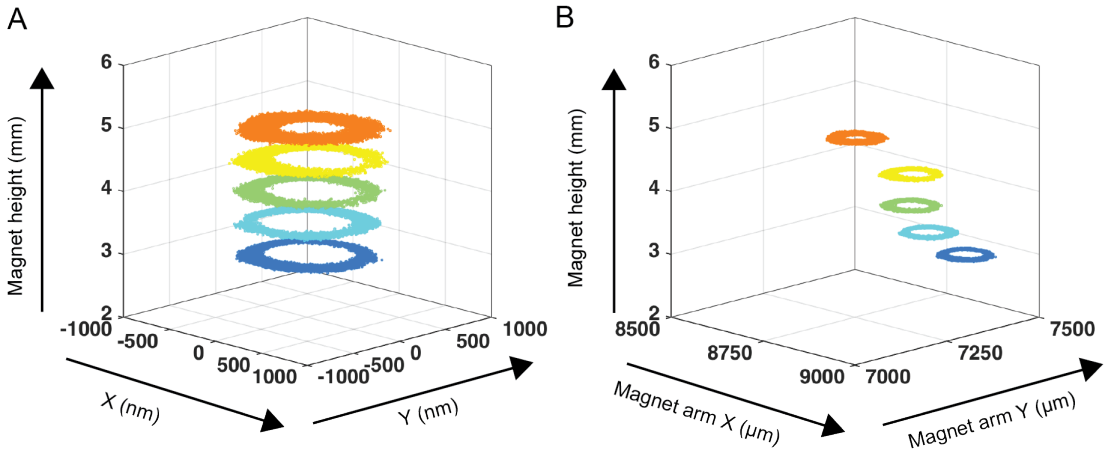

Figure 2.5: (A) An aligned M270 bead, centered to X and Y equal zero for illustration. Color code indicates different magnet distances (3, 3.5, 4, 4.5 and 5 mm). (B) Same data and color code as in A, but displayed relative to the position of the magnet arm in X and Y. Bead fluctuations appear 100x larger. Additional fine alignment is necessary when changing the distance between magnet and bead, i.e. the magnet height. Shown is the relative movement of the aligned bead relative to the magnet at different magnet heights.

Comparison

In summary, using a coarse-grained method to align the magnet with the objective is sufficient to align several MyOne beads at the same time in a FOV. Using additional fine alignment allows us to further maximize the amount of aligned beads by trans-locating the magnet arm with micrometer screws. One can find a single or even more beads that rotate freely (i.e. in a harmonic distribution) around the tether axis. Studying M270 beads in the same way does not give similar results. Coarse alignment is not enough to find an aligned M270 bead and it is not possible to align more than one M270 bead in a FOV. Furthermore, a different bead at exactly the same position does not give identical results, indicating that the bead-to-bead variation is large for M270 beads.

2.3.3 Multiplexed magnetic torque tweezers

FOMT does not allow inducing rotations on magnetic beads and such the DNA tether. Therefore, multiplexed MTT are an extension of multiplexed FOMT. Here, we add a side magnet (see materials and methods) to the FOMT magnet configuration to induce this effect, see inset in Figure 2.6A. The side magnet affects the bead's fluctuations: While the bead is free to rotate about the tether axis in FOMT, the bead is captured in a rotational trap in MTT. This is due to a slightly tilted magnetic field in MTT compared with FOMT, i.e in addition to the predominant vertical magnetic field component in FOMT there is a small radial side component in MTT. Displayed in Figure 2.6A are the same beads as in Figure 2.2B. Shown are recorded fluctuations of the beads with side magnet added to the FOMT magnet configuration. All beads trace out arc-like shapes in the X,Y-plane and are oriented towards the addition of the side magnet. The size of the arc is a number for the stiffness of the rotational trap k_{ROT} and is defined through the strength and direction of the magnetic field, and the magnetic content of the bead. MTT exert stretching forces on the molecular tether and allow measuring angular changes within the molecule, similar to FOMT [36], additionally they allow inducing twist to the tether. Shown in Figure 2.6B are the fluctuations of one particular bead in MTT (red). When slowly rotating the magnet assembly at 0.1 turn per second, the bead follows the direction of the magnetic field and fulfills a turn with every rotation of the magnet (trace shown in green). Multiplexed torque measurements are discussed in detail in Chapter 3.

2.3.4 Force calibration

In FOMT and MTT it is useful to transfer the recorded X,Y-data to polar coordinates. In FOMT, we therefore fit a circle to the transverse fluctuations of the bead (Figure 2.2C, left column for MyOne and Figure 2.4A for M270), while in MTT we fit a circle to the recorded trace of the bead when turning the magnet configuration (Figure 2.6B for MyOne and Figure 2.4B for M270, green data) to determine a center point and such transfer the data to polar coordinates.

Using

$$F(Z_{mag}) = k_B T \cdot \frac{L(Z_{mag})}{Var(R(Z_{mag}))} \tag{2.1}$$

we performed force calibrations similar to Reference [36], where Z_{mag} indicates the magnet height, k_B the Boltzmann constant, T the absolute temperature, L(Z_{mag}) the measured tether

length and R(Z_{mag}) the determined radius in each point. Tether attachment differences that change L(Z_{mag}) are corrected as described by Lipfert *et al.* [36].

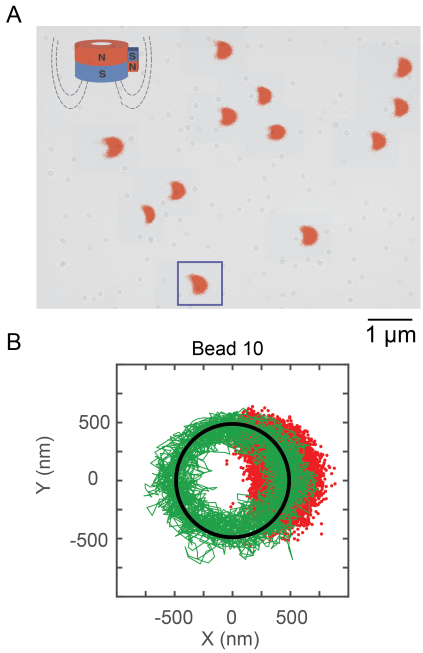

Figure 2.6: (A) Measured fluctuations in the XY-plane of 7.9 kbp DNA attached with MyOne beads in PBS at 3 mm magnet height in MTT. Fluctuations shown were recorded for 600 seconds. Scale bar shows one micrometer. No smoothing was performed on the data. Selected beads are the same as in Figure 2.2. The number of beads is reduced due to unspecific binding of beads to the surface over time. (B) When adding the side magnet to the cylindrical magnet, the bead is trapped in the magnetic field and its transverse fluctuations trace out an arc-like shape as indicated in red in the background. When rotating the magnet assembly at 0.1 turn per second, the bead follows the direction of the magnetic field and traces out a full circle (green).

Figure 2.7A, shows the mean and the standard error of the mean of the calculated forces (in sum 12 beads) for FOMT (blue) and MTT (red). The average difference between FOMT and the overestimated forces in MTT is about 6.5%. In Figure 2.7B we compare the mean of the radius determined in FOMT (blue circles) with MTT (red circles) at Z = 3 mm for MyOne beads and find good agreement between both. For the force calibration, however, the variance of the radius is taken into account (see Eq. 2.1), which is smaller for MTT than for FOMT (Figure 2.7B, bottom). This leads to a systematic error on the force (Figure 2.7A), which is understood by the methods used to determine the radius R: When using the transverse fluctuations as in FOMT, data is recorded for several characteristic times of the system. Whereas in MTT, the bead is forced to make full turns by rotating the magnets several times (here six times). Due to the rotational trap, which enables the ability to turn the beads, the bead's fluctuations are confined, leading to a smaller variance in the radius. This, however, leads to slightly larger calculated forces when using MTT data compared to FOMT but sill within error. The force range for MyOne beads, for the here tested magnet heights, is between ~0.3 pN and 1.1 pN (Figure 2.7A).

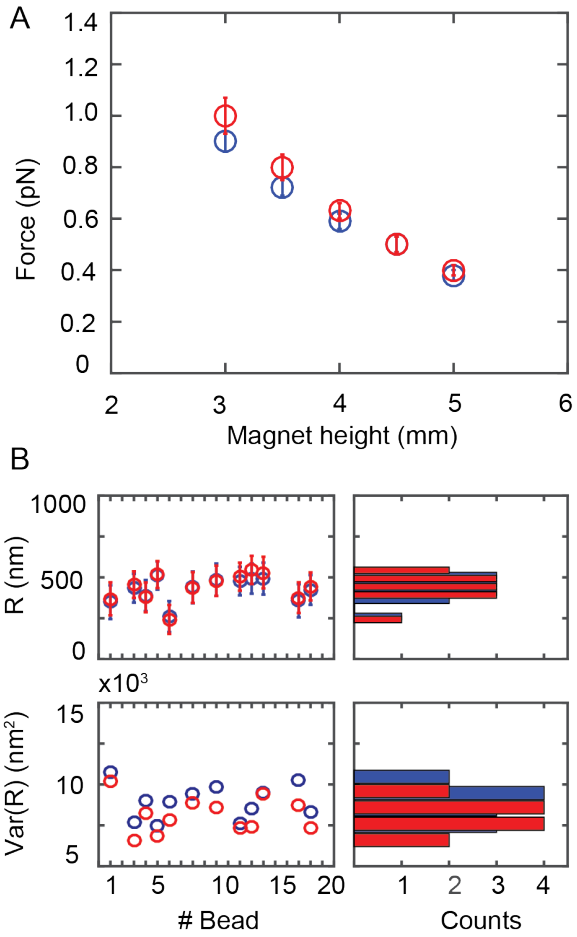

Figure 2.7: Force calibration for MyOne beads. (A) Calibrated force for MyOne beads at 3, 3.5, 4, 4.5 and 5 mm using FOMT (blue circles) and MTT (red circles). (B) Mean of the determined radius at each point and for each bead in FOMT (blue circles) and MTT (red circles) with the standard deviation as error bars and histograms with a binning of 50 nm. Corresponding variance of the radius in FOMT vs. MTT (same color code as before) with a binning of 1000 nm^2.

In this work, we use larger beads (here M270 beads, with a greater volume and such a larger magnetization) in order to reach higher stretching forces in measurements. Force calibrations and measurements are as previously described for MyOne beads. To calibrate the forces for M270 beads, we first focus on a single bead (Bead 11), see Figure 2.8A and find good agreement between FOMT and MTT, in particular, when assuming an error of 10% on average (as displayed within the Figure) on the forces.

Due to the fact that it is impossible to align several M270 beads at the same time in FOMT, we can only use a single bead to calibrate the force (Bead 11). The advantage of using MTT over FOMT for M270 beads is that one can measure several beads in parallel to calibrate the stretching force. In Figure 2.8B (red) we show averaged force calibrations for seven beads of M270 as determined by MTT. Co-plotted for comparison is the force calibration of Bead 11 in FOMT (same data as in Figure 2.8A).

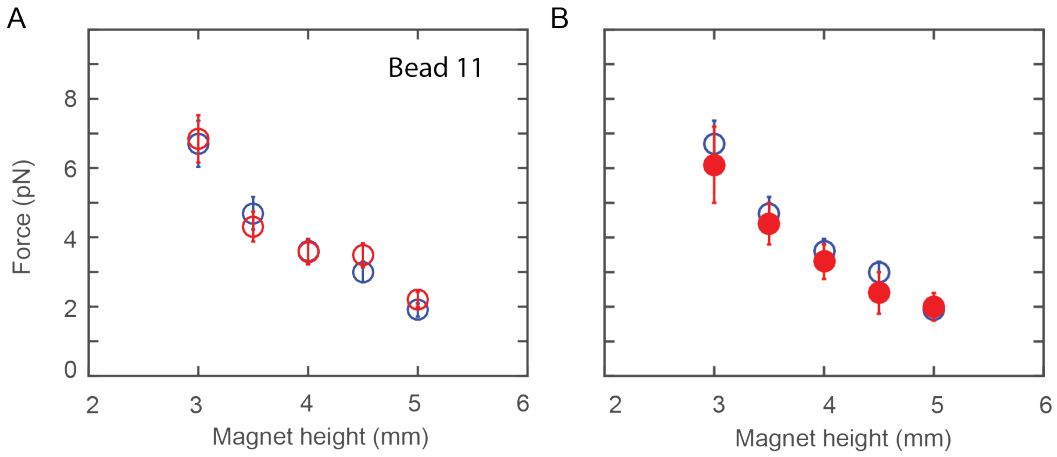

Figure 2.8: Force calibration for M270 beads. (A) Calibrated force for one particular M270 bead (Bead 11) at 3, 3.5, 4, 4.5 and 5 mm using FOMT (blue circles) and MTT (red circles). (B) Blue circles are the same data as in A. Red-filled circles show averaged force calibrations for seven beads determined in MTT. Error bars display the standard error of the mean (SEM). Measurements were performed in PBS and data were recorded for 300 seconds in FOMT and for six turns at 0.1 turn per second in MTT.

The overall force range for FOMT and MTT using the magnets described in this work in combination with MyOne and M270 beads lies between 0.4 and 6.5 pN. This force range covers all relevant forces to study for example DNA supercoiling, torque-induced melting upon underwinding DNA at medium force (>1 pN) and the transformation from B-DNA to P-DNA upon overwinding at high stretching force (>6 pN). Note, that the gradient of the magnetic field changes its sign in FOMT and such MTT close to the flow cell surface, which leads to a critical magnet distance upon which stretching forces transform to pushing forces [36, 38], thus rationalizing the magnet distance chosen in this work.

2.4 Conclusion

Larger camera chips and smaller magnification support tracking of many particles in parallel. However, in FOMT and MTT, the predominant vertical magnetic field component makes multiplexing more difficult compared to conventional MT. We experimentally demonstrated that multiplexed FOMT is easily realized for MyOne beads using only a coarse-grained alignment of the setup. For larger beads (M270 beads), we find that fine alignment of the setup is necessary to align a single bead within the FOV. Adding a permanent side magnet to the FOMT magnet configuration transforms FOMT into MTT. The overall effect on the magnetic beads is similar all over the FOV allowing for multiplexed torque measurements (see Chapter 3). On the one hand, force calibrations in FOMT can be used for MTT. On the other hand, force calibrations can be performed in MTT itself. There are several studies to come with multiplexed FOMT, like monitoring the assembly of several nucleosomes on bare DNA and the formation of a nucleosome fiber. Another idea is to observe intercalation of Ethidium bromide or other small molecules to DNA in real-time. Multiplexed torque tweezers help to study, in particular, torsional properties of DNA and RNA. A study to come is the temperature dependence of the torsional stiffness of DNA (see also Chapter 6) or a study on torque- induced binding, as expected from intercalating small molecules, like Etbr.

Chapter 3

Probing the Salt Dependence of the Torsional Stiffness of DNA by Multiplexed Magnetic Torque Tweezers *

Abstract

The mechanical properties of DNA fundamentally constrain and enable the storage and transmission of genetic information and its use in DNA nanotechnology. Many properties of DNA depend on the ionic environment due to its highly charged backbone. In particular, both theoretical analyses and direct single-molecule experiments have shown its bending stiffness to depend on salt concentration. In contrast, the salt-dependence of the twist stiffness of DNA is much less explored. Here, we employ optimized multiplexed magnetic torque tweezers to study the torsional stiffness of DNA under varying salt conditions as a function of stretching force. At low forces (< 3 pN), the effective torsional stiffness is ~10% smaller for high salt conditions (500 mM NaCl or 10 mM $MgCl_2$) compared to lower salt concentrations (20 mM NaCl and 100 mM NaCl). These differences, however, can be accounted for by taking into account the known salt dependence of the bending stiffness. In addition, the measured high-force (6.5 pN) torsional stiffness values of C = 103 ± 4 nm are identical, within experimental errors, for all tested salt concentration, suggesting that the intrinsic torsional stiffness of DNA does not depend on salt.

3.1 Introduction

DNA is the carrier of genetic information in all cellular life. In addition to its sequence, its polymeric and mechanical properties are critical for its biological function. For example, in our cells ~2 m of DNA are packed into a ~10 μm-sized nucleus [155], involving a multitude of deformations and DNA-protein interactions. In vivo DNA is negatively supercoiled and both

supercoiling and DNA packing play important roles in gene regulation [6, 8, 10, 156–158]. In addition to its biological role, DNA is emerging as a building block for artificially created 3D nanostructures [22]. A detailed and quantitative description of DNA mechanical properties is a prerequisite to understanding its biological roles and for its optimal use as a construction material at the nanoscale. At length scales significantly longer than one base pair, DNA is commonly modeled as an isotropic elastic rod, with a bending persistence length A, stretch or Young's modulus B, torsional stiffness C, and twist-stretch coupling D [1, 159]. All four elastic constants have been determined for DNA in vitro in a series of ingenious single-molecule manipulation measurements [33, 34, 46, 55, 71, 76, 84, 85, 110, 142]. However, their values, in general, can depend on solution conditions. In particular, salt concentration can strongly modulate DNA properties, as DNA is highly negatively charged [160]. In a classic argument, Odijk [62] and independently Skolnick and Fixman [63] derived how electrostatic repulsion increases DNA bending stiffness, A, and how the bending persistence length can be separated into a salt-independent and a salt-dependent contribution. Subsequently, single-molecule stretching experiments have determined the salt dependence of A for DNA [58, 60] and recently also for RNA [49, 61] and indeed found a reduction of A by ~20% going from low (< 20 mM monovalent salt) to relatively high (> 300 mM monovalent or ~10 mM divalent salt) ionic strength. However, the exact nature and molecular details of this dependence remain an area of active research [64, 65, 161–169].

The essence of the Odijk and Skolnick-Fixman argument is that bending a charged rod will bring charges into closer proximity, which will cost more energy if there are fewer screening counterions and, therefore, the stiffness will be increased at low salt. In contrast, for a homogenously charged rod, twisting the rod does not alter the distance between charges, which would suggest the twist-stiffness not to depend on salt. For real molecules the charges are localized, though; in DNA, the phosphate groups carry the negative charges under physiological conditions and it is not a priori clear whether the torsional stiffness would depend on salt. Several properties of DNA under torsional constraint, in particular aspects of DNA supercoiling, are known to strongly depend on salt concentration [94, 96, 170, 171]. Under sufficient torsional stress, DNA undergoes a buckling transition and forms plectonemic supercoils. Due to electrostatic repulsion, the diameter of plectonemic supercoils increases with decreasing salt concentrations [79, 93, 172, 173]. In addition, the critical linking number for buckling [76, 174], the number of plectonemes [97, 102], as well as their dynamics [96] have all been found to depend on salt concentration. However, plectonemic supercoils involve strong bending and bring DNA segments into close proximity and these observations, therefore, do not directly probe the torsional stiffness in isolation. Neukirch suggested from theoretical analysis of magnetic tweezers (MT) measurements on supercoiled DNA that the torsional stiffness of DNA decreases almost two-fold upon addition of millimolar concentrations of Mg_2^+ ions [172]. Similarly, direct torque measurements using a rotor bead assay suggested a small decrease of the torsional stiffness with increasing ionic strength (~10% in going from buffer only to ~150 mM monovalent salt and no additional decrease, within experimental error, upon further addition of ~1.8 M monovalent salt; at 10 pN stretching force) [48]. In contrast, Delrow *et al.* found an increase in torsional stiffness in FPA measurements by ~20% upon addition of 5 mM Mg_2^+ [175]. Finally, indirect torque measurements by thermodynamic integration [76] and Monte Carlo modeling [93] of MT measurements on supercoiled DNA concluded the torque at and past the buckling transition to depend on salt, but suggested little dependence of the

torsional stiffness on ionic strength. In summary, the dependence of the torsional stiffness of DNA on salt concentration and valence is currently debated, in particular due to the lack of systematic and direct measurements.

Here, we demonstrate multiplexed magnetic torque tweezers (mMTT) that enable parallelized single-molecule torque measurements. Using this experimental approach, we determine the torsional stiffness of DNA as a function of applied stretching force and salt concentration. Our mMTT instrument is an extension of conventional MT that have proven to be a powerful tool to investigate the torsional properties of nucleic acids [1, 11, 41]. In MT and mMTT, molecules of interest are tethered between a flow cell surface and magnetic particles (Figure 3.1). Bead positions are tracked by video microscopy, which enables tracking of many beads in parallel [147–149]. Stretching forces are applied by applying external magnetic fields that pull the magnetic particles upward. The forces can be calculated from the magnetic field gradients by taking into account the induced magnetization on the beads [42] and experimentally determined from analysis of the transverse fluctuations [28, 36, 41, 43, 176]. Conventional MT can apply torque by rotating the external magnetic field, which in turn rotates the beads, however, they do not measure torque. Torque measurements on individual DNA molecules in the MT have been achieved using an indirect approach by thermodynamic integration [76] and directly by tracking the rotation angle, either of a rotor bead [40, 46, 48, 84] or of the magnetic bead or assembly [33–35, 37, 38]. Our mMTT implementation employs an optimized angle tracking protocol and magnet geometry to extend the multiplexing capabilities inherent in MT measurement to the torque dimension.

3.2 Materials and methods

The magnetic tweezers instrument is described in Section 2.2.1. Experiments in this Chapter were performed with 7.9 kbp DNA coupled to MyOne beads (to reach forces ranging from 0.4 and 0.9 pN) and M270 beads (to reach forces ranging from 1 to 6.5 pN), see Section 2.3.4 for the force calibration. After preparation of the flow cell, the measurement chamber was flushed with ~500 μL of the appropriate buffer, see Table 3.1. Flow cell preparation, the DNA construct and magnetic beads are described in Section 2.2.2 and in Section 2.2.3, respectively. Bead selection is performed similar as explained in Section 2.2.4.

3.2.1 Magnetic torque tweezers configuration and measurement protocol

Conventional magnetic tweezers do not allow direct measurements of torque [34]; for single-molecule torque measurements the cubical magnets are, therefore, replaced by a set of cylindrical magnets (Figure 3.1A) that are assembled as a stack of 3 ring magnets with an outer diameter of 6 mm, a 2 mm diameter aperture in the center and a height of 2 mm per magnet (R-06-02-02-G, Supermagnete). A cylindrical magnet with 3 mm diameter and 6 mm height (S-03-06-N, Supermagnete) is used as a "side magnet". This magnet configuration exerts an upward pulling force [34, 36] while providing a weak rotational trap suitable for torque measurements. Details and optimization of the magnet configurations are further discussed below. Between rotating the magnets, we measured the angle fluctuations at a fixed number of applied turns for

100-200 s for MyOne and M270 beads. The characteristic time scales of rotational fluctuations are ~0.1 s and ~0.5 s for MyOne and M270 beads, respectively, in MTT representative for our conditions [34, 37, 38]. Our measurement intervals, therefore, correspond to > 100 times the characteristic time scale of angular fluctuations. We note that our camera integration time of ~17 ms (corresponding to the frame rate of 60 Hz) is significantly shorter than the characteristic time scale of rotational fluctuations, making blurring and aliasing effects negligible [176, 177]. The rotation speed of the magnets for under- and overwinding of the DNA tethers by integer number of turns during torque measurements was set to 0.1 Hz.

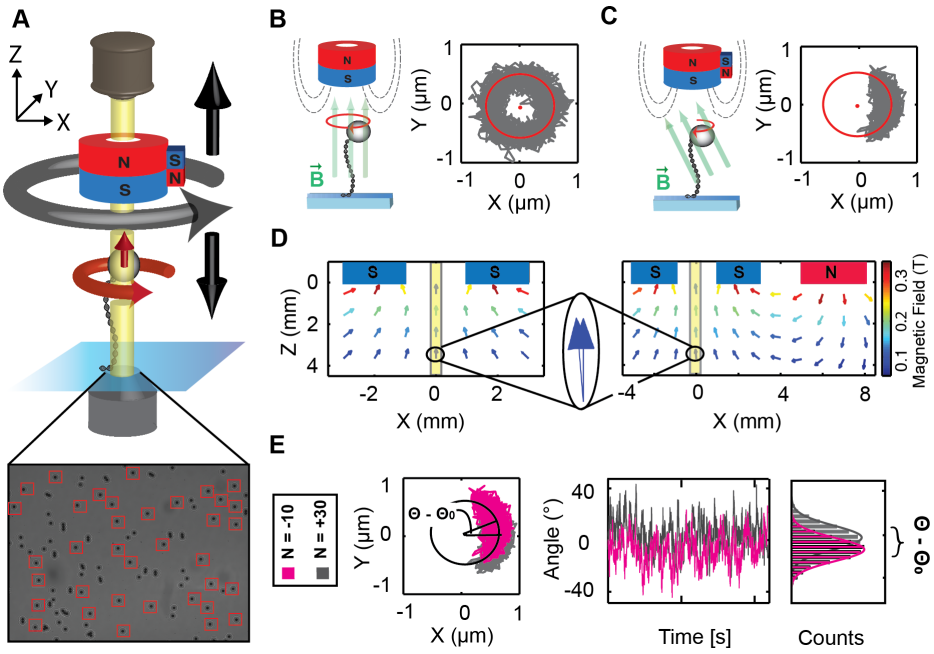

Figure 3.1: The principle of magnetic torque tweezers. (A) A schematic of mMTT. The molecules are tethered between magnetic beads and a glass coverslip. Permanent magnets, placed above the flow cell, exert magnetic fields, therefore enabling the application of forces and torques to the tethered molecules. The beads' positions are monitored by video tracking using an inverted microscope and monochromatic illumination. mMTT allow tracking of multiple beads in parallel (bottom left, red frames indicate beads marked for tracking), here 37 M270. (B) In FOMT, the bead's anisotropy axis aligns with the vertical magnetic field, exerted by the cylindrical magnets. The bead's motion is (torsionally) unconstrained and traces out a doughnut-like shape in the X,Y-plane. (C) An additional side magnet in the (m)MTT slightly tilts the magnetic field. This leads to (weak) angular trapping of the bead. Its motion in the X,Y-plane is confined to an arc-like shape. (D) Simulations of the magnetic fields for FOMT (left) and MTT (right) show that the difference in the magnetic field is small (large, blue arrows). The yellow shaded areas in the magnetic field simulations represent the width of the field of view. (E) The tracked X,Y-position of the bead is transferred to polar coordinates. Upon turning the magnets N times, the molecule exerts a restoring torque, causing a shift in the equilibrium position (θ - θ_0) of the rotation angle. Data shown are for F = 3.5 pN, going from N = −10 turns to N = +30 turns.

3.2.2 Data averaging of multiple single-molecule measurements

Torque measurements on dsDNA were performed for a range of forces and salt conditions (see Results and Figure 3.2 and 3.3). In order to improve the signal-to-noise ratio in the torque and extension vs. turns measurements, data for several independent DNA tethers were averaged for each condition. First, the responses of multiple DNA molecules to an applied number

of turns were collected and analyzed; subsequently, the curves were aligned to yield single, averaged extension-rotation and torque-rotation curves for each force and salt condition. For measurements at forces of < 1 pN, the rotation-extension curves are symmetric about zero turns (Figure 3.2A). For alignment, a Gaussian was fitted to the individual extension-rotation curves of independent DNA molecules (Figure 3.2C). The position of the maximum determined from the fit was defined as Lk0, the number of turns at which the molecule is torsionally relaxed. The extension-rotation and torque-rotation curves were shifted along the turns-axis by –Lk0 to center the curves before averaging. For the averaging of the extension curves at forces > 1 pN, a line was fitted to the constant region at negative turn values (Figure 3.2C). The first experimental value that fell below this line within experimental error was determined as the buckling point. Each curve was shifted along the turns-axis to align with the mean value of the buckling point of all measured DNA molecules for a given force and salt condition. Similarly, variations in the absolute extension of the molecule at zero turns were adjusted by shifting the curves. Finally, all curves for a given force and salt condition were averaged. For forces < 1 pN, the data where binned in bins of two turns prior to computing the standard deviation (STD) and standard error of the mean (SEM) for both torque and extension as a function of applied turns (Supplementary Figure 3.13). For forces > 1 pN, data were directly averaged (Supplementary Figure 3.14). Data points for each force and salt condition consist of at least 10 (and up to 45) independently measured molecules from at least two independent measurement runs, corresponding to an overall number of 475 measured molecules in this work. We note that the molecule-to-molecule variability (as measured by their standard deviation) of torsional measurements, in particular of the torsional stiffness, is about 10-20% in our current protocol, comparable with other single-molecule torque measurements [34, 48, 76]. This means that averaging over multiple (≥ 10) independent molecules is required to reduce the standard error of the mean sufficiently to be able to probe or detect small changes. In the current study, we have systematically varied salt concentration and applied force for a total of 28 conditions; carrying out ≥ 10 measurements for this number of different conditions would have been impractical in a "one-molecule-at-a-time" regime, highlighting the need for multiplexing.

3.3 Results and discussion

3.3.1 Principle of single-molecule torque measurements in magnetic torque tweezers

In magnetic tweezers, molecules of interest are tethered between a flow cell surface and ~μm-sized magnetic beads or particles (Figure 3.1A). External magnets are used to apply both forces and to control the rotation of the beads, therefore enabling the application of precisely calibrated stretching forces and control of the twist of the tethered molecules [41, 45, 178]. Magnetic torque tweezers enable the measurement of torque at the single-molecule level by employing a magnet configuration with a weak angular trap (Figure 3.1B-D; see also below) and a tracking protocol that permits to track the rotation of the molecule around the tether axis [33–35, 38]. The basic principle of the torque measurement is as follows: Tracking the rotation angle θ initially for a torsionally relaxed molecule, the mean of the bead's rotation angle θ_0 indicates the equilibrium position of the rotational trap and the magnitude of the fluctuations around the equilibrium position allows us to calibrate the stiffness of the angular trap (k_{ROT}):

$$k_{ROT} = k_B T / Var(\theta) = k_B T / (Std(\theta))^2 \tag{3.1}$$

where k_B is the Boltzmann constant and T the absolute temperature. After over- or under-winding the molecule by N turns, the restoring torque exerted by the molecular tether (τ_{mol}) gives rise to a shift in the mean angle position to a new angular position θ_N displaced from the initial equilibrium angle θ_0. The molecular torque can then be simply determined as the shift in mean angle multiplied by the rotational trap stiffness (Figure 3.1E):

$$\tau_{mol} = -k_{ROT} < \theta_N - \theta_0 > \tag{3.2}$$

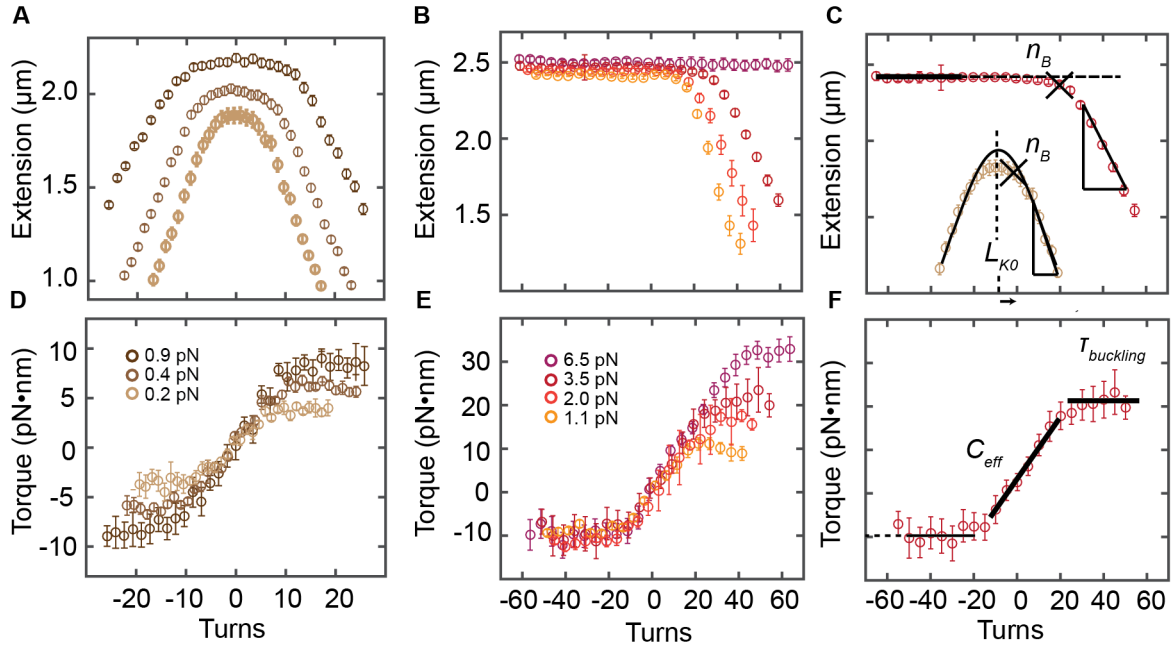

Figure 3.2: Averaged extension-rotation and torque-rotation measurements of dsDNA at varying forces. Measurements shown were recorded in TE buffer at pH 7.4 with 100 mM NaCl. (A, D) At low forces (< 1 pN; indicated in the legend in panel D) the extension vs. turn plot is symmetric about zero turns. When applying a number of turns to the DNA molecule (positive and negative), its extension stays constant, while the molecular torque increases linearly. Beyond the buckling point (post-buckling) the extension decreases linearly with each additional turn, while the molecular torque stays constant. (B, E) For higher forces (> 1 pN; indicated in the legend in panel E), no plectoneme formation occurs upon underwinding the molecules. Instead, torque induced melting takes place at −10 pN·nm. For forces > 6 pN, no supercoiling occurs at all. Instead a transition from B- to P-DNA occurs upon overwinding at 35 pN·nm. (C) Determination of the buckling points (n_B; black triangles), the post-buckling slopes (black lines) and Lk_0 (only for symmetric extension-rotation curves). (F) A line fit to the linear regime in the torque-rotation data (black line) is used to determine the torsional stiffness (C_{eff}). The mean of the constant plateau for positive turns (beyond buckling) is used to compute the buckling torque (τ_{buck}; black horizontal line).

3.3.2 Multiplexed magnetic torque tweezers

We have optimized our magnetic torque tweezers protocols to enable multiplexed measurements, i.e. to perform multiple single-molecule torque measurements in parallel. For parallel

measurements, it is desirable to employ molecular constructs that avoid the need for multi-component assembly, such as the addition of a rotor bead to the DNA or a fiducial marker bead or rod to the main magnetic bead, to maximize the number of well-tethered and complete molecular constructs in a single field of view. In our mMTT scheme (Figure 3.1A), we therefore use simple double-stranded DNA constructs, attached with one end to the flow cell surface via multiple digoxigenin labels and to commercially available magnetic beads via multiple biotin-streptavidin linkages (see Section 2.2.3 for the DNA construct), identical to constructs used routinely in conventional MT. We then exploit the particular geometry of bead fluctuations under a cylindrical magnet with a predominantly vertical field to track the beads' rotation angles via their X,Y-positions.

Tracking rotation angle from XY-position

If the magnetic field is aligned exactly vertically (the so-called freely-orbiting magnetic tweezers or FOMT configuration with a single cylindrical magnet [36]; Figure 3.1B), the bead is free to rotate about the tether axis and its thermal fluctuations trace out a doughnut shape (Figure 3.1B) in the X,Y-plane [36]. Importantly, this configuration allows tracking of the rotation angle by conversion of the X,Y-position on the doughnut to polar coordinates [36]. While the FOMT configuration enables observation of the unconstrained, rotational motion of the bead, it does not allow inducing twist. By adding a small magnet (or electromagnet [38]) the magnetic field is slightly tilted (Figure 3.1D). The tilted field provides a (weak) rotational trap for the magnetic beads and their fluctuations in the X,Y-plane no longer trace out the full circle, but an arc-like shape (Figure 3.1C). The beads still experience an upward pulling force in Z and the weak rotational trap enables to twist the molecule of interest by rotating the magnet assembly [34, 36]. Importantly, the position in X,Y can still be used to track the rotation angle of the bead. In practice, it is not necessary to align the magnets in FOMT configuration to fit the doughnut pattern; instead, it is sufficient to record the X,Y-position while rotating the magnets and to fit a circle to the recorded trace in order to determine the radius of the molecules movement around its tether axis, which is in turn used to transform the recorded X,Y-position of the bead to polar coordinates (see Supplementary Figures 3.5 and 3.6 and Chapter 2).

Optimization of the setup and trap stiffness for parallel torque measurements

There are conflicting requirements on the stiffness of the rotational trap in MTT, which in turn depends strongly on the magnetic field direction and strength. Equation 3.1 implies that for a given molecular torque, the shift in equilibrium angle is inversely proportional to the trap stiffness. As a consequence, if the trap stiffness is too high ($\geq$ 1000 pN·nm/rad, corresponding to Std(θ) < 4°), typical torques exerted by DNA lead to very small shifts in the equilibrium angle (< 1°) that are difficult or impossible to measure accurately [34]. In contrast, if the trap stiffness is too low ($\leq$ 30 pN·nm/rad or Std(θ) > 20°), the bead will not reliably follow the magnets' rotation, therefore precluding systematic and controlled application of twist to the tether (Supplementary Figure 3.7). For multiplexed measurements, we have to ensure that the trap stiffness is within these limits for the entire field of view (400 μm x 300 μm at 40x magnification and 260 μm x 190 μm at 60x magnification in our setup). In addition, it is desirable to have a homogeneous gradient of the field along the Z-direction to ensure that all tethers experience similar stretching forces. To guide and optimize the choice of magnet configuration

to satisfy these requirements, we carried out simulations of the axial and radial fields for our MTT magnet configuration. We calculated the magnetic field vectors for the magnet configurations used in FOMT (Figure 3.1B) and (m)MTT (Figure 3.1C) with the equivalent source method and exploiting the superposition principle (Supplementary Figure 3.8) [38, 42]. The cylindrical magnet with a hollow center used in FOMT is equivalent to two superimposed solid cylindrical magnets with opposite magnetization and the effect of the side magnet in the (m)MTT is added by considering an additional, laterally offset cylindrical magnet. We tested our field calculations against Hall probe field measurements and found excellent agreement between both (see Supplementary Figure S5, S6 and S7 of Reference [2]). Importantly, the gradient of the magnetic field, which essentially sets the force exerted on the beads, varies only by 0.5% over 400 μm (which corresponds to the largest extension of the field of view used in this work) for the mMTT configuration. The essentially constant field gradient implies that all tethered beads in the FOV experience the same force, only limited by the ~10% variation in total magnetization for the beads employed in this study [36, 42, 152].

Table 3.1: Buffer conditions and salt concentrations. Measurements were performed in TE-buffer at pH 7.4. Ionic strength was varied by the addition of $NaCl$ (salt 1, 2 and 3) or a combination of NaCl and $MgCl_2$ (salt 4).

	$Tris$	$EDTA$	$NaCl$	$MgCl_2$
Salt 1	10 mM	1 mM	20 mM	0
Salt 2	10 mM	1 mM	100 mM	0
Salt 3	10 mM	1 mM	500 mM	0
Salt 4	10 mM	1 mM	100 mM	10 mM

For the FOMT configuration, the radial field (i.e. X or Y) is zero directly under the cylindrical magnet, while adding the side magnet in the (m)MTT configuration adds a field component in X (Figure 3.1D). We found that for high-resolution torque measurement, in particular with the larger M270 beads, it is advantageous to lower the X-component of the field and, therefore, the trap stiffness. A displacement by ~400 μm reduces the trap stiffness ~3-4-fold, to 100-300 pN·nm/rad, compared to the alignment centered on the cylindrical magnet (Supplementary Figure 3.7). The rotational trap stiffness decreases with increasing distance of the magnet from the flow cell and, therefore, with decreasing force (Supplementary Figure 3.9). While the trap stiffnesses fall into the usable range of 30-1000 pN·nm/rad for all studied forces, we found it advantageous for low force torque measurements to bring the magnets closer to the flow cell (to 3-4 mm), corresponding to forces of 3-6 pN, for the segments of the torque measurement traces during which the magnets are actively rotated, to ensure that the beads reliably follow the magnets' rotation. For multiplexed torque measurements, it is important to not only have uniform forces across the field of view, but also uniform rotational trap stiffnesses. We found the variation in rotational trap stiffness for the same bead to only vary by $< 10\%$ at different positions across the field of view (Supplementary Figure 3.10). The variability across the field of view is much less than the $\geq 20\%$ bead-to-bead variability of the rotational trap stiffness at the same position in the flow cell (Supplementary Figure 3.10) that appears to stem from variations in the magnetic anisotropy of the beads employed [45, 50]. In practice, the variability in rotational trap stiffness is not a critical limitation, though, since the values tend to fall into the workable range of trap stiffnesses and since the same angle traces recorded for torque determination (Eq. 3.2) are also used for the trap stiffness calibration via Eq. 3.1. In practice,

after discarding beads that are attached via multiple DNA tethers, nicked molecules, or which are too close to other beads (which leads to tracking errors), we can simultaneously track currently up to 40 M270 beads or 80 MyOne DNA-tethered beads.

3.3.3 Probing the torque response of dsDNA using mMTT

Our mMTT setup enabled us to systematically investigate the response of dsDNA under different salt conditions. We recorded the extension and the rotation angle around the tether axis, which is converted to torque via Eq. 3.2, while systematically over- and underwinding DNA tethers (Figure 3.2). The extension vs. rotation behavior of dsDNA depends strongly on the stretching force exerted on the molecules. For low forces (< 1 pN) the extension-rotation curves for dsDNA are symmetric around zero turns (Figure 3.2A). Zero turns correspond to the torsional relaxed molecule. When the molecule is overwound (corresponding to positive turns and torques) or underwound (corresponding to negative turns and torques, respectively) at low forces (Figure 3.2A) its extension stays initially approximately constant. After a certain number of turns the buckling point n_B is reached and the extension of the molecule decreases linearly with each additional turn of the magnets beyond the buckling point. Simultaneously, starting at zero turns, the torque exerted by the molecule increases linearly with the number of turns up to the point where the buckling torque is reached and the molecule undergoes the buckling transition (Figure 3.2D). Beyond the buckling point, the torque remains approximately constant and additional turns create additional turns of the plectonemic supercoils. The extension vs. rotation curves become asymmetric for higher forces > 1 pN (Figure 3.2B) due to torque-induced melting that occurs at −10 pN·nm [34, 46, 90] (Figure 3.2E). Positive supercoiling occurs up to forces of ∼6 pN. For the highest measured force, 6.5 pN, no buckling occurs at all, instead the DNA molecules undergo a transition from B- to P- DNA at ∼35 pN·nm [1, 99, 100] (Figure 3.2E). The effective torsional stiffness of DNA can be determined from the experimentally measured torque vs. turns response, by fitting a slope to the linear region of the torque vs. turn response (Figure 3.2F):

$$C_{eff} = L_C/(2\pi N k_B T) \cdot \tau_{mol,N} = L_C/(2\pi k_B T) \cdot (\tau_{mol,N}/N) \tag{3.3}$$

Here L_C is the contour length of the molecule and N the applied number of turns, thus C_{eff} is in units of length and can be interpreted as a twist persistence length, in direct analogy to the bending persistence length A.

Extension-rotation and torque-rotation responses of dsDNA in different salt concentrations

We systematically recorded the extension and torque response of multiple DNA molecules and averaged the results for each force and salt condition (see materials and methods) including a total of 475 DNA molecules. For the measurements we chose a set of salt conditions (Table 3.1) that included monovalent salt concentrations from low (20 mM; “salt 1”) to high concentrations (500 mM; “salt 3”), including a point at near physiological monovalent salt concentration (100 mM; “salt 2”). In addition, we included measurements with 10 mM $MgCl_2$ added (“salt 4”); Mg^{2+} is the physiologically most abundant divalent ion and 10 mM Mg^{2+} is a typical “high” concentration, used e.g. to induce RNA folding in in vitro measurements [160]. We note

that these salt conditions cover the range typically used in in vitro studies of for e.g. RNA folding, nucleic acid-protein interactions, or nucleic acid nanotechnology. Averaged high-resolution extension-rotation and torque-rotation data from mMMT measurements resolve a salt dependence of dsDNA when applying turns (Figure 3.3). The response in extension (Figure 3.3A-C) and torque (Figure 3.3D-F) are similar for salt 1 and 2 and for salt 3 and 4. For further discussion we averaged the low salt conditions (salt 1 and 2, blue colors) and independently averaged the high salt conditions (salt 3 and 4, green colors). A large difference is observed between salt 1 and the higher salt conditions at 0.9 pN: While the extension-rotation curves are symmetric for the high salt conditions at this force, the response for salt 1 is asymmetric, indicating DNA melting upon underwinding. The lower salt concentration leads to a relative destabilization of the DNA double helix and thus to an earlier onset of DNA melting, consistent with previous reports [99, 105].

Buckling points

The buckling points correspond to the number of turns at which the DNA molecule starts to form plectonemes when being over- or underwound. Here we report the buckling points in units of the supercoiling density (Figure 3.3G), which is the change in linking number (i.e. the applied number of turns) normalized to the number of turns in the torsionally relaxed helix, 1 turn per 10.5 base pairs. The transition from an overwound (or underwound for forces smaller 1 pN) but straight molecule (pre-buckling) to a buckled molecule depends on the ionic surrounding. For high salt concentrations (with less electrostatic repulsion) buckling occurs for a (slightly) lower number of applied turns, compared to low salt conditions (with stronger ionic repulsion) [93, 94, 96]. The observed buckling points as a function of force are in reasonable agreement with a simple mechanical model of DNA due to Marko [91] (Figure 3.3G), as discussed below.

Post-buckling extension-rotation slopes

As negatively charged segments of DNA are brought into proximity in plectonemes, the radius (the size) of the plectonemes is strongly dependent on electrostatic interactions [93, 94]. For low salt conditions overall ionic screening is small, therefore electrostatic repulsion in the plectoneme is larger compared to the higher salt buffers, giving rise to a larger plectoneme radius and larger magnitude of the post-buckling slope at lower salt (Figure 3.3H), in agreement with previous measurements [76]. The force-dependence of the post-buckling slope follows an empirical power law behavior, in quantitative agreement with the results of Mosconi *et al.* [76] (Supplementary Figure 3.16A). In addition, the force and salt dependence of the slope in the plectonemic region are again reasonably well described by the mechanical model for DNA (Figure 3.3H), as discussed in the next sub-section.

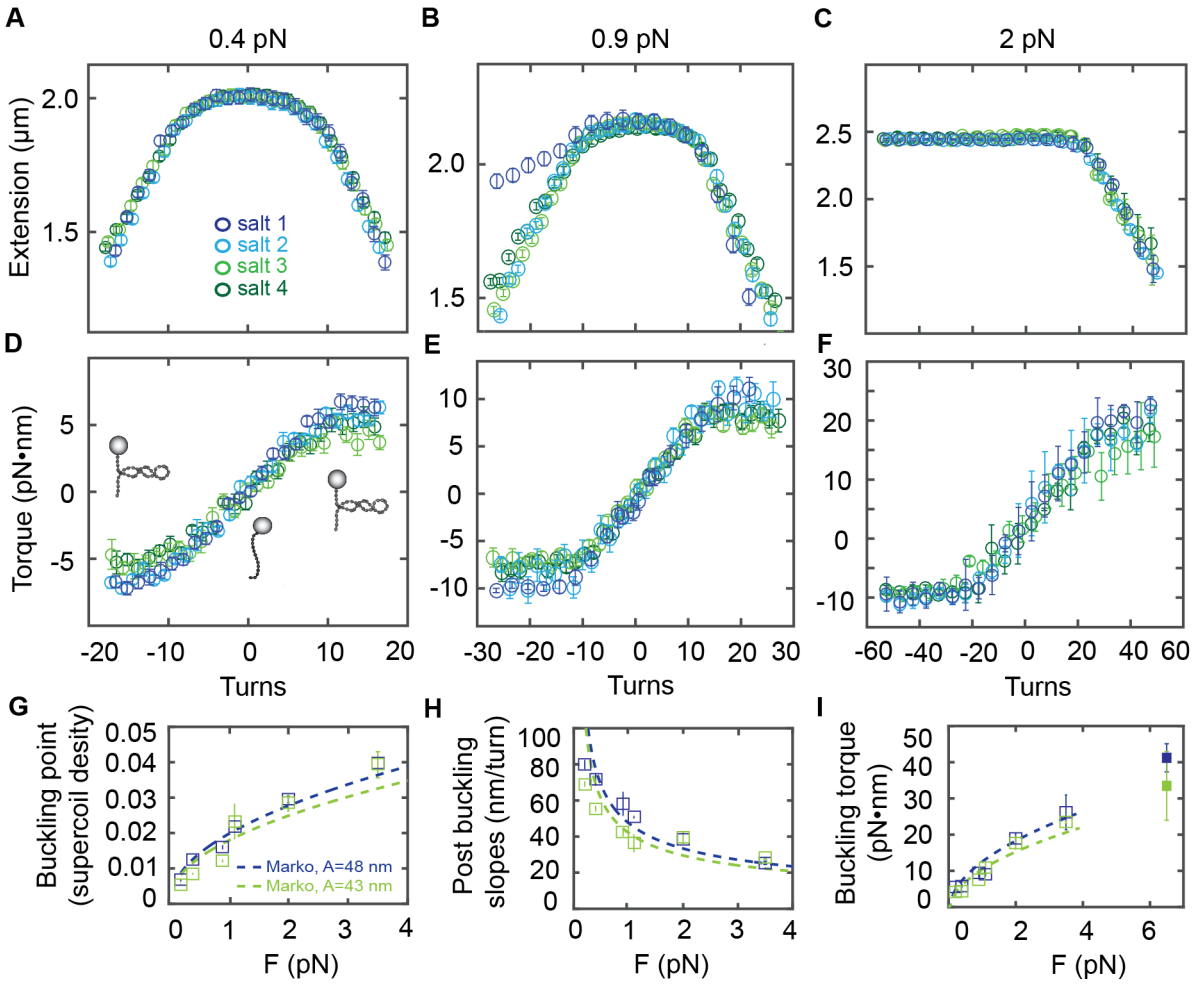

Figure 3.3: Averaged extension-rotation and torque-rotation responses of dsDNA for different salt conditions. Averaged extension vs. turns data for four different buffers and corresponding averaged torque vs. turns data at 0.4 pN (A,D), 0.9 pN (B,E) and 2 pN (C,F). Blue colors indicate measurements at low salt (salt 1 and 2); green colors indicate measurements at high salt (salt 3 and 4; see Table 3.1 for salt conditions). (G) (Normalized) buckling points as a function of force. We averaged salt 1 and 2 to low salt (blue) and salt 3 and 4 to high salt (green). (H) Post buckling slopes, determined from the averaged extension-rotation data against force. Same color code as in G. (I) Buckling torque derived from the torque vs. turn data. Color code as in G. Indicated with a filled, square symbol is the measured transition from B-DNA to P-DNA at 6.5 pN. Co-plotted in panels G-I is the Marko model (dashed lines) for dsDNA with fixed parameters: C (110 nm), A (43 nm for high salt conditions and 48 nm for low salt conditions), and $P_{lowsalt}$ = 20 nm or $P_{highsalt}$ = 15 nm.

Buckling torque

The measured molecular torque of dsDNA increases linearly up to the buckling transition for positive turns [93, 94]. We use the mean of the values in the plateau in the post-buckling regime to compute the buckling torque. Buckling torque increases with increasing force (see also Figure 3.2). The observed values are slightly lower for high salt compared to low salt (Figure 3.3I). Due to electrostatic repulsion at low ionic strength, dsDNA is able to store more molecular torque as compared to high salt before undergoing the buckling transition. We observe the force-dependence of the buckling torques to follow the empirical power law proposed by

Mosconi *et al.* [76] (Supplementary Figure 3.16B). The observed buckling torques are in good agreement with the mechanical model by Marko [91] (Figure 3.2I). To fit the buckling points, slopes in the plectonemic regime, and buckling torques in the framework of the Marko model, we used a fixed value for the intrinsic torsional stiffness C = 110 nm and the known values A = 48 nm and 43 nm for the bending persistence length at low and high salt, respectively. Our choice of C, notably taken to be independent of salt concentration, is a consensus value from previous studies [34, 46, 77] for the intrinsic torsional stiffness of DNA, corresponding to the high-force limit (see below). The values for the bending stiffness A under low and high salt conditions are typical average values for the corresponding salt conditions obtained in a number of different single-molecule studies [49, 55, 60, 61, 179] (see Supplementary Figure S1k of Reference [49] for an overview). The stiffness of the plectonemic state P at low salt and high salt was first fitted individually to the buckling points, slopes in the plectonemic regime, and the buckling torque data. We then averaged the resulting values for P and found P = 20 ± 4 nm and P = 15 ± 4 nm for low salt and high salt, respectively. We note that our value of 20 ± 4 nm at low salt is in agreement with the range of 21-27 nm suggested for these salt conditions; in addition, the observed decrease of P at high salt is as predicted by Marko [91]. In summary, our data on the behavior of DNA post-buckling is in agreement with previous results [76, 93, 94] and the effect of salt on DNA at the buckling point and in the post-buckling regime is at least semi-quantitatively described by the twistable worm-like chain model taking into account the known change in the bending persistence length and adjusting the torsional stiffness of the plectonemic state P. We find P to be 30% larger under our low salt conditions compared to high salt, which likely reflects the fact that in the plectonemes the DNA is sharply bent and segments of DNA are brought into close proximity.

The twist persistence length C_{eff}

Next, we focus on the pre-buckling regime, which does not involve large, plectonemic deformations of DNA and is dominated by the effective torsional stiffness of DNA. Using our mMTT data, we determined the effective torsional stiffness C_{eff} of DNA at varying forces and salt concentrations (Figure 3.4A), by fitting a slope to the torque vs. applied turns data in the pre-buckling regime (Equation 3.3 and Figure 3.2F). The fitting region was kept constant for each force and it was carefully selected to only fit to the linear regime, excluding data in the plectonemic and melting regimes. The effective torsional stiffness increases with force for all salt conditions from ~45 nm (at 0.2 pN) to ~100 nm (at 6.5 pN). The decrease in effective torsional stiffness with decreasing force is due to correlations between bending and twisting [77, 78] (see below) and has been seen in a number of previous studies [34–36, 48, 76].

Overall, the C_{eff} values appear similar for the different salt concentrations, irrespective of the valency of the ions used (Figure 3.4A). At the measured high forces (3.5 and 6.5 pN), the measured torsional stiffness values converge and at 6.5 pN C_{eff} is identical, within experimental errors, for all salt concentrations (Figure 3.4A,B). However, for lower forces (F < 3.5 pN) small but systematic differences between the different salt concentrations are apparent: The lower salt concentrations tend to give rise to higher C_{eff} values in the low force regime (Figure 3.4A,B). Running an n-way ANOVA on the C_{eff} values with salt and force as factors, we find that C_{eff} varies statistically significantly with force ($p = 1.3 \cdot 10^{-54}$) and salt ($p = 0.046$). For clarity, we again averaged the two low salt concentrations and the two high salt concentrations; the

resulting averaged values show the trend even more clearly (Figure 3.4C): An n-way ANOVA with salt and force as factors finds p = 0.0069 for the dependence on salt and p = $6.6 \cdot 10^{-57}$ for the dependence on force. We note that the same trends are observed when measuring individual molecules under the different conditions (see e.g. Supplementary Figure 3.12); however, given the measurement uncertainty of ~10-20% standard deviation, we focused on the averaged values for each conditions to draw statistical significant conclusions.

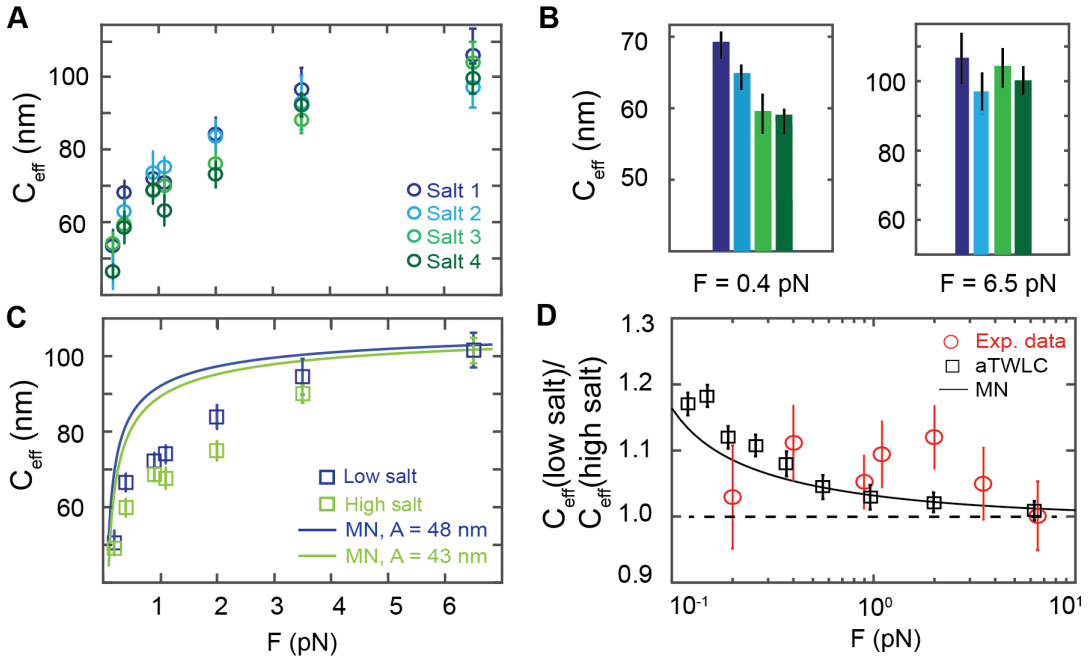

Figure 3.4: The effective twist persistence length of dsDNA for different salt conditions. The effective twist persistence length C_{eff} as a function of force and salt. Data points are the means and standard errors of the mean from 10–45 independent molecules for each salt and force condition. (A) C_{eff} increases strongly with force, saturating for high forces at ~100 nm for all salts. See Table 3.1 for salt conditions. (B) C_{eff} for all four salt conditions at 0.4 pN and 6.5 pN. Color code as in A. (C) low salt (salt 1 and 2, blue) versus high salt (salt 3 and 4, green) torsional stiffness data (see main text) show a trend to be slightly lower for higher salt concentrations. The MN model is co-plotted (solid line), with fixed values C = 110 nm and A = 48 nm (low salt, blue) and A = 43 nm (high salt, green). (D) The ratio of the low salt C_{eff} data and the high salt C_{eff} as a function of force. Two models, the MN model (black line) and the aTWLC model (black squares) are co-plotted with the experimental data (red circles).

The effective torsional stiffness is independent of salt concentration at high forces (F > 6 pN), but systematically and statistically significantly lower for high salt (F < 6 pN) in particular in the intermediate force regime (0.9 to 2.0 pN) (Figure 3.4C). The fact that the effective torsional stiffness deviates from the "true" intrinsic torsional stiffness value and decreases with decreasing force has been investigated before and can be (at least qualitatively) understood by taking into account the coupling between bending and twisting fluctuations, in particular using the perturbative model by Moroz and Nelson (MN). Taking to account the known dependence of the bending persistence length on salt (and assuming a salt-independent value for the intrinsic torsional stiffness), the MN model predicts relative differences between the high and low salt conditions that are in good agreement, within experimental errors, with our measurements

(Figure 3.4D, solid black line; reduced χ^2= 1.0). In contrast, the data are less consistent with the ratio of C_{eff} at low vs. high salt being equal to one (Figure 3.4D, dashed horizontal line; reduced χ^2= 1.92). Unfortunately, the MN model does not quantitatively account for the force dependence of C_{eff} and overestimates C_{eff} at intermediate and low forces (0.2 to 2 pN) (Figure 3.4C). This shortcoming of MN theory has been described and investigated in a number of recent publications. Extensions of the MN model have been proposed, to account for the systematic deviations between the MN model and experimental data [80]. One particular extension of MN is to extend the underlying isotropic rod model to include an anisotropy, i.e. distinguish between bending deformations between the two orthogonal directions that are perpendicular to the helix axis. First introduced by Marko and Siggia [180], this anisotropic rod model (aTWLC) has recently been investigated by Nomidis *et al.* [3] by extensive coarse-grained computer simulations; the results suggests that introducing a non-zero twist-bend coupling constant (which is zero by definition in the isotropic rod model) can quantitatively account for the previously published C_{eff} vs. F data. Unfortunately, our current implementation of the coarse-grained model does not explicitly account for electrostatics. However, again taking into account only the changes in bending persistence length with salt and keeping the intrinsic torsional stiffness fixed, the aTWLC model predicts differences of the high and low salt values for C_{eff} very similar to the MN model and consistent with experimental data (Figure 3.4D, black squares; reduced χ^2= 1.15).

3.4 Conclusion

We have developed and optimized a multiplexed magnetic torque tweezers setup that enables parallel measurements of torque at the single-molecule level. Our mMTT approach is based on exploiting the particular tethering geometry of DNA-tethered magnetic beads under a cylindrical magnet with a small side magnet, which allows us to track rotation angle from the beads' motion in X,Y. Using the mMTT implementation, we have obtained averaged extension-rotation and torque-rotation curves for DNA at varying salts and forces to, in particular, probe the effect of ionic conditions on the torsional stiffness of DNA. While we find the effective torsional stiffness to be ~5-10% smaller for higher salt concentrations for forces < 3 pN, C_{eff} converges at high forces and there are no significant differences between salt conditions at 6.5 pN. The differences in the effective torsional stiffness at lower forces can be rationalized by mechanical models that only take into account the known change in the bending persistence length with salt and that assume a constant value for the intrinsic torsional stiffness of DNA. In summary, our results strongly suggest that while many properties of DNA under torsional strain, in particular of plectonemes, are salt-dependent, the intrinsic, high-force torsional stiffness for DNA is independent of ionic strength. Our results provide fundamental input for models and simulations of DNA under torsional constraint and will be valuable for understanding DNA in more complex biological contexts. Our multiplexed torque protocol opens up the possibility to probe small changes in nucleic acid mechanics, through averaging, which would be difficult to detect in "one-molecule-at-a-time" measurements. Here, we have focused on the salt-dependence, but our method would be equally applicable to study e.g. anisotropic effects in bending and twisting or the temperature dependence of elastic properties. Going beyond bare DNA, multiplexed torque measurements will also be applicable to other molecules (e.g. double-stranded RNA [49]) and enable us to probe DNA-drug and DNA-protein interactions.

3.5 Supplementary data

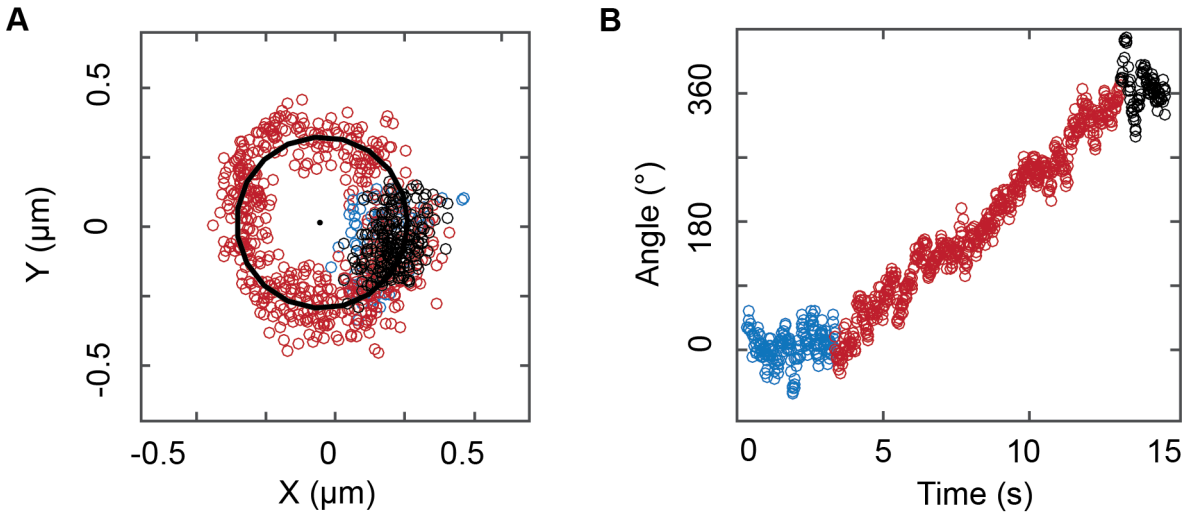

Figure 3.5: Tracking of the bead's X,Y and angular position while rotating the magnets by one turn. (A) The bead's motion in the X,Y-plane before, after, and while rotating the magnets by one turn. The position of the bead before and after twisting the bead for one turn is shown in blue and black, respectively. The bead's position while turning the magnet -and thus the bead- is shown in red. A circle is fitted to the recorded data in order to determine the radius of the bead's motion and transform X,Y-positions to polar coordinates. (B) The trace of the rotation angle of the bead, obtained by coordinate transformation of the data in panel A. Same color code as in A. The measurement was performed with a MyOne bead at F = 0.9 pN in PBS buffer.

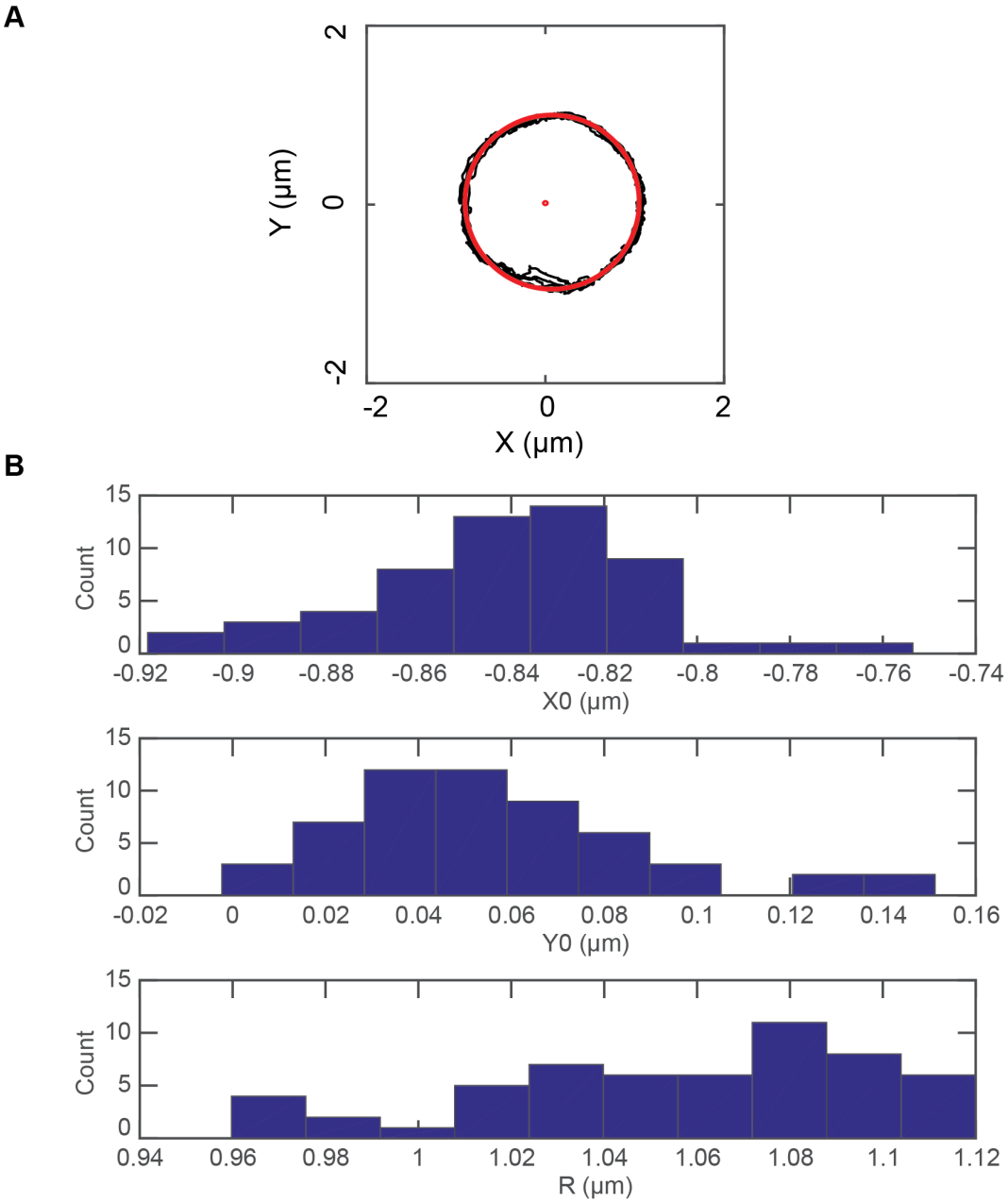

Figure 3.6: Analysis of the X,Y-fluctuation and tether geometry during magnetic rotation in systematic torque measurements. To measure the torque and extension response of DNA tethers, we systematically over- and underwind them by applying integer number of turns with the magnets (typically 2 or 5 turns, depending on stretching force). The traces of X,Y-positions while rotating the magnets can be used to determine the attachment geometry of the DNA-bead system, defined by the center position (X0,Y0) and the radius of the circle R of the X,Y-fluctuation pattern, which are required to convert the observed X,Y-fluctuations to polar coordinates. It is, therefore, not necessary to first align the FOMT configuration (Figure 3.1B) prior to carrying out torque measurements. (A) Tracked X,Y-positions of a magnetic bead (M270) recorded while turning the magnets (in total five turns) in the mMTT (black). The circle fit is shown in red. The data and the fit were shifted for illustration such that the circle is symmetric around zero by subtracting the fitted (X0,Y0). (B) Histograms (all in μm) of fitted radii R and center positions (X0,Y0) obtained for one tethered molecule during a complete over- and underwinding cycle at one force consisting of 55 individual magnet rotation traces similar to the one shown in panel A. The fitted values for R and (X0,Y0) vary only by ~10 nm from trace to trace, which corresponds to an uncertainty of ~1% in the radius. We use the median of R, X0 and Y0, in further analysis of the data set, in particular to transform the recorded X,Y-positions to polar coordinates. For this data set, the median values are 1.1151 μm, −0.8697 μm and 0.0466 μm, for R, X0 and Y0, respectively.

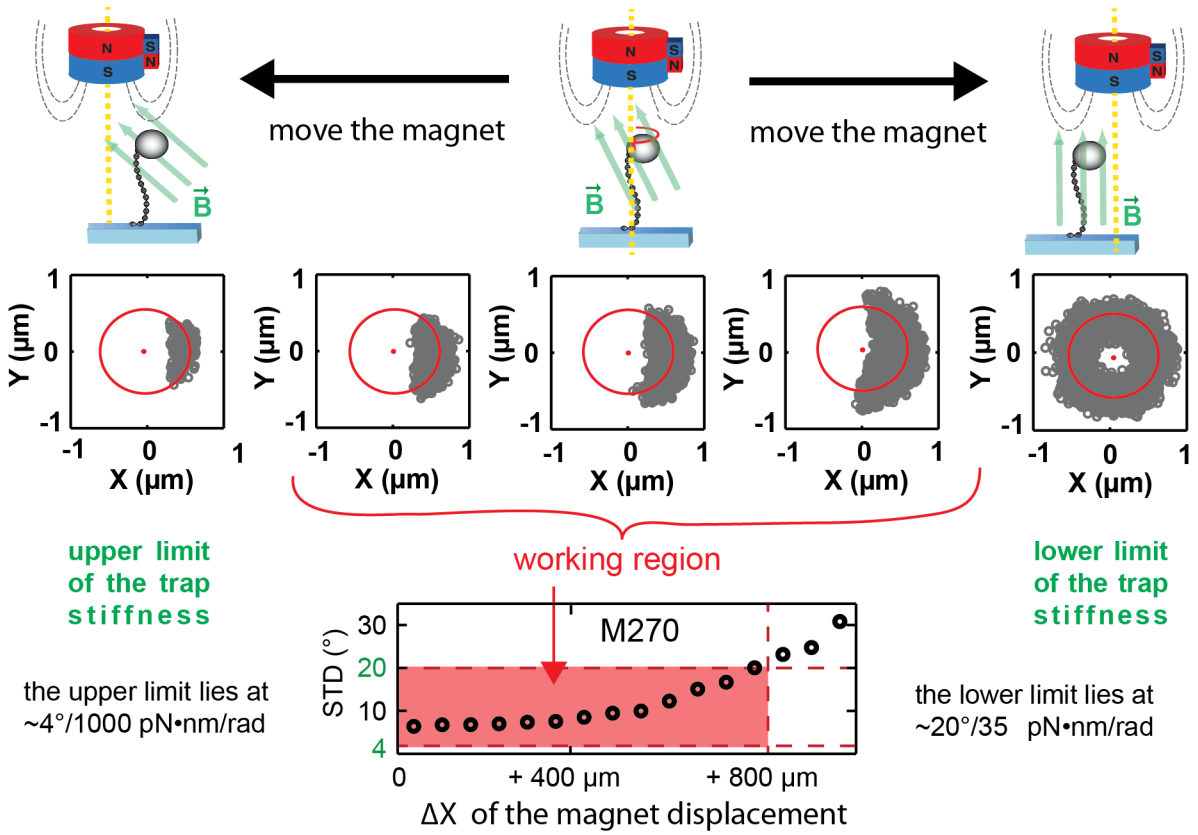

Figure 3.7: Dependence of the torsional trap stiffness on magnet alignment. The stiffness of the angular trap depends strongly on the relative position of the bead to the magnet assembly. Top row: schematic of the magnet position relative to the DNA-tethered magnetic bead indicating how the displacement of the magnets affects the magnetic field at the position of the bead. Middle row: the bead's motion in the X,Y-plane for the relative bead-magnet alignment indicated above. Changes in the magnetic field direction when changing the magnet position lead to changes in the X,Y-fluctuations of the magnetic bead. Shifting the position of the magnet towards the direction of the side magnet leads to a shift of the magnetic field lines towards the vertical alignment. This in turn increases the extend of rotational fluctuations of the bead (corresponding to softer rotational trap stiffness). If the magnet assembly is shifted sufficiently far in the direction of the side magnet, the magnetic field at the bead's position becomes vertical and the trap stiffness is reduced to the point that thermal fluctuation are sufficient to trace at a full turn (rightmost column): the bead's motion in the X,Y-plane traces out a doughnut-like shape, as in the FOMT configuration. If the magnet is shifted in the opposite direction, the magnetic field lines are tilted towards the horizontal axis, such that the stiffness of the angular trap increases and the bead's motion is increasingly constrained. Traces of bead fluctuation at different positions of the magnet were analyzed and the data converted to angular trap stiffness via Eq. 3.1. Zero indicates the position where the magnetic field of the cylindrical magnet without side magnet is vertical, indicated by the fact that the bead's fluctuations trace a full circle in the X,Y-plane. When adding the small side magnet to the cylindrical magnet, the bead experiences a trap stiffness of ~200 pN·nm/rad (8°). It was previously shown that trap stiffnesses above ~1000 pN·nm/rad make it difficult to perform accurate measurements of typical molecular torques [34]. To determine a lower limit for practical trap stiffnesses, we rotated the magnet assembly by one turn at each position and checked whether the bead follows the magnet rotation or not. The red box indicates the area in which the bead did follow the magnet rotation, beyond the red dashed line this was not the case. Below values of ~35 pN·nm/rad (or above standard deviation values of 20°), the stiffness of the trap is too soft to ensure bead rotations. The data shown are for a M270 bead measured at F = 2 pN in PBS buffer.

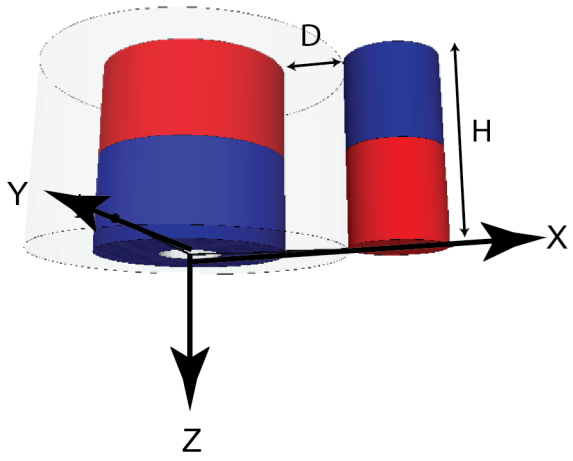

Figure 3.8: Schemetic of the magnet configuration in MTT and the principle of the 3D-field calculations. Between the cylindrical main magnet and the side magnet is a spacing of distance D. The center of the cylindrical magnet is chosen as center of the coordinate system. Z is pointing toward the flow cell and X is pointing towards the side magnet. The magnetic field is calculated using a semi-analytical description. The magnetic field is computed using the equivalent source method, essentially as described by Janssen *et al.* [38].

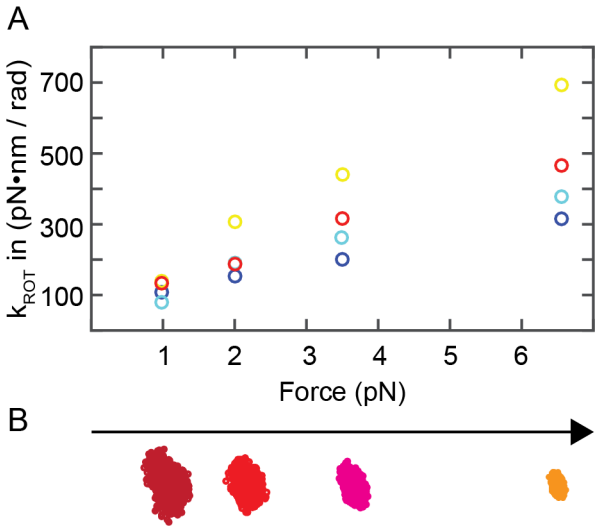

Figure 3.9: The stiffness of the rotational trap increases with increasing force. (A) Measured trap stiffness for four M270 beads (different colors correspond to different beads) as a function of the applied stretching force. In order to change the force, the magnets are moved in Z-direction. The magnetic field and its gradient changes with the height of the magnets and thus both the force and trap stiffness changes with magnet height [34, 38]. The closer the magnets, the higher the force and the stronger the angular trap. For this magnet alignment, the trap stiffness for four different beads at 6.5 pN varies from 300 to 700 pN·nm/rad, which still lies within the workable range to perform torque measurements. The spread of the measured rotational trap stiffnesses at a given magnet height (or force), is likely due to bead-to-bead variations of their magnetic anisotropy [45] (see also Supplementary Figure 3.10). (B) Bead fluctuations in the X,Y-plane for one particular bead held at the stretching forces indicated by the axis on top.

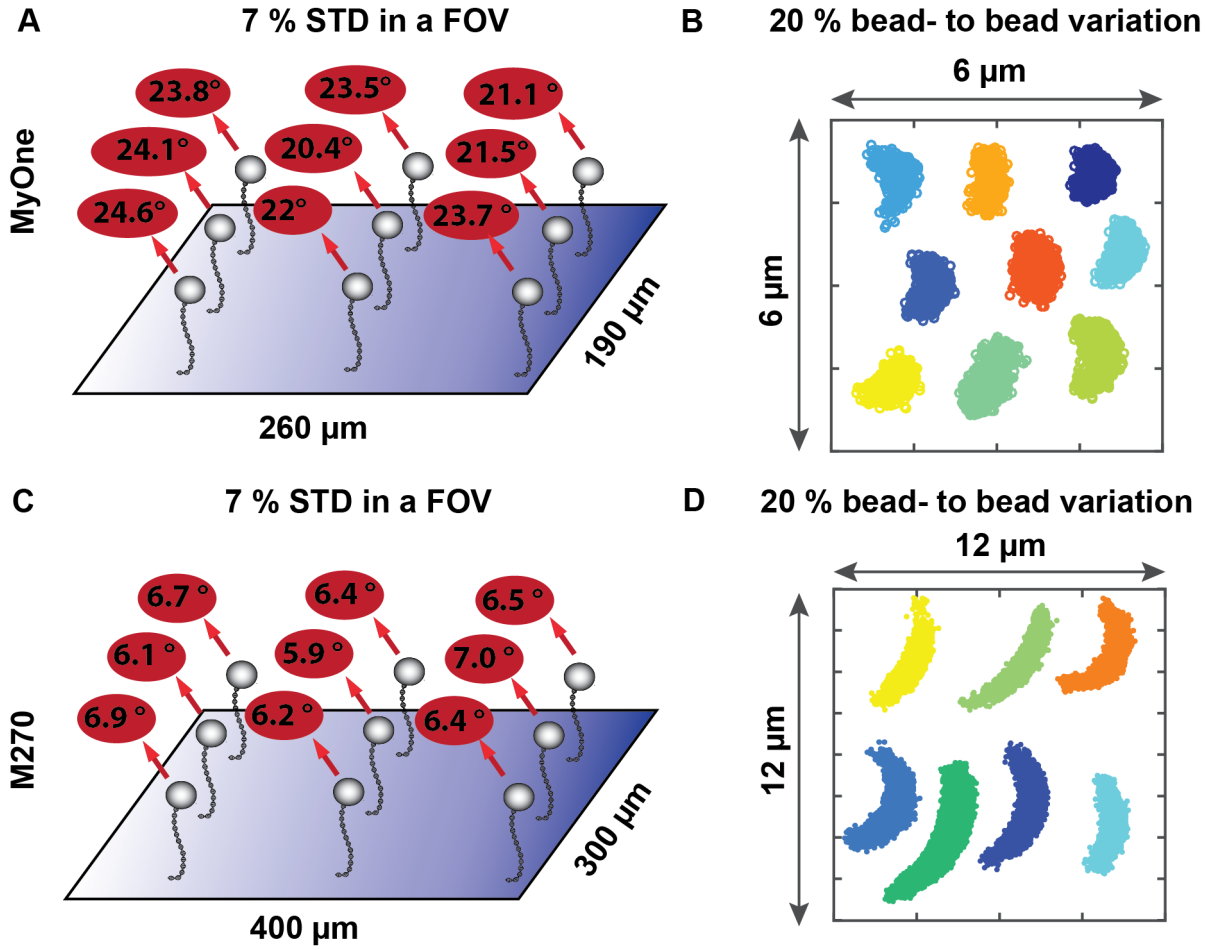

Figure 3.10: Bead-to-bead variation and variation across the field of view of the rotational trap stiffness. Measurements for MyOne (A,B) and M270 (C,D) beads at a magnet height of 4 mm above the flow cell surface. (A, C) The position of one particular bead was varied across the FOV by moving the flow cell with respect to the camera and magnet assembly and at each position the standard deviation of the angular fluctuations was measured. The positions in the FOV are shown schematically and the corresponding standard deviations are annotated. The variation of the standard deviations of the angular fluctuations of a bead across the FOV is ~7%. (B, D) In order to determine the bead-to-bead variation of the rotational trap stiffness we measured several beads in the same position under the magnets, within a fixed region of interest (6 x 6 μm for MyOne and 12 x 12 μm for M270 beads). This ensures that the relative position of the magnets to the bead center was only allowed to vary by a few μm. The different colors represent fluctuations of different beads and are placed in the area for illustration. Bead fluctuations within this figure are shown 6x larger than in reality. The bead-to-bead variation was found to be about 20% (measurements were performed for ten beads in PBS buffer).

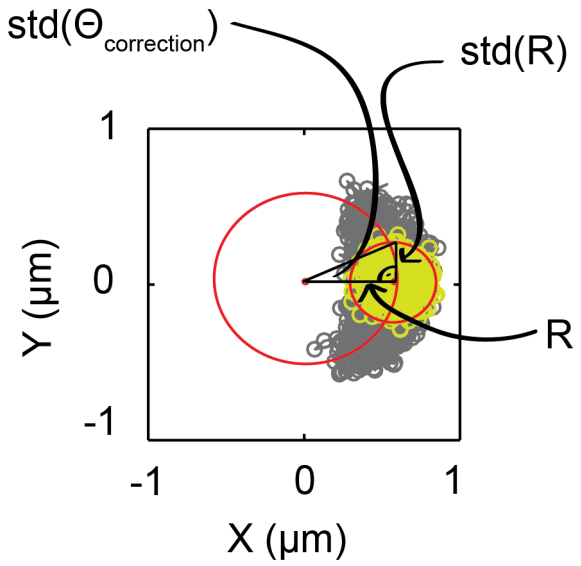

Figure 3.11: Cross-talk correction of the angular fluctuations. Due to thermal noise the bead fluctuates in the X,Y-plane (shown in yellow) even in the absence of rotational fluctuations. The magnitude of these transverse fluctuations in the magnetic tweezers is given by the classic "inverted pendulum" argument and is determined by the applied force and tether length. In the MTT/FOMT configuration the radial fluctuations are representative of the transversal fluctuations and can be used to calibrate the stretching force [36]. However, since the transverse fluctuations occur both in X and Y, they give rise to apparent fluctuations in the angle, even in the absence of bead rotation. To correct for this cross-talk, we compute the magnitude of the angle fluctuations due to the "standard magnetic tweezers" transverse fluctuations from the standard deviation of the radial fluctuations (std(R)) and the fitted radius (R):

$\mathrm{Var}(\theta_{correction}) = (\arctan(\mathrm{std(R)/R}))^2$

When calculating the stiffness of the angular trap (Eq. 3.1), we employ the corrected variance of the angle fluctuations:

$\mathrm{Var}(\theta) = \mathrm{Var}(\theta_{measured}) - \mathrm{Var}(\theta_{correction})$

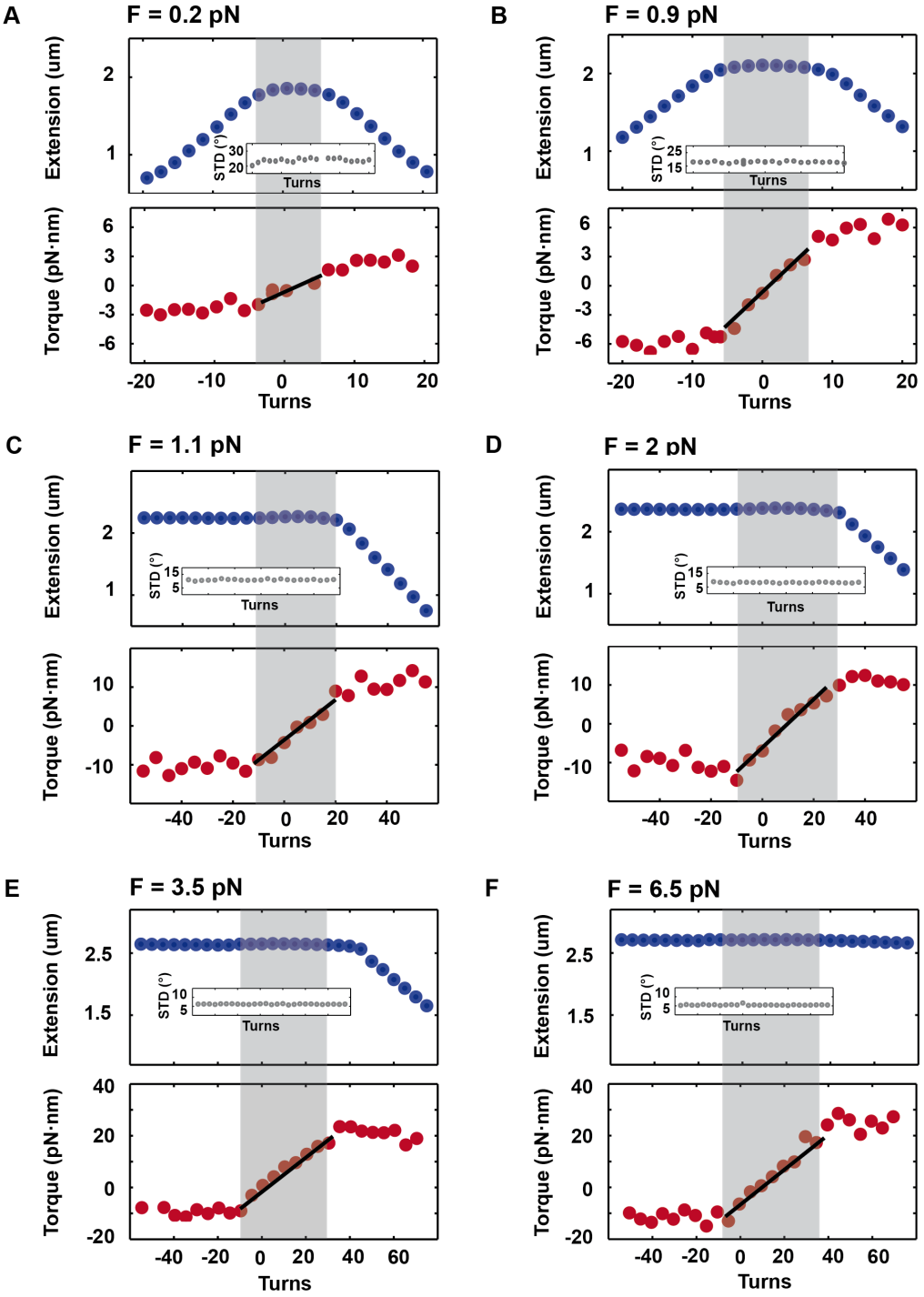

Figure 3.12: Representative torque measurements of dsDNA for a single molecule at different forces. Panels A to F show torque measurements of dsDNA at 100 mM NaCl (in TE buffer, pH 7.4) at varying forces for one particular molecule. The insets show the standard deviation (which is related to k_{ROT} by Eq. 3.1) recorded for each measurement point.

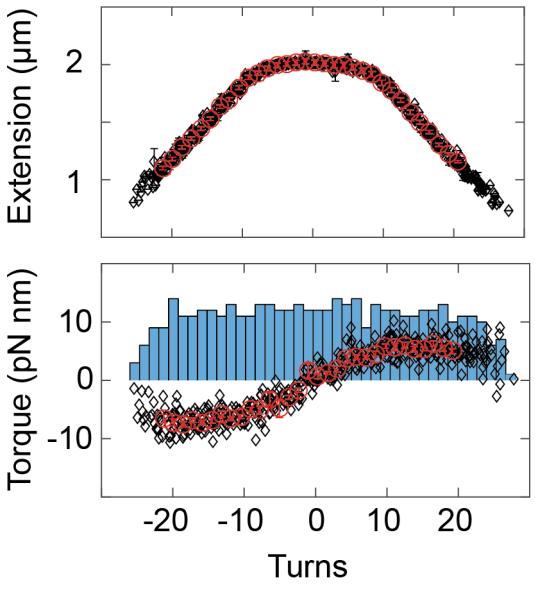

Figure 3.13: Multiple bead measurements: Averaging algorithm for symmetric extension-rotation curves. Data shown were recorded at 0.4 pN (using MyOne beads) and in TE buffer supplemented with 100 mM NaCl. The extension-rotation data of each molecule were first analyzed individually by fitting a Gaussian to determine Lk0 of the molecule. The extension as well as the torque data were shifted by –Lk0 on the turn axis in order to be symmetric around zero turns. The extension of the molecule was adjusted by correcting each individual extension according to the deviation to a defined reference curve. Corrected data for multiple molecules for the extension vs. turns and for torque vs. turns are shown as black diamonds. Next, the data were binned. The blue bars in the background of the torque-rotation data indicate the number of points in each bin. Values within each bin were averaged to yield the final averaged extension vs. turns and torque vs. turns data (red circles).

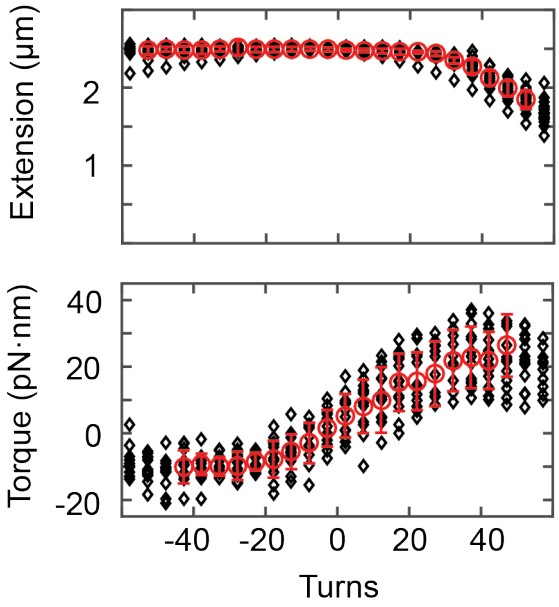

Figure 3.14: Multiple bead measurements: Averaging algorithm for asymmetric extension-rotation curves. Data shown within this figure were recorded at 3.5 pN (M270 beads) and in TE-buffer supplemented with 100 mM NaCl. The extension-rotation data of each molecule were first analyzed individually. In order to overlay the curves along the turns axis, the buckling point of each curve was determined by fitting a horizontal line to the extension-rotation data in the range where the extension is approximately constant. The first experimental value of the extension data (within error) at positive turns that falls below this line is defined as the buckling point (Figure 3.2C). Each curve is then shifted to the mean value of all collected buckling points at that particular force. The extension of the molecule was adjusted by correcting each individual extension according to the deviation to a defined reference curve. Torque values were shifted to −10 pN·nm for −20 turns (or smaller), assuming that torque-induced melting occurs for these values. All extension or torque values at the same number of turns are averaged, to obtain final averaged extension vs. applied turns and torque vs. applied turns curves.

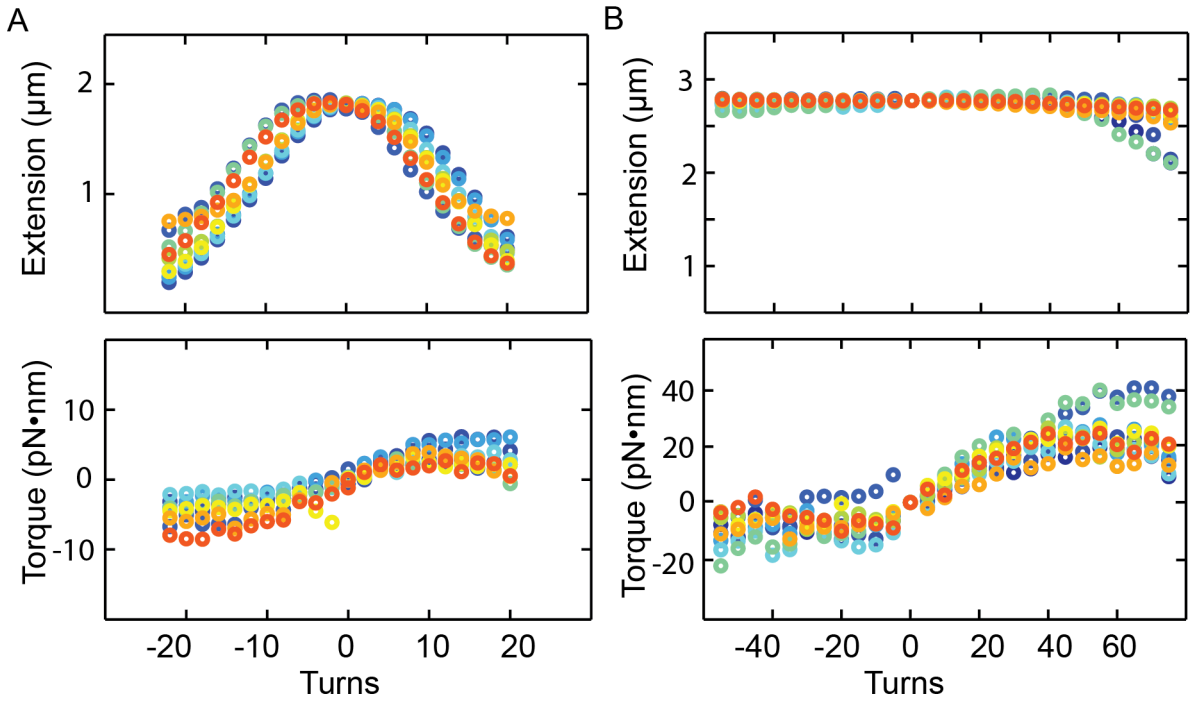

Figure 3.15: Multiplexed extension and torque measurements. Each color corresponds to one particular molecule, all measured at the same time in one mMTT measurement run. No averaging or shifting is performed for these data sets. Shown here, are eight tethers using MyOne beads at 0.4 pN (panel A) and nine DNA tethers using M270 beads at 6.5 pN (panel B), each measured simultaneously. Measurements were performed in TE-buffer with 100 mM NaCl and at pH 7.4.

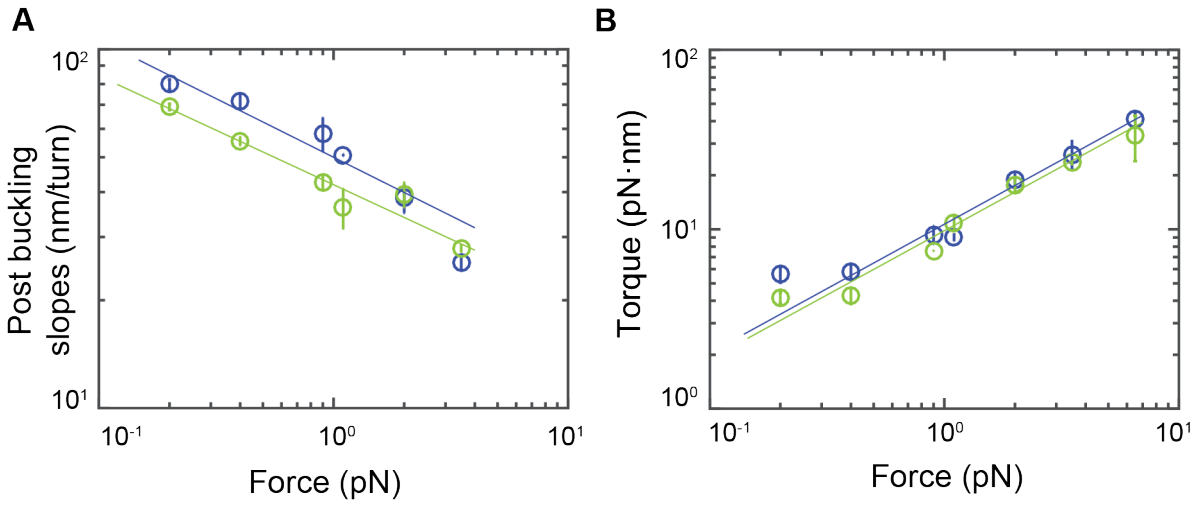

Figure 3.16: Double-logarithmic plots of the measured post buckling slopes vs. force (A) and buckling torques vs. force (B) for low salt (blue) and high salt (green) data. These are the same data as Figure 3.3H and I. We find a power law dependence for the post buckling slopes with an exponent of −0.33 (95% confidence intervals: −0.19 to −0.46) at low salt and −0.30 (95% confidence intervals: −0.21 to −0.49) at high salt (solid lines in A). Similarly, for the buckling torques, we find exponents of 0.72 (95% confidence intervals: 0.48 to 0.95) at low salt and 0.71 (95% confidence intervals: 0.52 to 0.91) at high salt (solid line in B). The fitted exponents are in quantitative agreement with Mosconi *et al.* [76]. Additionally, we see similar trends for the salt dependence. The exponential fit was performed between 0.2 and 3.5 pN.

Chapter 4

Twist-Bend Coupling and the Torsional Response of Double-Stranded DNA *

Abstract

In this Chapter we discuss the twistable-worm like chain, which is until today the accepted model to describe mechanical properties of nucleic acids. Using this model and taking DNA as a symmetric, isotropic elastic rod, Moroz and Nelson introduced in 1997 an analytical formula that rationalizes the dependence of the effective torsional stiffness of DNA on the stretching force. However, recent magnetic tweezers experiments have reported systematic deviations of the twist response of double-stranded DNA from the predictions of this model. Here we show, by means of analytical results and computer simulations, that these discrepancies can be resolved if a coupling between twist and bend is introduced. This coupling, which is a correction to the oversimplified TWLC model, occurs due to the asymmetry of the helix, i.e. the major and minor grooves. We obtain an estimate of 40±10 nm for the twist-bend coupling constant. The simulations are in good agreement with high-resolution, magnetic-tweezers torque data. Although the existence of twist-bend coupling was predicted long ago [181], its effects on the mechanical properties of DNA have been so far largely unexplored. We expect that this coupling plays an important role in several aspects of DNA statics and dynamics.

4.1 Introduction

The mechanical properties of double-stranded DNA (dsDNA) are critical for both its structure and function within the cell. The stretching of dsDNA under applied forces has been measured by single-molecule techniques [142, 182] and is accurately reproduced by a simple polymer model, containing the bending stiffness as the only parameter [55]. Elastic polymer models were also successfully employed to study the torsional properties of dsDNA [41] and compared to single-molecule experiments, such as magnetic tweezers (MT) [41]. The currently accepted

*This chapter is adapted from Nomidis *et al.* [3] with permission from the American Physical Society. Copyright ©2017 American Physical Society.

elastic model for dsDNA is the twistable worm-like chain (TWLC) [159]. Although the TWLC correctly describes the overall response of dsDNA to applied forces and torques, it fails to quantitatively explain the force dependence of the effective torsional stiffness [34, 36]. Here, we show that an alternative elastic model proposed by Marko and Siggia (referred to as aTWLC model) [180] quantitatively describes the force dependence of the effective torsional stiffness, by taking into account a direct coupling between twist and bend deformations. Furthermore, we demonstrate that the model proposed by Marko and Siggia explains an unresolved discrepancy in the measured intrinsic torsional stiffness, obtained from different techniques. Finally, we show that this model provides a better description of the pre-buckling torque response of dsDNA, determined in high-resolution magnetic torque tweezers (MTT) experiments, than the TWLC.

4.2 Materials and methods

This work combines torsional stiffness, extension-rotation and torque-rotation data measured with multiplexed magnetic torque tweezers as explained in Chapter 3 and coarse-grained computer simulations of dsDNA. For comparison, we add experimental FOMT data of the effective torsional stiffness of DNA from Reference [36] to this study.

4.2.1 Coarse-grained computer simulations

Nomidis performed coarse-grained computer simulations of dsDNA of the TWLC model and the aTWLC model to study the response of dsDNA to induced twist. Computer simulations were performed using a coarse-grained bead-and-spring model, similar to that discussed in Reference [183]. Each bead is represented as a rigid, spherical body, and described by an orthonormal frame. In our discretization setup we choose beads with diameter of 2.3 nm, corresponding to 6.7 base pairs, which is a good compromise between numerical accuracy and computational efficiency. The overall length of the DNA molecule is thereby 1000 base pairs (i.e. 1 kbp). The two ends of the polymer were attached to an impenetrable surface and a large bead, similarly to a typical MT experiment. More details are given in Reference [3].

4.2.2 Magnetic torque tweezers measurements

Using multiplexed MT we measured extension-rotation and torque-rotation curves in TE buffer (10 mM Tris and 1 mM EDTA at pH 7.4) supplemented with 100 mM NaCl. The magnetic tweezers setup, flow cell preparation and bead selection is described in Chapter 2. Measurements and corresponding data averaging were performed similarly to Chapter 3, leading to averaged extension-rotation and torque-rotation curves. The effective torsional stiffness data is extracted from the averaged curves by fitting a line to the linear regime, i.e. the pre-buckling regime, in the torque-rotation data. Measurement and analysis details are given Chapter 3.

4.3 Results and discussion

4.3.1 The symmetric, isotropic elastic rod model

Nucleic acids under at least not too large forces and torques and much longer than their persistence length, are well described by the isotropic elastic rod model (as introduced in Chapter 1.3.1). This model takes on two assumptions: First, the helix is symmetric, i.e. in absence of major and minor grooves. Second, bending along the molecule is isotropic, leading to a single parameter to describe the bending stiffness ("perfect helical symmetry"). Here, DNA is described as a beam or a rod that can undergo three deformations, namely extension, bending and torsion. Each described by an elastic constant, which describes the properties of the "material" and a corresponding quantity that describes the change induced through the deformation. Bending deformations are described by the bending stiffness A, stretching is described by the Young's modulus B, and twist deformations by the torsional stiffness C. The only allowed coupling term is the twist-stretch coupling D. Sometimes the stretch stiffness S is used instead of B ($S = B \cdot k_BT$).

In order to calculate the energy stored in the beam by such a deformation, the beam is divided in small segments ds. The overall energy is then calculated by adding up all contributions from the segments by mathematical integration [184]. In the case of small deformations, the energetics are simply quadratic [184], according to the potential of a harmonic spring for small deformations:

$$E = \frac{1}{2} k_BT \cdot \int_0^{Lc} \left[A\beta^2 + Bu^2 + C\omega^2 + 2Du\omega \right] ds \tag{4.1}$$

Eq. 4.1 describes the energy E of the elastic rod along the macromolecular chain by integration along the contour length L_C over small segments ds, with s being the arc-length of the molecule. $\beta(s)$ is a vector that measures how the tangent vector changes as one walks down its length, $u(s)$ and $\omega(s)$ are scalars describing the fractional change in length of the segment, and measuring how each element has been rotated perpendicular to the rod's main axis relative to its neighbor according to Reference [54], respectively. Aβ^2, Bu^2, $C\omega^2$ and $Du\omega$ times k_BT are in units of force, i.e. Newton. k_BT is taken out of the integral for convention, thus A and C are in units of *length*, B in $length^{-1}$ and D is *dimensionless*. The twist-stretch coupling is the only allowed cross term in this model as the energy itself is a scalar.

Note, that the convention throughout this Chapter is adapted from Nelson [54]. Other definitions, in particular of $\beta(s)$, $u(s)$ and $\omega(s)$, might be found in literature, in general explaining the same or similar models.

The inextensible WLC

Stretching of DNA under applied forces (< 10 pN) is well described by the inextensible worm-like chain (WLC) taking the bending stiffness as the only fitting parameter. The force-extension behavior of dsDNA can be studied using MT by simply pulling on the molecule, early experiments were performed by Smith *et al.* [142]. No twisting, thus no C, and no stretch modulus B, is needed to describe the energetic deformation, see Eq. 4.2. One can derive an analytical

formula that accurately describes the force-extension behavior of nucleic acids, based on the typically termed worm-like chain (WLC).

$$E = \frac{1}{2} k_B T \cdot \int_0^{Lc} \left[A\beta^2 \right] ds \tag{4.2}$$

The extensible WLC

The extensible WLC is used to describe the stretching behavior of DNA including higher forces (> 10 pN). The energy of an isotropic elastic rod is hereby described by bending and stretching, whereas there is still no twist (see Eq. 4.3). From force-extension experiments it was found that DNA overcomes a stretching transition at about 65 pN that induces a conformational transformation from B-DNA to a stretched form, termed S-DNA (for more information see Chapter 1.3.1).

$$E = \frac{1}{2} k_B T \cdot \int_0^{Lc} \left[A\beta^2 + Bu^2 \right] ds \tag{4.3}$$

The twistable worm-like chain and the model of Moroz and Nelson

The twistable worm-like chain (TWLC), which treats DNA with perfect helical symmetry, is the currently accepted model to describe twist deformations in DNA. It takes the bending persistence length as well as the torsional persistence length into account. The stretch modulus and thus the twist-stretch coupling can be neglected for the forces relevant in this model (F < 10 pN), hence, DNA is practically inextensible. The free energy of deformation reduces to:

$$E = \frac{1}{2} k_B T \cdot \int_0^{Lc} \left[A\beta^2 + C\omega^2 \right] ds \tag{4.4}$$

Moroz and Nelson [78] solved this problem analytically in 1997 and compared it to experimental available data on single-molecule studies on DNA under applied force and torque. The model is in good agreement with DNA extension-rotation data [78]. However, it has not been compared to direct measurements of molecular torque, i.e. torque-rotation measurements of dsDNA.

The twist persistence length (also in units of length), termed also the intrinsic torsional stiffness, describes the overall energetic cost of a pure twist deformation. Without any thermal fluctuations, DNA can be seen as a stiff rod, and all twist is absorbed in C. However, with thermal fluctuations, some twist can be absorbed in bending, leading to an effective torsional stiffness C_{eff} that is smaller than C. This is in particular of relevance when discussing several measurement modalities that often imply stretching forces. Moroz and Nelson (MN) calculated the force dependence of the effective torsional stiffness using the TWLC in the high-force limit

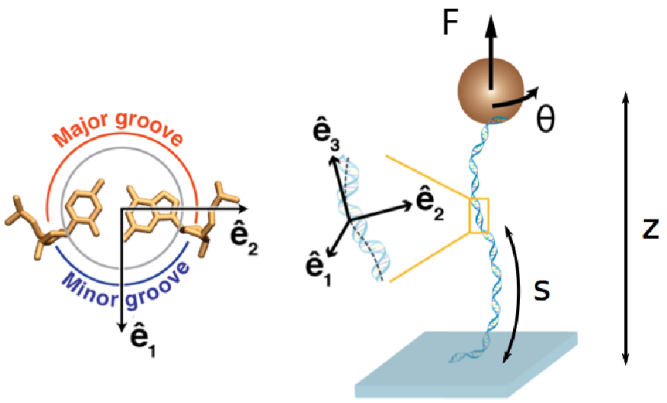

Figure 4.1: Schematic representation of a typical MT experiment. Magnetic fields are used to apply stretching forces and torques (inducing a rotation angle Θ) to a paramagnetic bead. A dsDNA molecule is attached at one side to the bead and at the other to a flow cell surface, separated by a distance z measuring the extension of the molecule. Continuum elastic models describe the double helix conformation using an orthonormal frame $\hat{e}_1$, $\hat{e}_2$, $\hat{e}_3$ at each point along the molecule, labeled by a coordinate s. $\hat{e}_3$ is tangent to the helical axis, while $\hat{e}_1$ points from the center of the helix towards the middle of the minor groove, and $\hat{e}_2 = \hat{e}_3 \times \hat{e}_1$.

(1st order) [78]:

$$C_{eff} = C \cdot \left(1 - \frac{C}{4A}\sqrt{\frac{k_B T}{AF}}\right) \tag{4.5}$$

The effective torsional stiffness C_{eff} decreases with decreasing stretching force F, described in Eq. 4.5. Note, that the MN model was already mentioned in Chapter 1 and 3.

The MN model qualitatively predicts the trend of the effective torsional stiffness with increasing force, but over predicts the exact values determined from experiments, in particular for forces smaller 3 pN. Schurr recently proposed an extension of the MN model, that is a two-state model, which assumes sub-states within the DNA helix that convert into each other in a cooperative fashion [80]. Doing so he was able to fit the effective torsional stiffness data of DNA more accurate. However, the existence of the sub-states is still speculative. A brief discussion is given in Chapter 1.3.1.

Another idea to account for the deviations of the MN model is to use the asymmetric elastic rod model with bending anisotropy, instead of the symmetric, isotropic elastic rod model to describe DNA, as done by Marko and Siggia in 1993 [181] and recently by Nomidis *et al.* [3].

4.3.2 The asymmetric, anisotropic elastic rod model

The asymmetric rod model can be seen as a correction of the oversimplified symmetric, isotropic elastic rod model. It accounts, on the one hand, for the groove asymmetry, i.e. the major and minor grooves that naturally occur in the DNA helix. On the other hand, bending is no longer isotropic, but anisotropic. That splits the bending stiffness into two parameters A_1 and A_2, meaning that bending along one axis is preferred. When considering DNA as asymmetric

a new coupling term, the twist-bend coupling G, arises in the energetic description of the deformation of the rod. For the forces considered here (< 10 pN), the stretch modulus and thus, the twist-stretch coupling can be neglected. We further refer to this model as *aTWLC* (also in Chapter 3).

$$E = \frac{1}{2} k_B T \cdot \int_0^{Lc} \left[A_1 \beta_1^2 + A_2 \beta_2^2 + C\omega^2 + 2G\beta_2\omega \right] ds \tag{4.6}$$

In the aTWLC model, the bending stiffness is described by A_1 and A_2, the torsional stiffness by C and the twist-bend coupling by G, all in dimension of length. Where ω measures the rotation perpendicular to the helical main axis, as explained previously. β_1 and β_2 describe the bending along one of the vectors $\hat{e}_1$ or $\hat{e}_2$ within the orthonormal frame, see Figure 4.1. The mean bending stiffness in this model is defined as $A = (A_1 + A_2)/2$ and the bending anisotropy is $\epsilon = (A_1 - A_2)/2$. In the model the renormalized bending κ_b and the renormalized twist stiffness κ_t are functions of ϵ, G, A and C. κ_b and κ_t are equivalent to the previously described bending and twist persistence length, respectively. Further information on the parametrization can be found in Reference [3]. Note, that the TWLC is a limiting case for the aTWLC model: taking DNA as isotropic ($A_1 = A_2$) and symmetric (G = 0) reduces Eq. 4.6 to Eq. 4.4. For $G = 0 = \epsilon$, κ_b equals A and κ_t equals C. Otherwise, κ_b and κ_t are smaller than A and C, respectively, implying that the presence of the twist-bend coupling softens the DNA molecule.

4.3.3 Coarse-grained measurements of the torsional stiffness of DNA

The torsional stiffness

To apply the TWLC and the aTWLC to the coarse-grained model of DNA we fix the bending persistence length to 43 nm and the torsional stiffness to 110 nm. The persistence length of DNA is salt dependent, thus, literature values vary between 40 and 50 nm for 100 to 150 mM monovalent salt (see Supplementary Figure S6 of Reference [3] for a collection of measured values and Chapter 1.3.1 for a discussion of the salt dependence). We find, from averaged force-extension data 43 nm ± 5 nm for the bending persistence length of DNA (not shown in this work), justifying the chosen value within this work.

The consensus in literature for the effective torsional stiffness of DNA at higher force, i.e. when the effective torsional stiffness C_{eff} is equal to the intrinsic torsional stiffness C, is between 100 and 110 nm measured with magnetic tweezers [34, 35, 179, 185]. Supplementary Figure S10 of Reference [3] illustrates a collection of values for C_{eff} measured with different modalities and for varying forces. Additionally, extrapolating C_{eff}, see inset of the re-scaled plot in Figure 4.2, results in C = 110 nm, which is thus used in this study.

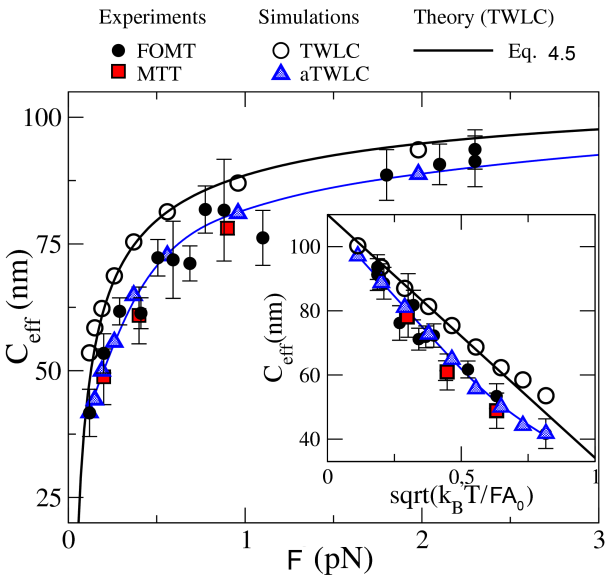

Figure 4.2: Force dependence of the effective torsional stiffness from MTT (present work) and FOMT [36] measurements, from simulations of the TWLC and the aTWLC model (where error bars are smaller than the symbols) and from the analytical TWLC approximation. Parameters are A = 43 nm and C = 110 nm for the TWLC and A = 56 nm, C = 110 nm, ϵ = 10 nm, and G = 40 nm for the aTWLC model. The inset shows C_{eff} as a function of the rescaled variable $\sqrt{k_BT/A_0F}$ (with A_0 = 50 nm); in these units Eq. 4.5 becomes a straight line. The experimental data are not well described by the TWLC, but agree quantitatively with the aTWLC model (reduced χ^2_{TWLC} = 6.1 and χ^2_{aTWLC} = 0.74, respectively). The blue line is an interpolation of the aTWLC simulation points.

The coarse-grained model of DNA is described in materials and methods and in Reference [3, 183]. Shown in Figure 4.2 are the measured and calculated results for the effective torsional stiffness (C_{eff}) of DNA at varying forces. The black solid line presents the theoretical prediction of the TWLC model with a fixed bending persistence length A = 43 nm and a fixed torsional stiffness C = 110 nm. Applying the TWLC model to the coarse-grained model of DNA, we find very good agreement between calculated values and theoretical values of C_{eff}. This implies that the coarse-grained model of DNA used, is valid to describe DNA mechanics. However, the predictions of the TWLC model overestimate the effective torsional stiffness. In particular for forces < 3 pN. Note, that there is a good agreement at 6.5 pN stretching force, where bending is totally suppressed and $C_{eff} \approx C$ (see also Chapter 3).

To apply the aTWLC model, the same values for the bending persistence length (i.e. the renormalized bending) and the intrinsic torsional stiffness are chosen. ϵ and G, however, are derived by fitting the model to the experimental data for the effective torsional stiffness and by minimizing the deviation between model and experiment, i.e. minimizing the reduced χ^2. An initial estimate of 25 nm on G was given by Reference [186]. Varying ϵ and G, by keeping always one parameter constant and comparing with experimental data, results in a best fit for ϵ = 10 nm and G = 40 nm ± 10 nm. Using these parameters one can determine the mean bending stiffness A = 56 nm and thus, the effective torsional stiffness of DNA for different forces. The predictions for C_{eff} (blue triangles) are in very close agreement with the experimental data (both, MTT data, red squares and FOMT data, blue circles in Figure 4.2). More details are in Reference [3].

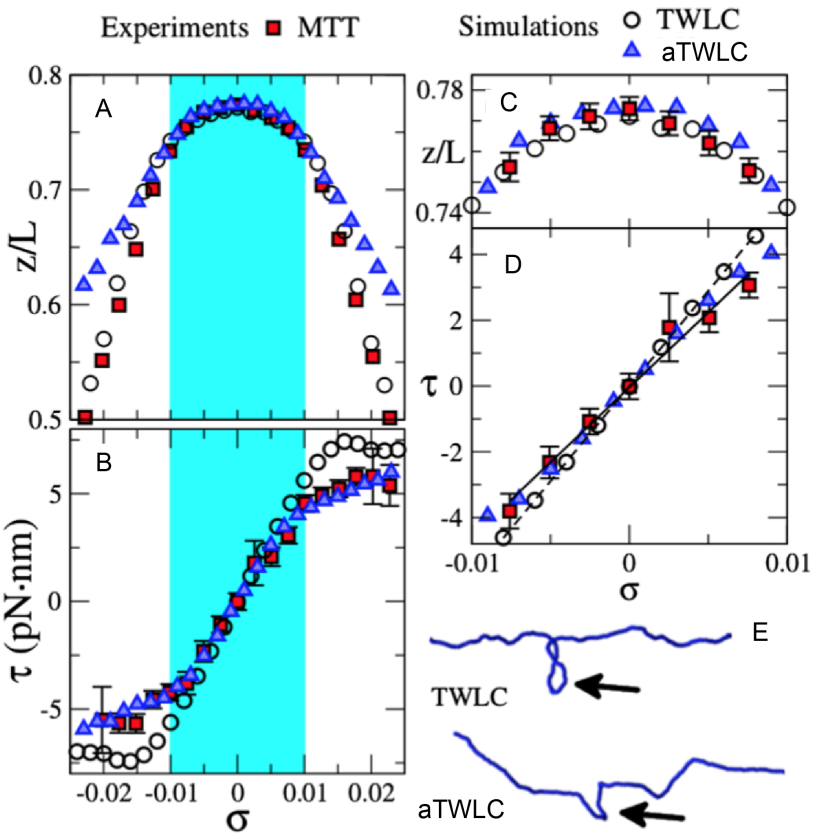

Figure 4.3: Extension-rotation and torque-rotation data from experiment and from coarse-grained calculations of the TWLC and aTWLC model. (A) Relative extension z/L and (B) torque τ vs. supercoiling density σ at F = 0.4 pN from MTT experiments (solid squares) and simulations of the TWLC (open circles, A = 43 nm, C = 110 nm) and aTWLC (solid triangles, A = 56 nm, C = 110 nm, G = 40 nm, and ϵ = 10 nm) models. (C, D) Closeups of z/L and τ in the pre-buckling regime, shaded area (A) and (B). (E) Snapshots of simulations of the TWLC and aTWLC models, respectively, at σ = 0.023. The arrows point to a plectonemic supercoil in the TWLC and to a solenoidal supercoil in the aTWLC model.

Torque-rotation data

In addition, coarse-grained extension-rotation and corresponding torque-rotation calculations using the TWLC and the aTWLC model are compared with high-resolution MTT data for three forces: 0.2, 0.4 and 0.9 pN. The results for 0.4 pN are shown in Figure 4.3, whereas the others are shown in Supplementary Figure S8 of Reference [3].

The extension-rotation data (red squares) and the coarse-grained simulations of the TWLC model (black circles) are in prefect agreement in the pre-buckling (turquoise shaded area) and in the post-buckling regime (Figure 4.3A). The aTWLC model, in contrast, fails to predict the extension-rotation data of DNA post-buckling. A possible reason is illustrated in Figure 4.3E. Snapshots of the coarse-grained simulations using the TWLC model (top) and the aTWLC model (bottom) at a supercoil desity σ = 0.023 show that the simulations of the aTWLC model do not form plectomenes (as shown for the TWLC model) but solenoidal supercoils. Note, that the supercoil density σ is just a re-scaled variable of the applied number of turns. σ is defined as the quotient of ΔLk and Lk0, where ΔLk is the applied number of turns and Lk0 the linking

number of the molecule at zero torque, respectively. However, in the pre-buckling regime (Figure 4.3C) the TWLC (black circles) model and the aTWLC (blue triangles) are both in good agreement with experimental data (reduced χ^2 = 1.6 and 0.77, respectively).

The comparison with torque-rotation data is contrary: there is a much better agreement for the aTWLC model (reduced χ^2 = 1.3) than for the TWLC model (reduced χ^2 = 5.9). Interestingly, the TWLC fails to predict the molecular torque post-buckling, in contrast to the aTWLC model (Figure 4.3B). Additionally, the aTWLC model fits the data more accurately pre-buckling, see Figure 4.3D.

4.4 Conclusion

In this work, we investigated coarse-grained simulations of double-stranded DNA and performed extension-rotation and torque-rotation simulations for two models, the symmetric, isotropic (TWLC) and the asymmetric, anisotropic (aTWLC) elastic rod model. Additionally, we performed high-resolution magnetic torque tweezers measurements and compared simulations with experiments. The aTWLC model, which is a correction of the oversimplified TWLC model, leads to a significantly better fit of the effective torsional stiffness of DNA under applied forces than the TWLC model. We conclude, that introducing a twist-bend coupling results in a good prediction for the effective torsional stiffness.

The quantitative agreement of the aTWLC model with experimental extension- and torque-rotation data in the pre-buckling regime further highlights the importance of including the twist-bend coupling term in the elastic model.

Although we showed that the aTWLC model is a more accurate mechanical model of dsDNA than the standard TWLC in the pre-buckling regime, there is still an open issue at a higher supercoil desity ($|\sigma|$), where neither of the two models fully agrees with the experiments. However, in future work it is of interest to further investigate the model in order to account for the experimental observables and to focus on measurements to directly observe the twist-bend coupling of DNA.

Acknowledgments

I thank Stefanos K. Nomidis for helpful discussions and input to this chapter.

Chapter 5

The Helical Twist of DNA Decreases with Increasing Temperatures *

Abstract

DNA is the carrier of all cellular genetic information and increasingly used in nanotechnology. Quantitative understanding and optimization of its functions requires precise experimental characterization and accurate modeling of DNA properties. A defining feature of DNA is its helicity. DNA unwinds with increasing temperature, even for temperatures well below the melting temperature. However, accurate quantitation of DNA unwinding under external forces and a microscopic understanding of the corresponding structural changes are currently lacking. Here we combine single-molecule magnetic tweezers measurements with atomistic molecular dynamics and coarse-grained simulations to obtain a comprehensive view of the temperature dependence of DNA twist. Experimentally, we find that DNA twist changes by $\Delta\mathrm{Tw(T)} = (-11.0 \pm 1.2)$ degree/(°C·kbp), independent of applied force, in the range of forces where torque induced melting is negligible. Our atomistic simulations predict $\Delta\mathrm{Tw(T)} = (-11.1 \pm 0.3)$ degree/(°C·kbp), in quantitative agreement with experiments, and suggest that the untwisting of DNA with temperature is predominantly due to changes in DNA structure for defined backbone substates, while the effects of changes in substate populations are minor. Coarse-grained simulations using the oxDNA framework yield a value of $\Delta\mathrm{Tw(T)} = (-6.4 \pm 0.2)$ degree/(°C·kbp) and suggest an important role for local, short-lived base-pair melting.

5.1 Introduction

DNA is the storage medium for genetic information in all cellular life and increasingly used as a construction material for artificially designed nanostructures. Many of the structural and mechanical properties and conformational transitions of DNA have been mapped out in a series of landmark single-molecule measurements [1, 92, 122, 182]. At the same time, significant

*This chapter is submitted by Kriegel *et al.* and currently under review at *Nucleic Acids Research.*

effort has been directed at modeling DNA at various scales, from atomistic models [187–189] to more coarse-grained representations [3, 72, 93, 190–195]. Precise knowledge and predictive models of the structural and mechanical properties of DNA and their dependencies on solution conditions are a prerequisite for a quantitative understanding – and ultimately optimization – of its biological and technological functions.

A central property of DNA is its helicity. Famously discovered by Watson and Crick [196] with experimental input from Franklin and Wilkins [197], the helicity of DNA has been measured using a range of methods, including X-ray diffraction [198], Förster resonance energy transfer [199] and AFM/STM imaging [200] and is in the range of ~10.5 bp/turn [52]. Measurements using circular plasmids and electrophoretic mobility have demonstrated that the overall helical twist of DNA depends on temperature, with twist decreasing with increasing temperature. Initial estimates [201] reported a change in the helical twist of ΔTw(T) = -4 to -5 degree/(°C·kbp); subsequent work, using the correct value for the unwinding angle per ethidium molecule [124, 202] obtained -10 to -11 degree/(°C·kbp). Later, measurements based on electrophoretic mobility were extended up to thermophilic temperatures [203] close to the DNA melting transition and found a linear temperature dependence up to 80°C with a coefficient of -10.5 degree/(°C·kbp) [204]. Strick *et al.* [145] observed unwinding of the helix at the level of individual molecules from (fairly limited) measurements on lambda-phage DNA in magnetic tweezers (MT). They found the helix to unwind by -13.4 degree/(°C·kbp), an effect ~30% larger than seen in previous bulk studies.

On the simulation side, Everaers and coworkers performed a molecular dynamics (MD) study of DNA over a broad range of temperatures [205] and found an average decrease of ~0.5° in the base step parameter twist in going from 0 to 77°C, which corresponds to a change in helicity of approximately -6.5 degree/(°C·kbp). Another MD and coarse-grained simulation study predicted roughly -4 degree/(°C·kbp) [206]. These estimates are about half of the experimentally determined value. However, a direct comparison with experiment is complicated by the fact that the local base pair step twist is generally not identical to the overall helical twist [49, 72, 194, 205, 207]. Importantly, the experimental measurements capture the relative global rotation of the two DNA ends and, therefore, a proper definition of the coordinate determined in simulations is important for a direct comparison.

Here, we use high-resolution single-molecule MT measurements to quantify the temperature dependence of the helical twist of DNA. We critically compare the experimental results to both atomistic MD and coarse-grained simulations using the oxDNA framework to provide a stringent test on current simulation protocols and to give microscopic mechanistic insight into the origin of the temperature dependence of DNA twist. Experimentally, we determine the temperature dependence of the helical twist of DNA ΔTw(T) using a novel custom-build implementation of a temperature-controlled MT. Our setup is similar to previous implementations of temperature controlled MT [103, 151] and was optimized for simplicity of operation and implementation as well as the ability to use the temperature control module as an optional add-on to an existing MT set up. Using this instrument, we obtained DNA rotation-extension curves (i.e. measurements of DNA tether extension vs. linking number) as a function of temperature, which allow us to determine the change in helical twist as a function of temperature in the range of 24°C to 42°C. Our measurements are in good agreement with prior bulk studies and, in addition, show that the temperature dependent helical change is not force-dependent,

in the force range where torque induced melting is negligible and the overall twist-extension response of DNA is symmetric (i.e. for stretching forces < 1 pN).

From a microscopic point of view, one would expect no change of the ensemble-averaged twist with temperature if the associated free energy profile is harmonic and temperature independent. However, the underlying free energy profile is a result of a large number of interatomic interactions involving not only DNA but also the surrounding water molecules and ions. In MD simulations, these interactions are captured by atomistic force fields, which are under constant development, with major updates released recently [208, 209]. To analyze the response of twist to temperature at atomic resolution, we performed a series of ~μs, atomic resolution, explicit solvent MD simulations of a mixed 33 base pair (bp) DNA sequence at temperatures ranging from 7°C to 47°C using the OL15 Amber force field [208]. Control simulations using the earlier released bsc0 force field [210] were also performed. We use a scheme involving coordinate frames at each end of the DNA molecule to determine the change in twist, mimicking the experimental setup. To investigate the microscopic origin of the twist temperature dependence, we use local conformational descriptors inferred from MD data for assessing various structural contributions to the overall twist change.

We complement the atomistic MD simulations with coarse-grained simulations using the oxDNA framework [211, 212]. Unlike atomistic models of DNA, coarse-grained models explicitly simulate only a reduced number of effective degrees of freedom, which are chosen such as to represent selected physically relevant processes in the system. While no longer allowing for the explicit representation of the full microstructure, coarse-grained models reduce the computational cost and allow access to time and length scales that currently cannot be treated in all-atom simulations. oxDNA represents DNA on the level of individual nucleotides which are treated as rigid bodies with three interaction sites coupled by physically motivated attractive and repulsive potentials. The model has been developed with a focus on the thermodynamics of double-strand denaturation and shown good agreement with the experimentally observed behavior of DNA under mechanical stress in a variety of systems [87, 211, 213, 214]. A combination of the atomistic and coarse-grained perspectives has proven beneficial to provide a comprehensive picture of the molecule at multiple scales, e.g. to study DNA under superhelical twist in closed circular systems [214]. Our oxDNA simulations of a 600 bp DNA construct allow us to compare the atomistic and coarse-grained perspectives and, in particular, to test to what extent the observed temperature dependence of DNA twist can be captured by oxDNA.

5.2 Materials and methods

5.2.1 Magnetic tweezers measurements

Experiments on DNA were performed in a home-built magnetic tweezers setup described in Section 2.2.1 and Reference [2]. For temperature-controlled measurements we supplied the setup with two heating circuits: one for objective heating and one for baseplate heating. We attach a single heating foil (KHLV-0502/10-P, Omega) around the objective (60x, Plan Fluorite with correction collar, NA 0.9 or 100x, Plan Fluorite, NA 0.75, Olympus) and two separate heating foils to the bottom of the baseplate (Supplementary Figure 5.6). We chose the material of the baseplate to be aluminum because of its good heat conductivity. The two circuits are

connected in series and operate with the same power supply (HWS-50A-24/A, TDK-Lambda). Each circuit is controlled by a PID controller (CN7823, Omega) and via solid-state relays (SSRDC100VDC12, Omega). Pt100 temperature sensors (SA1-RTD, Omega), placed as indicated in Supplementary Figure 5.6, serve as temperature sensors in both circuits in the feedback loop (Supplementary Figure 5.10). We used the vendor (Omega) provided software for control and read-out. For the connection of the controller to the computer a RS485 to USB converter (USB-RS485-WE-1800-BT, FTDI Chip) was used (Supplementary Figure 5.10). Measurements used 7.9 kbp and 20.6 kbp DNA constructs described previously [34, 178] and MyOne beads (streptavidin-coated 1.0 μm diameter MyOne; Life Technologies). The preparation of the flow cell, and the selection of tethers are carried out as described in Chapter 2 and in Reference[2]. Rotation-extension measurements to determine the helical twist of DNA were performed using conventional magnetic tweezers with two cubic magnets (5 x 5 x 5 mm^3; W-05-N50-G, Supermagnete), oriented in a vertical configuration [42].

5.2.2 Molecular dynamics simulations

We used a DNA oligomer (33 base pairs, sequence GAGAT-GCTAA-CCCTG-ATCGC-TGATT-CCTTG-GAC), that was previously used to study DNA allostery [215, 216]. In the simulations we used the SCP/E water model and added 150 mM KCl salt parameterized according to Dang [217]. The equilibration protocol was identical to that in Reference [216]. Independent trajectories of 1 μs each at 1 atm and at 280 K, 290 K, 300 K, 310 K and 320 K, (7°C, 17°C, 27°C and 37°C) were calculated using the Amber suite of programs and the OL15 [208] and bsc0 [210] force fields. The mass repartition scheme implemented in the pmemd module of Amber enabled us to use a time step of 4 fs [218]. Mass repartition was only used for the solute with bond constraints on all bonds involving hydrogen atoms using the SHAKE algorithm [219]. Mass repartition was not used for the solvent since the analytic bond constraint algorithm, SETTLE [220], used for the solvent is compatible with a 4 fs time step even with the original mass distribution. The scheme has been found to give thermodynamic and kinetic results compatible with simulations without mass repartition for several test systems [218]. Conformational analysis programs 3DNA [221] and Curves+ [222], as well as in-house scripts, were used for the analysis.

5.2.3 Coarse-grained simulations using oxDNA

We simulated a 600 bp DNA double-strand using the oxDNA2 version of the model [212] which includes a Debye-Hückel representation of screened electrostatics, and set the monovalent ionic strength to 150 mM to match experimental conditions. OxDNA simulations were run at T= 300 K, 310 K, 320 K, and 340 K (27°C, 37°C, 47°C, and 67°C). Double strands are set up in a homogeneously underwound state with a fixed overall twist angle. After pre-equilibration, production simulations are run for at least 2.5 μs of simulated time for each system. As in previous applications of oxDNA to similar systems [87] the overall twist of the system is kept constant by fixing the strand ends in stiff harmonic traps and preventing the double strand from passing over its own ends. Being an implicit-solvent model, oxDNA requires addition of a noise term to Newton‘s equations of motion to ensure the appropriate representation of diffusive behavior of particles. As in previous work [87, 214], this was implemented using an

Andersen-like thermostat [223].

Model for the effect of local base pair melting on overall DNA twist

In the oxDNA runs, we observed delocalized and short-lived broken base pairs (see main text and Supplementary Figure 5.13). We can estimate the effect of these short-lived defects by performing an average over the twist angles along a double strand that has N_D denatured base pairs, out of N total base pairs. Since the single denatured base pairs are separated along the double strand, they typically cause disruption of two consecutive twist angles (the one with their precursor and their successor). The change in average twist angle $\langle\alpha\rangle$ can be estimated as follows (where α_D and α_0 are the twist angle of denatured and intact base pairs, respectively), assuming that α_D and α_0 remain constant and that the dominant effect is a change in N_D with temperature:

$$\frac{d\langle\alpha\rangle}{dT} \approx \frac{2}{N-1}(\alpha_D - \alpha_0)\frac{dN_D}{T} \tag{5.1}$$

5.3 Results and discussion

5.3.1 Temperature controlled magnetic tweezers measurements

In magnetic tweezers (MT) DNA molecules are tethered between ~μm-sized magnetic particles and a flow cell surface [30, 41, 42] (Figure 5.1A). Magnets mounted above the flow cell enable the application of calibrated stretching forces [42, 43, 224] and can be used to control the twist of the DNA tether [11, 41, 91, 174, 178].

To control the temperature of the flow cell environment, we mounted resistive heating foils and thermocouple temperature sensors to both the metal baseplate of the flow cell holder and around the objective (Supplementary Figure 5.6). We tested three options for temperature control: only objective heating, only baseplate heating, and the combination, objective and baseplate heating in parallel. In all cases the current through the heating foils was controlled with a PID controller that enabled independent control of the objective and baseplate heating circuits. Using a custom-made flow cell with temperature sensors inserted at the approximate position of the field of view of the microscope and at the flow cell periphery, we found that objective heating is sufficient to reliably heat the system locally (Supplementary Figures 5.6 and 5.7), but leaves the temperature at the edges of the flow cell (far away from the objective) almost unaffected. Conversely, we found that if only the baseplate was heated, the temperature at the position of the objective was almost unaffected (Supplementary Figure 5.6). For applications where it is sufficient to temperature control the local environment in the observation volume of the MT measurement, we found that objective heating alone is sufficient. In particular, using objective heating only, the feedback sensor located at the objective, a temperature sensor inserted into the immersion oil between objective and flow cell surface, and a sensor in the observation volume within the flow cell all gave consistent temperatures (< 0.5°C deviation; Supplementary Figure 5.7).

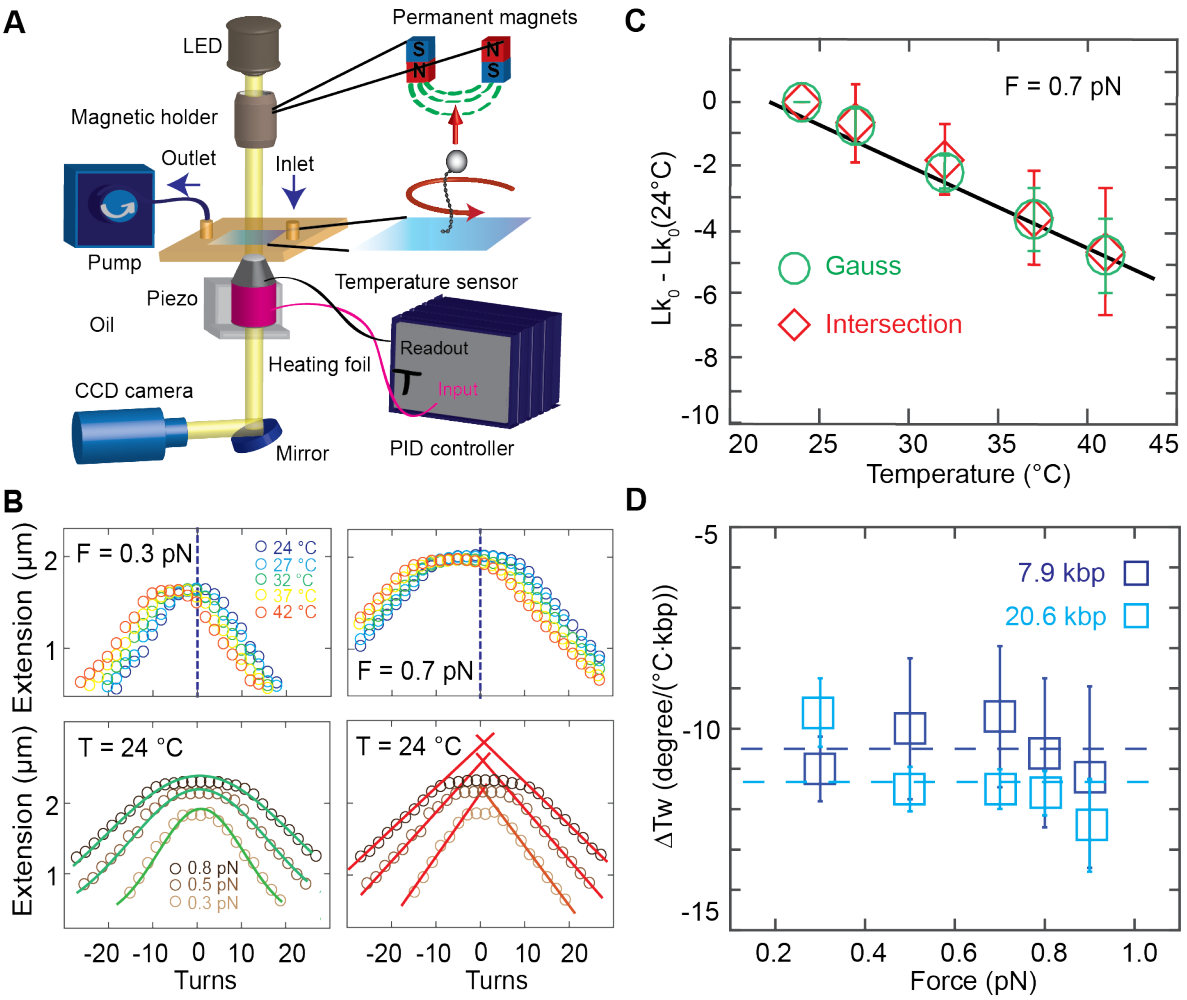

Figure 5.1: Temperature controlled DNA rotation-extension measurements. (A) Schematic of the temperature controlled magnetic tweezers setup. In MT, DNA is tethered between the surface and magnetic beads in a flow cell. An inverted microscope is used to image the flow cell surface onto a camera. Monochromatic light illuminates the flow cell from top. Permanent magnets are placed on a translational and rotational motor on top of the flow cell to apply stretching forces and torsional control, respectively. A pump is used for buffer exchange. A heating foil around the objective is used to locally heat the flow cell and controlled using a PID controller. (B) Top: Rotation-extension measurements for 7.9 kbp DNA at 0.3 pN (top left) and 0.7 pN (top right) and different temperatures. The center of the extension vs. turns curve shifts to negative turns with increasing temperature. Bottom: Illustration of the approaches to determining the centers of the rotation curves. Gaussian fits (green lines) to the extension vs. applied turns data at F = 0.3 pN, 0.5 pN and 0.8 pN. The center of the Gaussian function of each curve is used to determine the center of the curves along the turn axis (bottom left). Linear fits (red) to the plectonemic regime of the rotation-extension curves at positive and negative applied turns. Here the intersection of the linear fits is used to determine the center (bottom right). (C) Changes in the DNA linking number with temperature are determined from the shift of the centers of the rotation curves. Data shown here are for 7.9 kbp DNA at 0.7 pN; symbols and error bars are the mean and standard deviation from seven molecules. ΔTw(T) is determined from the fitted slope. (D) Temperature dependence of the helical twist ΔTw(T) as a function of applied force. Data are for 7.9 kbp DNA (dark blue) and 20.6 kbp DNA (light blue), respectively. Symbols and error bars are the mean and standard error of the mean from at least seven individual molecules for each measured force and DNA length. The change in helical twist does not depend on force, within error, as both data sets are consistent with a force-independent ΔTw(T) (dashed lines; reduced χ^2 = 0.04 for the 7.9 kbp DNA with ΔTw(T) = (-10.5 ± 0.6) degree/(°C·kbp); reduced χ^2= 0.24 for the 20.6 kbp DNA with ΔTw(T)= (-11.5 ± 1.0) degree/(°C·kbp)).

Use of objective heating only has the advantage of requiring only one simple heating circuit that can readily be added to existing MT setups. Using this approach, we control the temperature in the local flow cell environment from room temperature to 42°C (which is the maximum recommended temperature for the used objective by the vendor's specifications), achieving constant temperatures over long periods of time (> hours). The heating circuit is fast and reaches the adjusted temperature in approximately one minute. However, in order to have constant temperatures from the beginning, it is recommended to let the system equilibrate for 15 to 20 minutes. We observed that the expansion of the brass objective upon heating leads to a systematic change in the vertical position of plastic beads unspecifically attached to the flow cell surface that was monitored using the standard MT position tracking procedures. The observed expansion was consistent, within experimental error, with the thermal expansion coefficient of brass (Supplementary Figure 5.8). We note that even though we used a separate temperature sensor on the objective for feedback in all measurements reported here, in principle the tracked position of fixed reference beads could be used for temperature feedback, if it is desirable to simplify the temperature control circuitry even further.

5.3.2 Experimental determination of the temperature-dependence of DNA twist

Using our temperature controlled MT set up, we recorded rotation-extension curves for a 7.9 kbp (Figure 5.1B) and a 20.6 kbp DNA (Supplementary Figure 5.9) construct attached to the flow cell surface via multiple digoxigenin-antidigoxigenin labels and to 1.0 μm-diameter magnetic MyOne beads via multiple biotin-streptavidin linkages. We recorded traces in the force range from 0.3 pN to 0.9 pN and the temperature range from 24°C to 42°C. The rotation-extension curves shift systematically along the turn-axis to a negative number of turns with increasing temperature (Figure 5.1B). To systematically quantify the shifts in the rotation-extension curves, we used two different approaches to determining the centers of the rotation curves (Figure 5.1B, bottom), which corresponds to Lk0, i.e. the point where the DNA molecule is torsionally relaxed. One approach is to fit a Gaussian to the extension vs. applied turns data and to use its center position as Lk0 (Figure 5.1B, bottom left). A second approach is to perform line fits to the regions where the tether length decreases linearly with the applied number of turns, i.e. the plectonemic regions of the rotation-extension curves, and to then determine the intersection points of the fitted lines as Lk0 (Figure 5.1B, bottom right). While both methods gave identical results (Figure 5.1C), within experimental error, we found the approach of fitting a Gaussian to be more robust, since it does not require setting a fitting range, and we used the Gaussian fits in the subsequent analyses.

The change in Lk0 determined from rotation-extension curves with temperature is linear (Figure 5.1C). Averaging over all forces, we find a change in DNA helical twist of ΔTw(T) = (-10.5 ± 0.6) degree/(°C·kbp) for the 7.9 kbp DNA construct and ΔTw(T) = (-11.5 ± 1.0) degree/(°C·kbp) for the 21 kbp construct, where we have reported the mean and standard error of the mean determined from nine and seven individual molecules, respectively. In the range studied (0.3 to 0.9 pN), we do not see any statistically significant force dependence of ΔTw(T), for neither of the two DNA constructs. We note that it is straight-forward to apply larger forces in the MT; however, at forces $\geq$ 1 pN the rotation-extension behavior becomes asymmetric, due to torque induced melting of DNA upon underwinding [90, 145], which precludes the determination of

the curves' centers as outlined in Figure 5.1B. Therefore, we limited our analysis to the range of forces that avoids torque-induced melting. Our results for the overall value of ΔTw(T) for the two DNA constructs investigated are in agreement, within experimental error, with one another and with previous bulk measurements. Nonetheless, we find that the change in the helical twist for our 20.6 kbp DNA construct is ~10% larger compared to the 7.9 kbp construct. This small difference might be due to the difference in GC content of the constructs -the 7.9 kbp DNA consists of 55% GC, while the 20.6 kbp DNA has 45% GC- or due to other sources of experimental variability.

5.3.3 Molecular dynamics simulations of temperature-dependent changes of DNA twist

Our ability to accurately measure the overall change in DNA helical twist with temperature provides a sensitive test for current MD force fields for nucleic acids. Conversely, atomistic MD simulations have the potential to provide microscopic mechanistic insights into the change in twist of DNA with temperature. We performed atomic-resolution MD simulations of a 33 base pair mixed DNA sequence with explicit inclusion of water molecules and ions at five different temperatures ranging from 7°C to 47°C. The newly released OL15 force field [208] was used to model DNA interatomic interactions. Simulations were run for 1 μs at each temperature and snapshots were recorded every 10 ps.

To compare the MD results to experimental data, we extracted the DNA end-to-end twist in a way that closely mimics the experimental measurements. Two coordinate frames were assigned to the ends of the DNA molecule (Figure 5.2A) that were defined as follows: First, for the three penultimate base pairs at each end (base pairs 2-4 for R1 and 30-32 for R2, Figure 5.2A, red ellipses) the standard base pair coordinate frames [225] were computed and subsequently averaged using the quaternion averaging introduced in Reference [226]. Second, each mean frame was projected onto the mean helical axis, computed as the average of the helical axes assigned to the three pairs by the 3DNA conformational analysis program [221]. Third, the end-to-end twist between the two frames R1 and R2 was computed, using a definition exactly analogous to the local base pair step twist employed in 3DNA. In this "mean plane" definition the twist is the rotation in the plane normal to the mean of the Z-axes of R1 and R2. The mean plane definition has the property that twist differences are invariant with respect to the initial constant rotation offset of the frames about their Z-axes. This definition corresponds to the experimental setup where the initial rotational setting of the beads is also not known.

The end-to-end twist was analyzed for each of the snapshots of the MD trajectory at all simulated temperatures (Figure 5.2B, data in red). We find the twist to decrease almost linearly in the range of 7°C to 47°C. The least-squares fitted linear dependence gives ΔTw(T) = (-11.1 ± 0.3) degree/(°C·kbp), in excellent quantitative agreement with experimental values. The underlying end-to-end twist free energy landscapes computed by the Boltzmann inversion of the probability distributions (Figure 5.2C) are nearly harmonic, with slight anharmonicities only for undertwisting at low temperatures (roughly starting from a 37 degree undertwist at 7°C and 17°C, marked by a vertical line in Figure 5.2C).

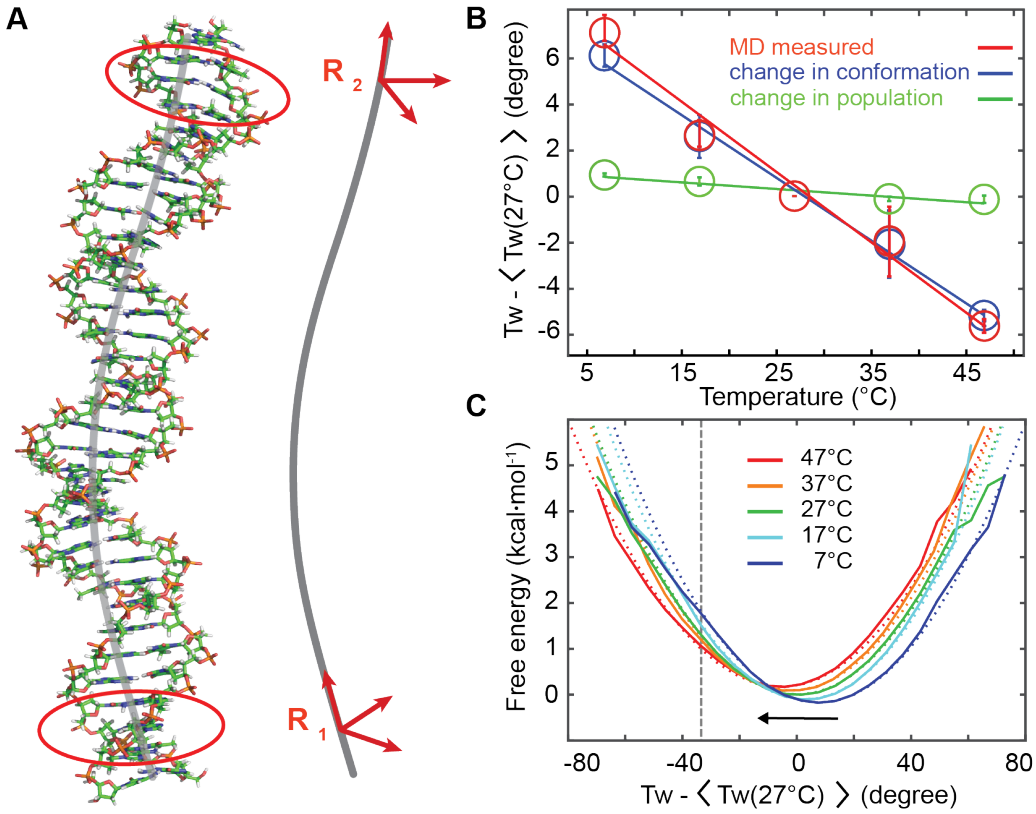

Figure 5.2: Determination of DNA twist from atomistic MD simulations. Results from atomic-resolution unrestrained molecular dynamics (MD) simulations of a 33 bp DNA oligomer at different temperatures. (A) Snapshot of the DNA structure from a MD simulation and definition of the right-handed orthonormal frames that were attached to the oligomer ends, mimicking the experimental setup. Base-fixed frames in three pairs close to the ends (marked by red ellipses) were averaged and then projected onto the helical axis (gray), yielding the end frames R1 and R2. (B) End-to-end twist between R1 and R2 as a function of temperature (red circles). Symbols are the average over the entire trajectory, error bars are estimated by repeating the analysis for the first and the second halves of the trajectories and calculating mean difference between these values and the value for the entire trajectory. The resulting twist temperature slope (red line) for the OL15 Amber force field is (-11.1 ± 0.3) degree/(°C·kbp). We decompose the change in twist with as a superposition of the change in populations of the BI/BII backbone substates and the conformational change of the individual substates. It is seen that the change in BI/BII substate populations, with substate conformations taken constant (green) contributes only very weakly, whereas the conformational change of the individual substates (blue) almost account for the total observed change. (C) Twist free energy landscapes computed from the Boltzmann inversion (solid lines) and harmonic fits with the same mean and variance (dotted lines). The potentials are overall harmonic, with a slight anharmonicity for undertwisting at low temperatures (to the left of the indicated grey, vertical line). All twist values are plotted relative to the mean twist at 27°C.

Employing identical simulation protocols and twist definitions, we performed simulations with the earlier bsc0 Amber force field [210]. Once again, the twist decreases almost linearly with temperature and the underlying free energy profiles are nearly harmonic. However, the slope is (-7.5 ± 1.7) degree/(°C·kbp), which deviates significantly from the experimental value and from the MD simulations with the OL15 force field. The simulated oligomer using bsc0 suffers from numerous base pair breaks and transient non-canonical states of the glycosidic angle χ near the oligomer ends. However, filtering out these contaminated snapshots changes the twist temperature dependence slope only weakly, indicating the slope to be an intrinsic

property of the bsc0 parameter set and not an end effect. Thus, the OL15 force field captures the fine phenomenon of twist temperature dependence better than the earlier bsc0 force field.

We performed control calculations to test whether the definition of twist angle had an influence on the results. Three alternative definitions of twist were analyzed. One approach is to define the end frames R1 and R2 as above but to compute the end-to-end twist using the axis-angle rotation parameters, used e.g. in the conformational analysis program Curves+[222]. In this "axis-angle" approach, the relative rotation from R1 to R2 is parameterized by a vector whose length is equal to the rotation angle and whose direction is that of the rotation axis. The twist is defined as the third component of the vector in any of the two frames R1 or R2. Two additional approaches to computing the twist are based on summing individual contributions along the helix. These approaches computed the total twist either as the sum of either local twists or as the sum of helical twists along the oligomer (between base pairs 3 and 31). The local base pair step twist is a parameter of the rotation connecting two successive base pairs, irrespective of the helical axis. The helical twist, in contrast, describes the rotation with respect to the helical axis. While the two are often similar in DNA, they are different in e.g. the A-RNA helix where the bases are inclined with respect to the helical axis [225].

The results are summarized in Figure 5.4 (and Supplementary Table 5.1). Since the axis-angle twist is not invariant with respect to the rotation offset, the computed values for ΔTw(T) vary with the initial rotational setting and a range of values is reported (Supplementary Table 5.1). For each force field, we find that the range of values for ΔTw(T) from the axis-angle definition overlaps with the value determined using the mean-plane definition. Summing the local or helical twists yield similar, though not identical, slopes compared to the end-to-end twist definitions. The only exception is the sum of the helical twist using the 3DNA definition that give consistently smaller slopes, for both force fields. Independent of the definition of twist, the bsc0 force field consistently finds slopes that are too small, by about a factor of two, compared to both the OL15 force field and the experimental data. The temperature dependence of the DNA twist of -6.5 degree/(°C·kbp) deduced by Everaers and coworkers [205] is very close to the values that we find using the same bsc0 force field.

In summary, the mean-plane end-to-end twist has the advantages i) that it closely mimics the experimental situation and ii) that it is does not depend on the rotation offset. We note that the end-to-end twist does not depend on the local twists only, but also on local bending coordinates roll and tilt (see below), which are in general not zero.

Microscopic model for the change in twist from MD simulations

To obtain insight into the microscopic mechanism for the observed temperature dependence of DNA twist, we first explore the possibility of local melting, i.e. breaking of the Watson-Crick base pairs. We consider a pair to be broken if at least one hydrogen bond is broken, defined by a donor-acceptor distance greater than 4 Å. The populations of the broken pairs are illustrated in Figure 5.5. We note that the amount of melting observed in the MD simulations is in agreement with the values found in oxDNA simulations (see below). However, the molten base pairs in the MD simulations do not have a significant effect on the overall change in twist with temperature (Supplementary Figure 5.14). This indicates that local melting is not the main mechanism for the temperature dependence of DNA twist in MD simulations. This may be due to the rather small perturbation of the local base pair step geometry. For instance, the local twist of steps

containing a broken pair is still 33.5 degrees for OL15 and 31.5 degrees for bsc0 on average, with standard deviations increasing from ca. 6 degrees at 7°C to 9 degrees at 47°C for both force fields.

Another potential mechanism for the temperature dependence of DNA twist might be related to the flips of the backbone angles γ from their canonical g+ to t conformation. These flips are rare and reversible in MD using modern force fields [208–210], but are associated with very low local twist and may therefore play a role. However, excluding the snapshots with at least one γ flipped does not change the twist temperature slope in any significant way (Supplementary Figure 5.14).

Thus, other conformational changes must be operative in MD. The end-to-end twist depends on the end frames, which, in turn, are functions of the orientation of the individual bases. For further analysis we use an approximation, which expressed the end frames in terms of the local rotational coordinates, parameterized by the local rotational coordinates of each step (local tilt, local roll and local twist, respectively). The local coordinates may depend on temperature through various mechanisms. One obvious possibility is related to the DNA backbone substates BI and BII that we observe in our simulations. A lot of research effort has been devoted to decipher the dependence of DNA structure on BI/BII substates (see for instance [227, 228]). In particular, it has been discovered that the conformation of a given step depends not only on the BI/BII backbone states within that step but also on the states of neighboring backbone fragments, both on the 5' and the 3' side (for a detailed discussion see [229] and references therein). Thus, the conformation of a given step depends on 6 backbone fragments, two inside the step, two at its 3'side and two at its 5'side. Since each fragment can be in one of two substates (BI or BII), we have 64 substates to consider for every step. As temperature changes, the populations of these 64 substates also change, implying a change of the step conformation. The differences in conformation between the substates can be quite significant – local twist may change by several degrees [229]. The resulting change, however, is far from obvious as, for instance, the inner and the 5'outer BII states increase, whereas the 3'outer BII states decrease local twist [229]. In addition to changes in the backbone substate populations with temperature, the step conformation for a fixed substate can also be temperature dependent, which we investigated separately.

Thus, the change of the local coordinates is decomposed into two contributions: the change due to the temperature dependence of the substate populations assuming constant substate conformations and the change of the substate conformations assuming constant populations.

If both terms are included, the predicted ΔTw(T) is (-10.8 ± 0.2) degree/(°C·kbp), very close to the slope obtained by directly monitoring the end-to-end twist (-11.1 ± 0.3) degree/(°C·kbp), red data in Figure 5.2B). Keeping just the first term implies a model in which the temperature change of the end-to-end twist is exclusively due to change in populations of the BI/BII backbone substates. However, the results show that this model predicts almost no change of the twist with temperature at all (Figure 5.2B, green), its slope being just (-1.0 ± 0.1) degree/(°C·kbp). In contrast, keeping just the second term implies a model in which the change of end-to-end twist takes place exclusively due to temperature changes in conformation of the individual backbone substates. This second model gives ΔTw(T) = (-9.7 ± 0.1) degree/(°C·kbp), suggesting that it is the conformational change of the individual BI/BII backbone substates that is largely responsible for the observed temperature dependence of DNA twist, while the changes in substate populations with temperature play only a minor role.

5.3.4 Coarse-grained simulations of DNA with oxDNA

To complement the atomistic MD simulations, we performed coarse-grained simulations using oxDNA. An advantage of coarse-graining is that much longer DNA molecules can be simulated as is currently possible using atomistic representations. We performed simulations for several 600 bp DNA systems, ~20-fold larger than the MD simulations and approaching the DNA lengths used in MT. Simulations were run at various levels of twist and subject to a constant pulling force of 0.7 pN at 27°C, 37°C, 47°C, and 67°C using the oxDNA average parameterization, which uses one set of parameters for all base pairs (Figure 5.3). Control calculations using the sequence-dependent parameterization of oxDNA on 600 bp systems with random sequences of a GC content of 45 and 55 percent gave essentially identical results, within error (Supplementary Figure 5.12).

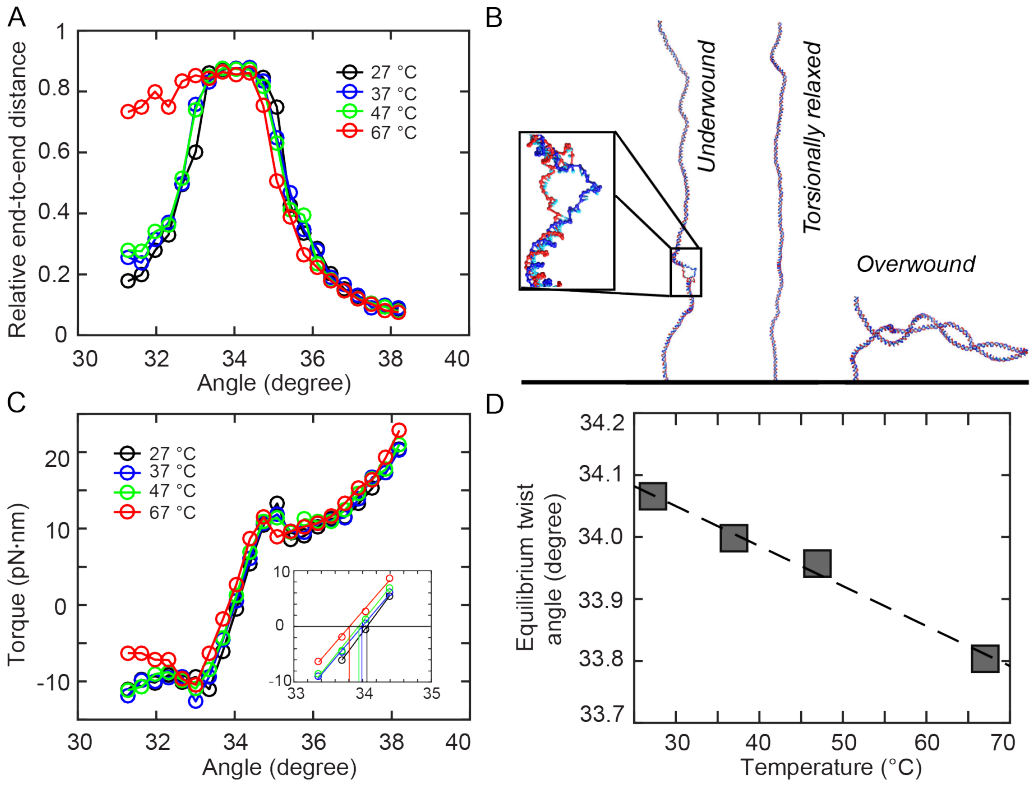

Figure 5.3: Coarse-grained oxDNA simulations. Results from coarse-grained oxDNA simulations of a 600-bp double-stranded DNA system in the average-base parametrization at 150 mM monovalent salt. F = 0.71 pN was used in all simulations. (A) Extension vs. imposed mean twist angle for 27°C, 37°C, 47°C and 67°C. Note that for 67°C, denaturation bubble formation occurs in the undertwisted system (angles ≤ 33 degree), leading to asymmetric curves. (B) Molecular conformations observed in oxDNA simulations at T = 67°C for an angle of 31.6°, showing a denaturation bubble (left), 34.0°, showing an extended double strand (centre) and 37.2°, showing a plectoneme (right). For 31.6° snapshot, a closeup of the 23-bp denaturation bubble is shown in the inset. (C) Torque response at different temperatures, showing a linear regime close to the equilibrium angle, followed by an overshoot and a post-buckling torque which increases more slowly upon further twisting. The inset shows a zoom of the data with the interpolation in the linear torque-regime and determination of the equilibrium angle corresponding to zero torque. (D) Equilibrium twist angles for the different temperatures determined by linear interpolation of the torque response shown in C to zero torque. The black line indicates a linear fit of temperature dependence, yielding $\Delta Tw(T)$ = -6.5 degree/(°C·kbp).

oxDNA reproduces the rotation-extension response of double-stranded DNA under twist and tension (Figure 5.3A and Supplemental Figure 5.11). A direct comparison to the experimental curves for F = 0.7 pN and 37°C shows good agreement of extensional behavior (Supplementary Figure 5.11). For 67°C, we observe an asymmetric extension curve, indicating thermally aided melting upon underwinding, similar to previous experimental results [103]. Representative structures from oxDNA simulations in the linear, plectonemic and partially denatured states are shown in Figure 5.3B. The torque response of the simulated system as a function of the average twist angle per base pair step shows a linear torque response for small deviations from equilibrium twist (Figure 5.3C). Upon further over- or under-winding, the system exhibits a torque overshoot at the point where the DNA buckles to form plectonemes, similar to experimental observations [38, 48, 171] and a post-buckling state for which the torque increases more slowly upon further twisting (Figure 5.3C). Unlike for larger molecules usually used in experiments, the post-buckling torque is not strictly constant in the simulations due to a finite size effect: for high twist, the plectoneme takes up almost the entire simulated 600 bp double strand. In this situation, further twist can only be absorbed by tighter winding of the end loop, leading to a small but nonzero torque response.

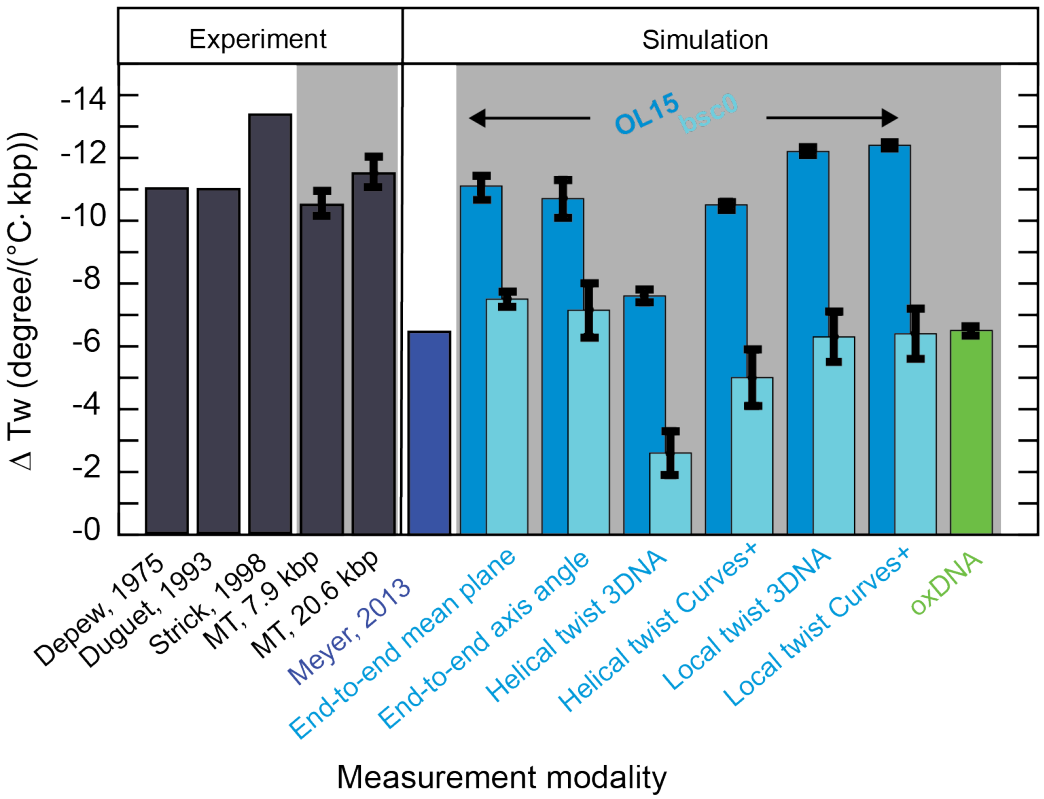

Figure 5.4: Values for the change of DNA twist with temperature ΔTw(T) from measurements and simulations. Dark grey bars indicate values obtained from experiments. Indicated with the light dark background are values that were obtained as part of this work. Blue colors refer to data from all-atom MD simulations. Lighter blue colors represent data generated in this work with the OL15 and bsc0 force fields, respectively. Green represents the value gained by coarse-grained oxDNA simulations within this work.

We observe an overall shift of the torque response to induced twist to smaller measured angles upon heating, indicating a decrease of the average twist angle per base pair with increasing temperature. As described in previous work [87], extension curves of the 600 bp simulated system exhibit larger finite-size effects compared to the experimental system, making it difficult to determine the zero-twist state by directly fitting to the extension curve as done for experimental data. Hence, we determined the mean twist angle of the torsionally relaxed state directly from the torque response by interpolating the linear part of the torque response curve to determine the angle corresponding to zero torque (Figure 5.3C, inset). The resulting mean twist angle for zero torque decreases as a function of temperature (Figure 5.3D). A linear fit of the temperature dependence yields a change of (-6.4 ± 0.2) degree/(°C·kbp), which is smaller than the experimentally determined value, but still relatively close to the experimental results, in particular for the 7.9 kbp DNA measurements. Various approximations are inherent in the coarse-graining approach of oxDNA, concerning both the molecule structure and the representation of physical interactions experienced by the molecule. Given these simplifications, the value obtained with oxDNA is in fair agreement with the experimental findings and at the level of deviations observed for the different atomistic force fields (bsc0 and OL15, Figure 5.4).

Delocalized melting of base pairs in oxDNA simulations

Given the encouraging, semi-quantitative agreement between the temperature dependence of DNA twist predicted by oxDNA with the experimentally determined value, we again analyzed the simulated conformations to gain a mechanistic understanding of the observed trend. As in previous applications of the oxDNA framework [87], we defined base pairs to be broken when their hydrogen-bonding interaction energy dropped below -4.13·10^{-21} J, corresponding to approximately 15% of the value for a fully formed bond. We observe intermittent, short-lived opening of base pairs in the double-strand due to thermal fluctuations, which do not however lead to stable formation of denaturation bubbles (Supplementary Figure 5.13). Depending on temperature we find on average between 0.6 base pair breaks at 27°C up to 2.2 at 67°C for the torsionally relaxed 600 bp system (Figure 5.5). In order to determine if the decrease of the mean twist angle with temperature observed in simulations is due to the local base pair melting, we developed a simple model to calculate the effect of denaturing single base pairs on the average twist angle (materials and methods) and apply it to systems which are almost torsionally relaxed at the different simulated temperatures. Using the simulation data, our model predicts a twist angle decrease from delocalized base pair denaturation alone of -5 degree/(°C·kbp). This value is close to the total twist change with temperature observed in the oxDNA simulations; these findings suggest that in the oxDNA simulations, the overall unwinding of the DNA helix with increasing temperature can almost be entirely attributed to delocalized and short-lived base pair melting.

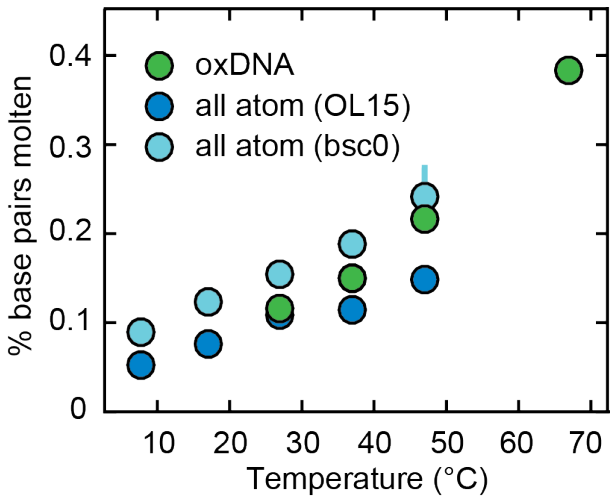

Figure 5.5: Fraction of broken base pairs as a function of temperature. In the all-atom molecular dynamics calculations with the OL15 (dark blue circles) and bsc0 (light blue circles) force fields the two base pairs at each end of the oligomer were excluded from the analysis and broken bases are defined as bases where at least one hydrogen bond donor-acceptor distance exceeds 4 Å. In oxDNA (green circles) broken bases are defined as base pairs where the interaction energy is less than 15% of the value for a fully formed pair. Errors (from splitting the trajectory in half) are smaller than symbols for most points.

5.4 Conclusion

We have presented a new, operationally straight-forward implementation of temperature controlled MT and used the instrument to determine the change in DNA twist with temperature ΔTw(T). We find ΔTw(T) to be independent of force, in the force range that avoids torque-induced melting, and to be independent of GC content, within experimental error. Averaging over all MT data, we obtain a value of ΔTw(T) = (-11.0 ± 1.2) degree/(°C·kbp). Atomistic MD simulations find ΔTw(T) values in excellent quantitative agreement with experiments (Figure 5.4). To determine accurate values for ΔTw(T) from MD simulations, care must be taken to properly define the end-to-end twist, as opposed to simply summing the individual base pair step twist values, which tends to yield smaller values for ΔTw(T). In addition, we found that the OL15 force field yields significantly more accurate results compared to the older bsc0 parameter set (Figure 5.4). The excellent agreement between MD simulations and experiments found in this work suggests that current nucleic acids force fields and simulations protocols are sufficiently advanced to predict even subtle features of DNA structure.

Coarse-grained simulations using the oxDNA framework yield values of ΔTw(T) that are slightly smaller, but that are still reasonably close to experimental results. This level of agreement is encouraging, given the considerable approximations inherent in the coarse-grained framework and the fact that oxDNA was primarily parameterized to capture the thermodynamics of double-strand formation. We note that both the all-atom MD and oxDNA simulations predict a similar fraction of molten base pairs (Figure 5.5); interestingly, local base pair melting does not significantly contribute to the temperature dependence of DNA twist in the MD simulations, but account for most of the change in the oxDNA calculations. As the magnitude of ΔTw(T) predicted by oxDNA is still smaller than the one observed experimentally and in atomistic simulations using the OL15 force field, one might expect this difference to be

due to microscopic properties of the twist potential for intact double-strand base pairs which are not represented explicitly in the coarse-grained framework.

Experimental values for ΔTw(T) provide a stringent test on DNA simulation protocols that will be useful in testing other coarse-graining schemes and atomistic force-fields in the future. While being a relatively subtle effect, even small changes in DNA twist can play important roles, for example for the pitch and curvature of higher-order DNA origami structures [22, 230, 231]. In addition, the delocalized and temporary base pair breaks revealed by the simulations might well serve as important nucleation points for proteins binding to DNA or for conformational transitions of the DNA helix.

5.5 Supplementary data

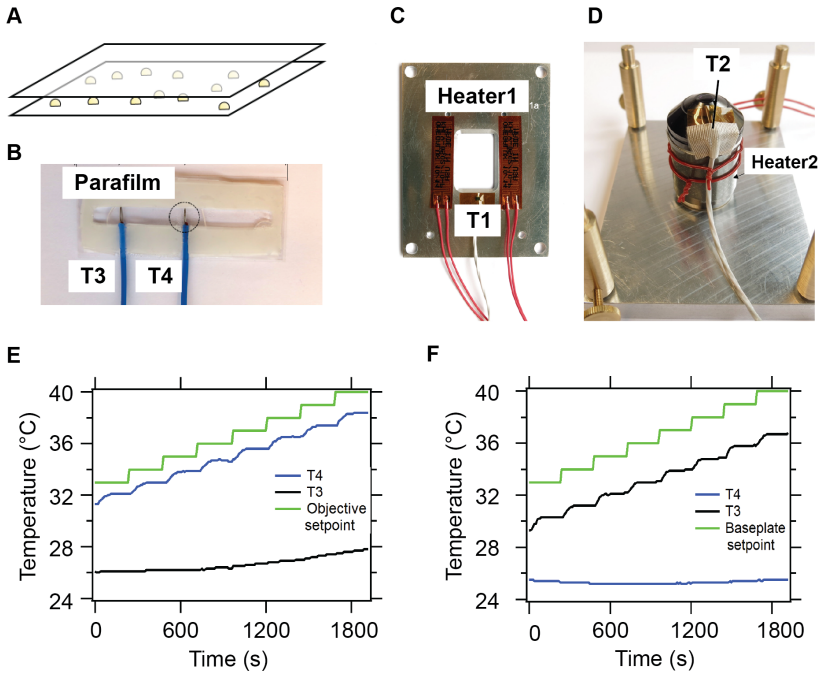

Figure 5.6: Temperature control hardware and measurements. (A) Schematic of surface attached plastic beads that are used as reference beads for the measurements in the MT setup to determine the expansion coefficient of the objective. (B) Image of the custom-made flow cell for temperature measurements. This flow cell uses several parafilm layers as spacers to facilitate insertion of thermocouple temperature sensors (labeled T3 and T4 in the figure). In contrast, our regular flow cells use a single layer of parafilm as spacer. T4 was adjusted such that it is directly above the heated objective; T3 is placed close to the flow cell edge. (C) Image of the two heating foils mounted onto the base plate of the flow cell holder; Thermocouple T1 serves as feedback sensor for this heating circuit. (D) Image of the heating foil mounted on the objective, with temperature sensor T2 that serves as feedback sensor for the objective heating circuit. (E) Temperature readings as a function of time during objective heating only. The green line shows the set temperature, whereas the blue line corresponds to the sensor T4 in the middle of the flow cell. The black line shows the measurements from sensor T3, located at the edge of the flow cell. The difference between set temperature and measured temperature within the FC is about 1°C. (F) Temperature readings as a function of time during base plate heating only. Same color code as in E. Sensor T4 is almost not affected by heating. The difference between set temperature and measured temperature within the FC is about 2°C. The offset between the measured temperatures in the flow cell (T3 and T4) and the set temperatures (green lines) is mainly due to the thickness of the flow cell and the fact that it has holes in the top glass cover slip. This offset is avoided when using the regular, thinner flow cell (see Supplementary Figure 5.7).

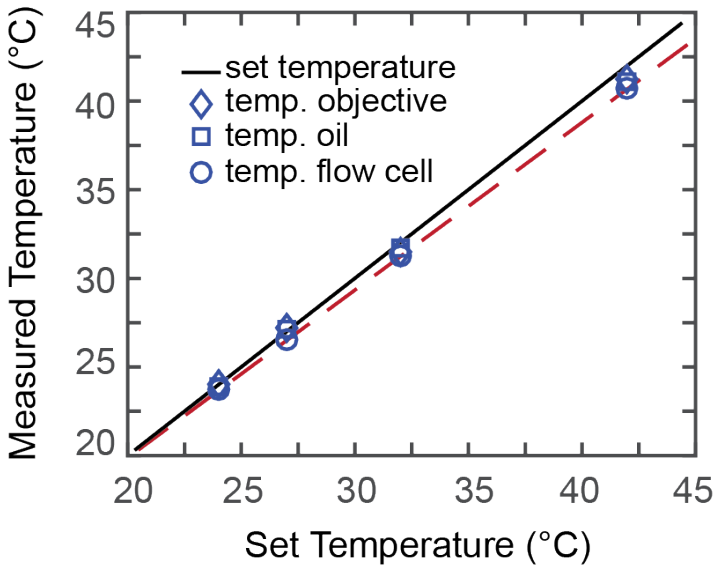

Figure 5.7: Temperature measurements for objective heating only. Measured temperature in the flow cell using the heated objective and regular flow cells with only a single parafilm layer spacer. In contrast to the system in Supplementary Figure 5.6, we used top glass cover slips with holes such that we can introduce the temperature sensor from the top directly into the solution. The black line indicates the set temperature (the set point at the PID controller). The temperature was measured separately at three positions: in the flow cell (directly at the position of the objective, blue circles), in the oil (between objective lens and flow cell, blue squares) and at the objective (close to the heating foil, blue triangles). The measured temperatures at the objective and in the immersion oil are in excellent agreement with the set point temperature. A slight temperature decrease in the flow cell is observed compared to the set point temperature at the PID. This deviation becomes larger for higher temperatures. Fitting a straight line to the recorded data of the measured temperature within the flow cell vs. set temperature (red, dashed line), we find a deviation of the temperature within the flow cell compared to the set temperature of 6% in °C. From this relation we can calculate which temperature to set in order to reach the wanted temperature within the flow cell. Overall, in the range presented in this work, we reach the temperatures within 0.5 °C.

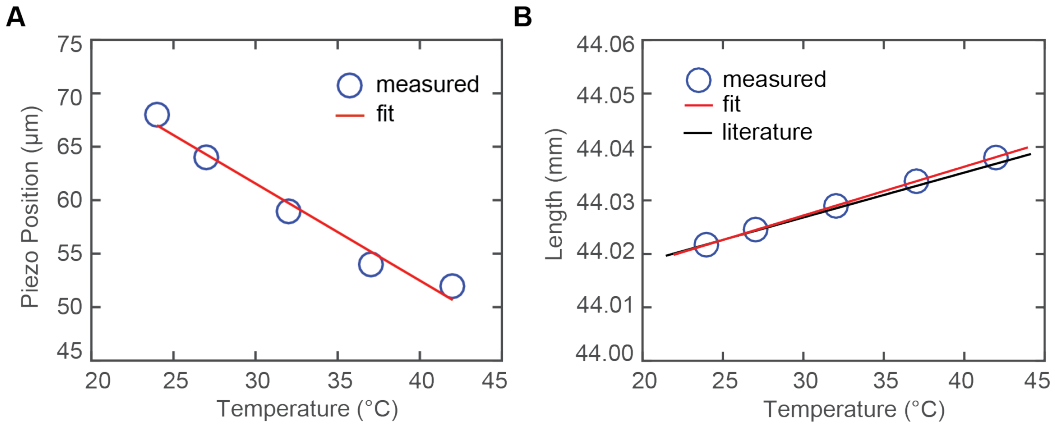

Figure 5.8: Thermal expansion of the objective. The flow cell is pushed upwards upon heating due to the expansion of the objective. This effect can be quantified by tracking the diffraction patterns of surface attached reference beads in the flow cell. (A) The objective is mounted on a piezo and the piezo position was adjusted to keep the diffraction patterns constant while increasing temperature. Shown as blue symbols is the absolute piezo position with increasing temperature. The red solid line is a linear fit to the observed data and its slope can be converted to an apparent expansion coefficient α of the objective, using its length L (L = 44 mm, vendor specification), ΔL and ΔT, by $\alpha = L \cdot \frac{\Delta L}{\Delta T}$. The data shown are for a 60x objective (Olympus, Oil Immersion objective, 60x magnification, NA 1.42,) and imply an expansion coefficient of $(2.06 \pm 0.02) \cdot 10^{-5}\ °C^{-1}$. Similar measurements using a 100x objective (Olympus, Oil Immersion Objective, 100x magnification, NA 1.25) found a thermal expansion coefficient of $(1.8 \pm 0.03) \cdot 10^{-5}\ °C^{-1}$, where the error comes from the error given with the line fit. Both values are very close to the literature value for brass α (brass) = $1.9 \cdot 10^{-5}\ °C^{-1}$ (http://www.engineeringtoolbox.com/linear-expansion-coefficients-d95.html). (B) The measured length of our objective at room temperature is approximately 44.02 mm. In B, we add the measured expansion (ΔL) to the overall length of the objective and plot the expansion over temperature. Co-plotted is the expansion of the objective using the literature value for the expansion of brass. Good agreement between both lines suggests that the expansion of the brass body of the objective is the dominant effect (compared to e.g. the expansion of the lens or the immersion oil).

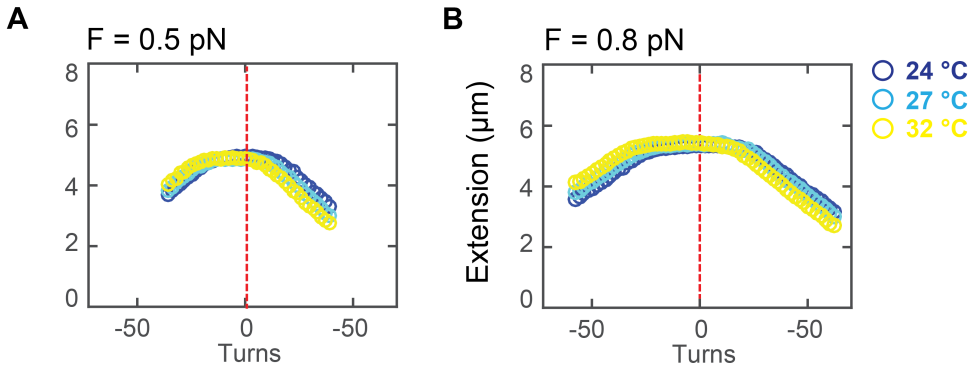

Figure 5.9: Rotation-extension curves for 20.6 kbp DNA. Examples of rotation-extension curves of 20.6 kbp DNA in PBS buffer measured at F = 0.5 and 0.8 pN at 24 °C, 27 °C and 32 °C. We find similar results for 20.6 kbp DNA as for the 7.9 kbp data shown in the main text: the rotation-extension curves shift to negative number of turns with increasing temperature.

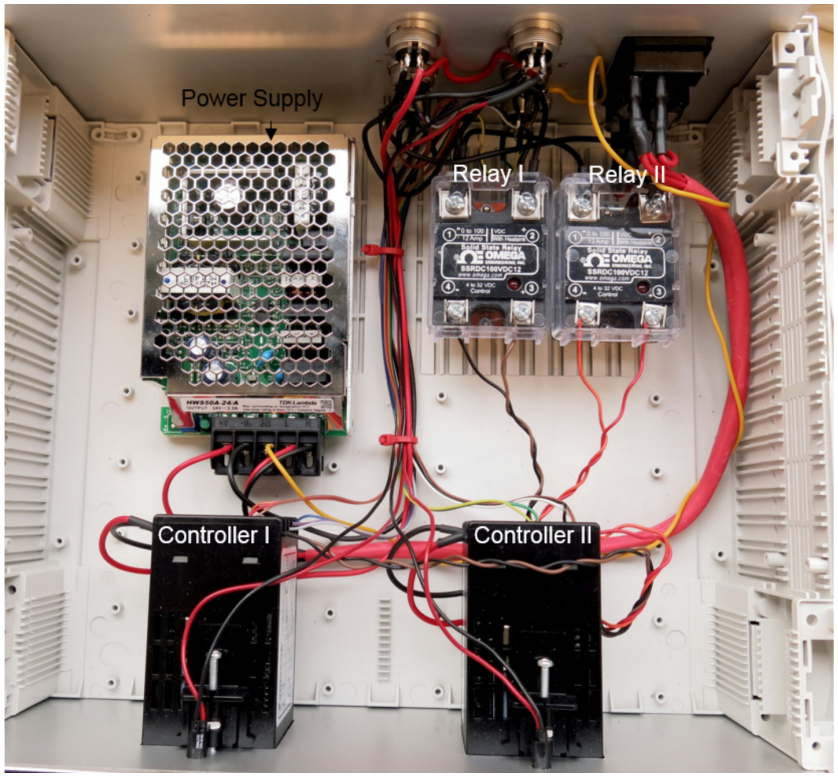

Figure 5.10: Custom made heated circuit for temperature control. The setup has two heating circuits, one for the objective and one for the flow cell heating. Each heating circuit is controlled by a single PID controller: objective heating with Controller 1 and baseplate heating with Controller 2 (as indicated in the figure). The power supply feeds both controllers that are connected to a relay and the temperature sensors.

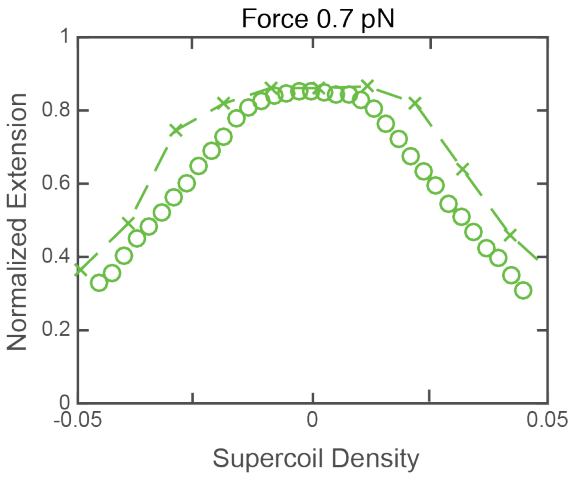

Figure 5.11: Rotation-extension data from MT measurements (circles) and oxDNA simluations (dashed line) at 0.7 pN and at 37°C. The overall shape of the curve as well as post-buckling slopes, are in good agreement. We note that differences in the precise location of the buckling superhelical density can be rationalized as a finite size effect [87, 171].

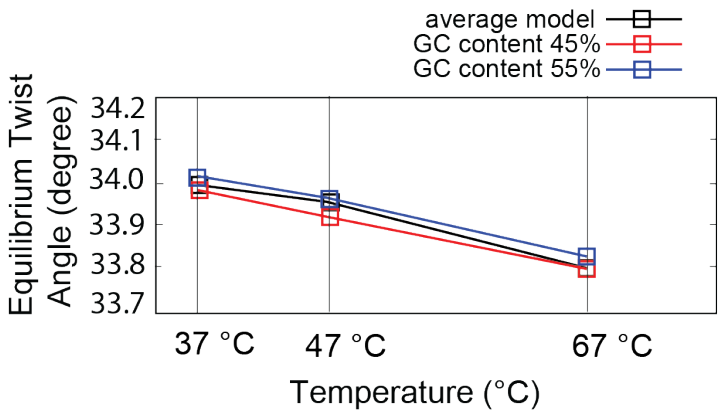

Figure 5.12: Control calculations with the sequence dependent parameterization of oxDNA. In order to check for the effect of varying GC content, we also performed simulations using the sequence-dependent parameterization of oxDNA on a 600-bp system with random sequences of a GC content of 45 and 55 percent. The value of the unwinding constant obtained from both these simulations is -6 degree/(°C·kbp), exhibiting no significant difference to the average base parametrization.

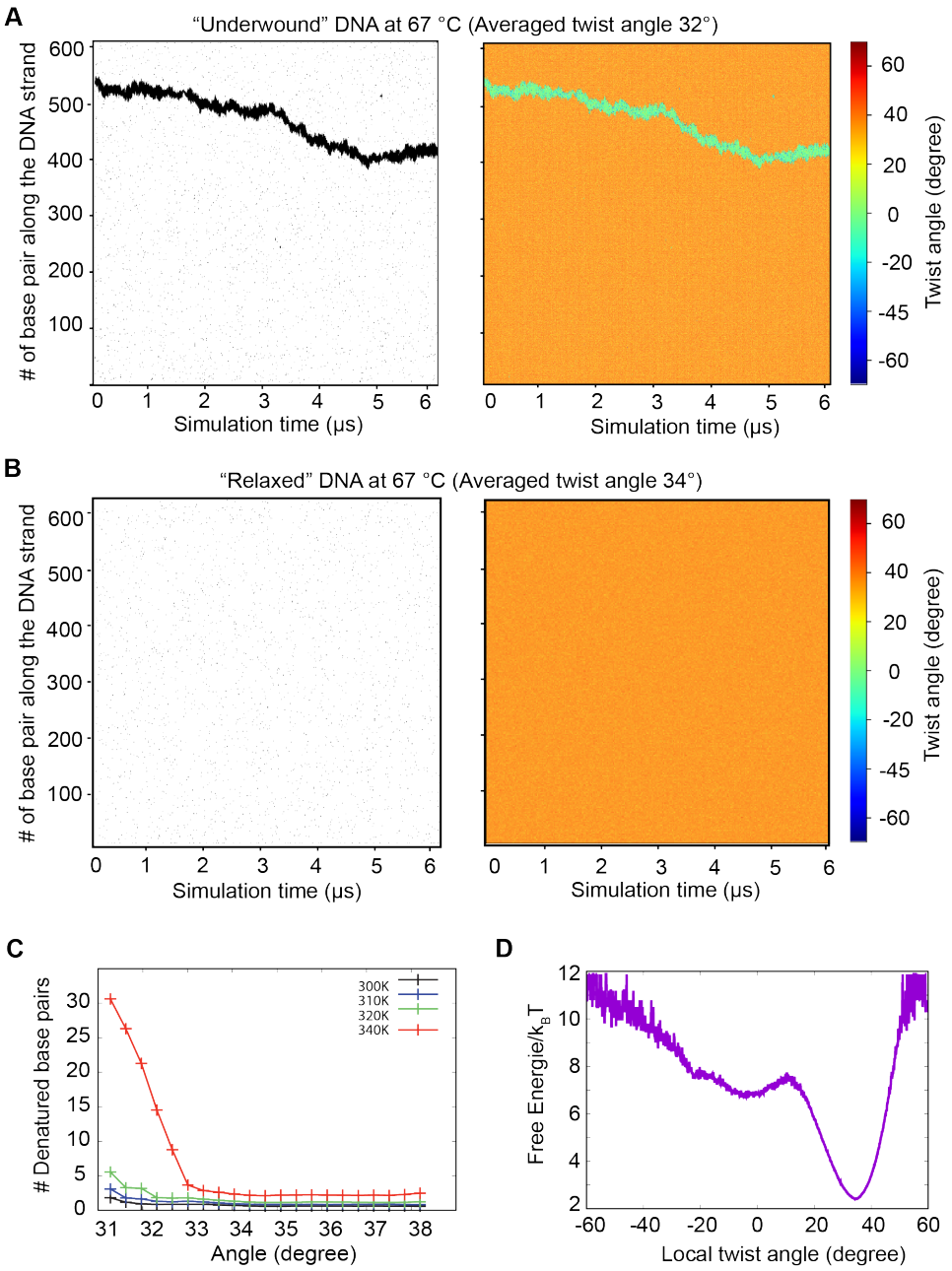

Figure 5.13: Analysis of DNA melting in oxDNA simulations. Simulations of a 600 bp DNA molecule using the base averaged parametrization of oxDNA. (A) Kymographs of base denaturation (left) and twist angle (right) for a system of average twist angel of 32.0°, corresponding to underwound DNA with a supercoiling density of σ = -0.059. Comparing the kymographs shows that the undertwist is localized, while the double- stranded region retains its relaxed-twist value. (B) Denaturation and twist angle kympgraph for a torsionally (almost) relaxed system at average twist angle of 34.0° (which is the equilibrium angle for DNA in the oxDNA parametrization). The data demonstrates short-lived and delocalized opening of double-strand base-pairs due to thermal fluctuations. (C) Number of denatured base pairs as a function of twist and temperature. (D) Free energy landscape of local twist angles for T = 67 °C and an average twist angle 32.0°, exhibiting a global minimum at ~34°, corresponding to the base paired helix and a secondary minimum at ~0°, corresponding to the denatured/broken base pairs.

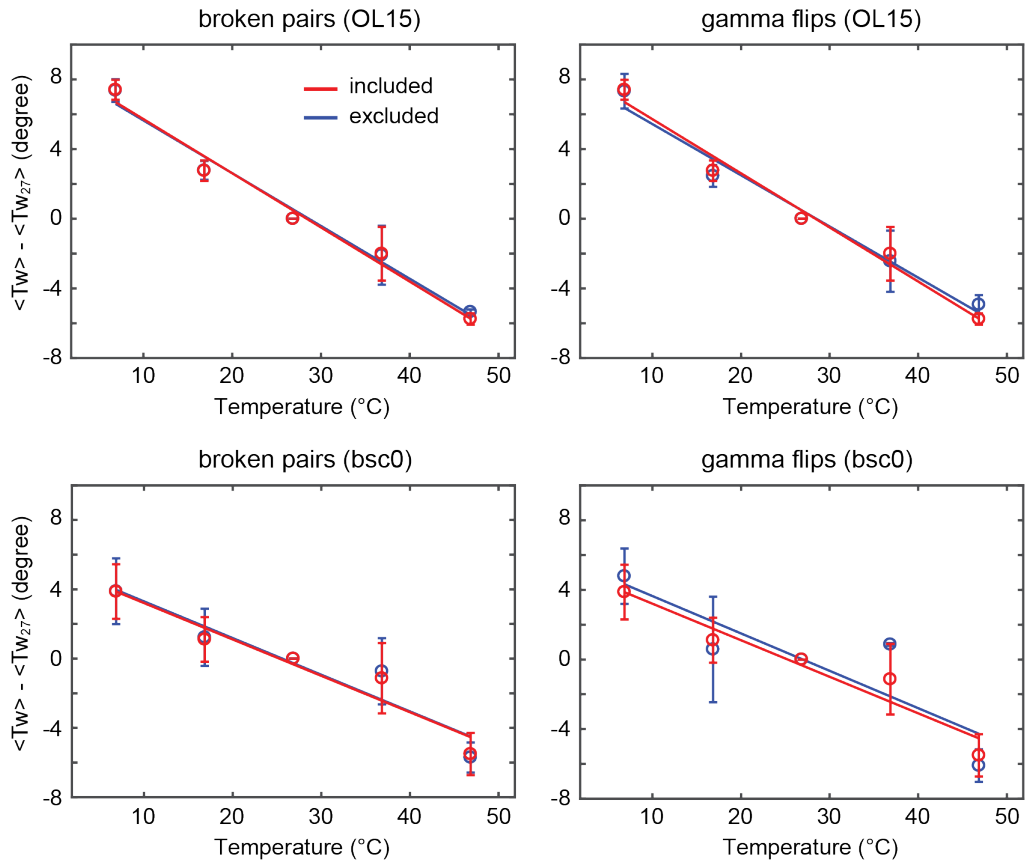

Figure 5.14: Effect of the broken base pairs (left) and the noncanonical flips of the backbone angle gamma (right) on the temperature dependent twist. Excluding snapshots with at least one base pair broken or with at least one gamma flipped (blue) does not change the twist temperature dependence in any significant way compared to the full MD data (red). Top figures illustrate MD simulations performed with the OL15 force field, whereas bottom figures illustrate simulations with the bsc0 force field.

Table 5.1: Collection of slopes for the change in helical twist obtained from MD data. Values for the OL15 and for the bsc0 Amber force fields are shown in degree/°C·kbp. Various twist definitions have been used. The end-to-end twist is based on the two end frames (Figure 5.2 in the main text). The mean-plane twist is invariant with respect to constant offset rotation of the end frames around their Z-axes. The axis-angle twist varies somewhat with the offset rotation and we show the interval of values for a series of rotations in 45 degree steps. Temperature slopes of end-to-end twists for each force field are mutually consistent irrespective of the definition and expose the differences between the force fields. The OL15 values agree quantitatively with the experiment, whereas the bsc0 values are lower. For completeness, results for twist defined as a sum of helical or local base pair step twists along the oligomer are also shown. The values span a wide range depending on the details of the definition.

	OL15 in degree/°C·kbp	**bsc0 in degree/°C·kbp**
End-to-end mean-plane	-11.1±0.3	-7.5±0.17
End-to-end axis-angle	-10.1±0.2 to -11.3±0.2	-6.3±0.15 to -8.0±0.19
Helical twist 3DNA	-7.6±0.2	-2.6±0.7
Helical twist Curves+	-10.5±0.1	-5.0±0.9
Local twist 3DNA	-12.2±0.1	-6.3±0.8
Local twist Curves+	-12.4±0.1	-6.4±0.8

Table 5.2: Values for the change of DNA twist with temperature ΔTw(T) from measurements and simulations. Early experiments using plasmid ligation and gel-electrophoresis derived values similar to the determined values within this work. The value obtained by Strick *et. al.* using MT is slightly higher. Everaers and co-workers published a value for the change in helical twist using MD simulations that is half the determined experimental values. MD calculations presented in this work using the OL15 force field refer values similar to the experimental data. Using the oxDNA frame work results in values half the experimental values. Further discussion is in the main text.

ΔTw(T) in degree/°C·kbp	**Method**	**Reference**
-10 to -11	Plasmid ligation and gel-electrophoresis, T = 60-100 °C	Depew and Wang, Ref. [204]
-10.5	Plasmid ligation and gel-electrophoresis, T = 35-83 °C	Duguet, Ref. [203]
-13.4	Magnetic tweezers, 48 kbp λ-DNA, T = 27-42 °C	Strick et al., Ref. [145]
-10.5 ± 0.6	Magnetic tweezers, 7.9 kbp DNA, T = 24-42 °C	This work
-11.5 ± 1.0	Magnetic tweezers, 20.6 kbp DNA, T = 24-42 °C	This work
-6.5	MD simulations	Everaers and co-workers, Ref. [205]
-10.8 ± 0.1	MD simulations, mean-plane definition, OL15, T = 7-47 °C	This work
-6.4 ± 0.2	oxDNA simulations, T = 27-67 °C	This work

Chapter 6

The Effect of Temperature on the Torsional Stiffness of DNA

Abstract

This chapter discusses preliminary extension- and torque-rotation data recorded at 20°C and 40°C using multiplexed magnetic torque tweezers in combination with the heating objective described in the previous chapter. FPA experiments report a decrease in the torsional stiffness > 50% going from 7 to 37°C, whereas the data presented here finds a much smaller decrease (about 10%). Predictions of the TWLC and aTWLC model, discussed in Chapter 4, find a decrease of the torsional stiffness of 5% going from 20°C to 40°C. oxDNA and all-atom MD simulations as described in Chapter 5, find a decrease of about 10% going from 7 to even higher temperatures (> 40°C). Overall, direct torque measurements and molecular dynamic simulations find a decrease between 5 and 10%. The open question is, to what extend the intrinsic torsional stiffness is affected due to changes in temperature, or whether effects on the effective torsional stiffness are mainly caused by a decrease in the bending stiffness.

6.1 Introduction

Biological organisms adapt to physiological conditions, like temperature, pH and salt concentrations. Small changes within these parameters can change the overall activity or functionality of molecules. A good example is the TATA-binding protein (TBP), which is a protein involved in the read-out of DNA. It binds to a specific sequence of DNA, referred to as TATA-box, and initiates the process of transcription. Studying the binding affinity of TBP to DNA, results in enhanced activity at temperatures that are in agreement with their thermophilic growth conditions [232].

The change in helical twist of DNA with temperature is discussed in the previous chapter and shows that there is a small unwinding effect. This effect is mainly due to a change in conformation of the DNA's backbone. Also, it is known that the bending persistence length depends on temperature and decreases upon the increase of temperature [233, 234]. A similar effect to the increase of salt concentration in solution. A smaller bending persistence length

effects buckling transitions and the formation of DNA plectonemes. Thus, implying that a change in temperature will also effect the torsional stiffness of DNA. However, it is unknown whether this affects also the intrinsic torsional stiffness of DNA, or only the effective torsional stiffness at stretching forces < 3 pN, where a decrease in C_{eff} could be explained by a pure change in bending stiffness. Fluorescence polarization anisotropy (FPA) measurements by Barone *et al.* [235] suggest that the torsional stiffness decreases by 50% going from 7 to 37°C. Direct measurements of molecular torque at comparable temperatures have not been done yet. Preliminary data, presented in this work and measured with the temperature controlled multiplexed MTT instrument, suggest that the effect of temperature is smaller than suggested by Barone *et al.* [235] and in good agreement with all-atom and coarse-grained simulations, which predict a decrease on C_{eff} smaller than 10%.

6.2 Materials and methods

Measurements within this chapter were performed using measurement protocols described previously. Refer to Chapter 2 for instrument details, preparation of the flow cell, the DNA construct, magnetic beads and tether selection. Multiplexed extension- and torque-rotation measurements are explained in Chapter 3. Measurements at 40°C were performed using the heated objective as explained in Chapter 5 and measurements at 20°C were performed using the air-conditioning of the laboratory only. All measurements were performed using PBS buffer, as stated previously.

Preliminary data on temperature dependent torque-rotation measurements, suggest that if there is an effect of temperature on the torsional stiffness of DNA within this temperature range, it is small. The subtler the effect the more care must be taken during a measurement and in the sub-sequent analysis. Therefore, the averaging algorithm described in Chapter 3 was adapted, including smoothing of the data and a different, but similar approach to determine the buckling point as well as the buckling torque. Symmetric and asymmetric extension-rotation data need to be treated with different analysis protocols, see below.

6.2.1 Data averaging: Symmetric extension-rotation data

Determining Lk0

A Gaussian is fitted to the extension-rotation data of DNA (Figure 6.1(1)) to determine Lk0, similar to Chapter 5. Both, the extension and torque-rotation data is then shifted along the turns axis by -Lk0. The Gaussian fit is very robust, such that the fit converges for every curve, resulting in a very accurate determination of Lk0.

Extension adjustment

From the theoretical prediction of the WLC, one can estimate the relative extension, i.e. the measured tether extension relative to the contour length of the molecule, at Lk0 and at a given force. The relative length of the molecule at 0.6 pN and 0.9 pN is 80% and 84% of its contour length, respectively. The contour length, Lc, is calculated using the known number of base pairs (here 7900) and the base step parameter (0.34 nm/turn) and is about 2700 nm. The

deviation of the molecules extension at Lk0 from the calculated value is further used to shift the extension-rotation data along the extension-axis (Figure 6.1(2)).

Determining the buckling point and post-buckling slope

Three lines are fitted to the corrected extension-rotation curves: Two, in the post-buckling regime, i.e. where the molecules extension decreases upon inducing twist, and one to the pre-buckling region, i.e where the molecular's extension stays almost constant upon the application of turns. Assuming that the extension stays constant upon over- and underwinding in the pre-buckling regime, the slope in the line fit is kept fixed to zero, resulting in a horizontal fit to the data in the pre-buckling region. Performing line fits, in general, asks to pre-define fitting regions.

The intersection of the post-buckling line fit for positive turns with the line fit in the pre-buckling area is defined as the buckling point for positive turns. Whereas the intersection of the slope of the post-buckling area for negative turns is defined as buckling point for negative turns (Figure 6.1(2)). Whether one defines the closes measured value as buckling point (Figure 6.1(2), large diamonds) or the exact value on the turn axis of the intersection of the lines (large squares), is in good agreement. For the sub-sequent analysis, the intersection of the lines is defined as buckling point.

Define zero torque at zero turns

The corresponding torque-rotation data is shifted along the turns axis by -Lk0 using the value extracted from the extension-rotation data. A line fit to the pre-buckling region, i.e. the region where the molecular torque increases, is performed and the torque value at zero turns is determined. Each curve is then shifted along the torque-axis using the deviation of torque at zero turns from zero (Figure 6.1(3)). Taking into account that at low forces (< 1 pN) positive and negative buckling occurs symmetric around zero turns, the buckling torque for positive and negative turns should be symmetric around zero torque. If necessary, the data is shifted along the torque axis to fulfill this criterion.

Determining the torsional stiffness and buckling torque

The previously performed line fit (Figure 6.1(4), black line) in the pre-buckling region is used to calculate the torsional stiffness of every single DNA molecule using Eq. 3.3 in Chapter 3. The temperature is hereby already adjusted to the conditions of the measurement. The region for the fit is pre-defined and varies for different forces. It is from -6 to 6 turns and -8 to 8 turns for 0.6 and 0.9 pN, respectively. The buckling torque, positive and negative, is defined as the torque value at the buckling point. To ensure that the buckling torque lies not in the pre-buckling region but further in the post-buckling area, the next value, either in positive turn direction for positive buckling, or in negative direction for negative buckling, is defined as buckling torque (Figure 6.1(4), black crosses).

Smoothing and binning

The data is now collected in arrays that are independent of the measured molecule (Figure 6.1(5,6), black symbols in the background). Extreme outliers in the extension- and torque-

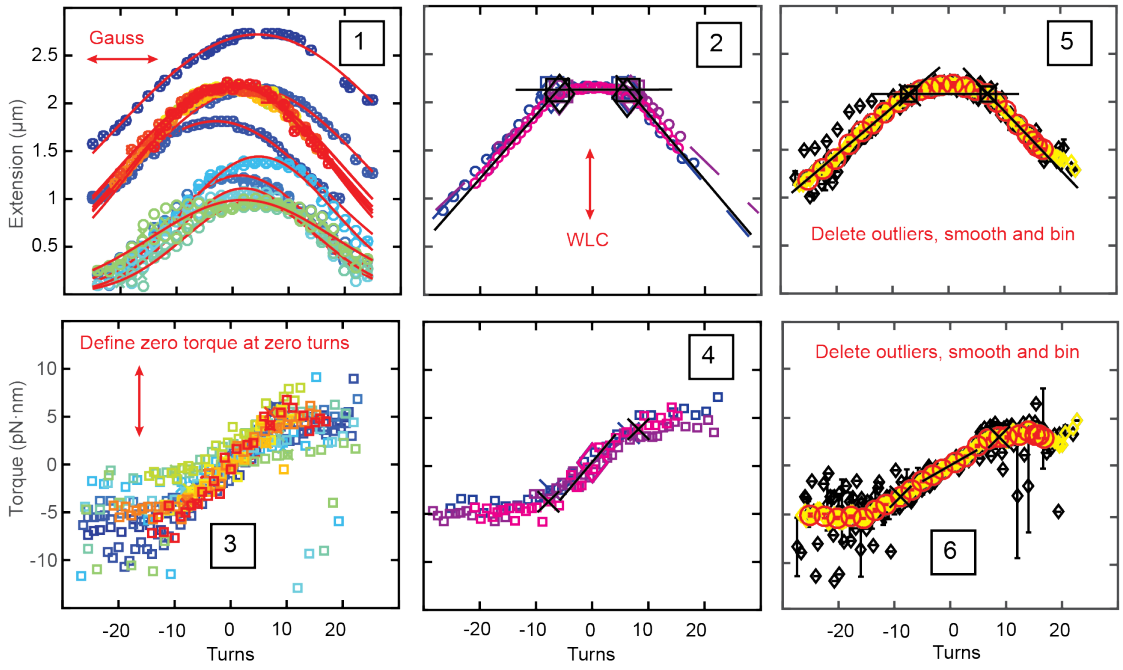

Figure 6.1: Data averaging for symmetric extension-rotation and torque-rotation data. (1) Illustration of individual extension-rotation data measured at the same temperature (20°C) and the same force (0.6 pN). Curves are shifted along the turns axis, by determining Lk0 using a Gaussian fit. (2) The extension of the molecule is adjusted using the WLC approximation. (3) A slope fit is performed on every single torque-rotation curve, to determine zero torque along the turns axis. Data is shifted, such that zero torque corresponds to zero turns (4). (5,6) Smoothing of the data reduces the error. Averaged extension- and torque-rotation data are obtained using a binning of 2 turns along the turn axis. The torsional stiffness, buckling point, post-buckling slope and the buckling torque are extracted from each individual molecule and finally also from the averaged curve for comparison. Shown is data at 0.6 pN and 20°C in PBS buffer, mean and SEM.

rotation data are removed by defining an upper and lower limit for both data sets. If the extension is larger than 3 or less than 0.5 μm (or if torque values are larger than 30 pN·nm), data points are ignored in the subsequent analysis. Smoothing is performed by a moving window average with a window of 5 data points (Figure 6.1(5,6), yellow). To result in averaged curves a binning (MATLAB, "histcount" function with predefined "edges") of two along the turns axis, is performed and the mean and standard error of the mean in each bin is computed (Figure 6.1(5,6), red). To further reduce errors, every data point that deviates by two sigma from the mean is not taken into account.

6.2.2 Data averaging: Asymmetric extension-rotation data

Determining the mean buckling point

Due to the asymmetry of the extension-rotation data at 3.5 pN, the location of Lk0 cannot be defined as previously described. In order to properly overlap the different curves they are shifted to the mean buckling point along the turns axis. Therefore two slopes are fitted to pre-defined, i.e. manually defined, regions: One to the post-buckling regime for positive turns, and one to the region where torque induced melting occurs (Figure 6.2(1)). The intersection

of the two lines in defined as buckling point. The mean of all buckling points is derived and each individual curve is shifted along the turns axis, such that its buckling point results on the mean value (Figure 6.2(2)).

Extension adjustment

To overlap the data along the extension axis, the deviation of the measured value at zero turns to the WLC approximation (92% of Lc, see above) is determined and the extension is adjusted (Figure 6.2(2)).

Define zero torque at zero turns

The corresponding torque-rotation data is shifted along the turns axis similar to the extension-rotation data. Additionally, the torque value at zero turns is determined using a line fit in the pre-buckling region, where the area of the fit needs to be pre-defined. The data is shifted along the torque axis, such that zero turns results in zero torque (Figure 6.2(3)).

Determining the torsional stiffness and buckling torque

Using the line fit in the pre-buckling region (from -10 to 20 turns at 3.5 pN) to the torque-rotation data, the torsional stiffness is defined taking the different temperatures into account. The buckling torque is defined similarly to the symmetric analysis: The next torque value along positive turns to the buckling point, is defined as buckling torque (Figure 6.2(4)).

Smoothing and binning

Extension- and torque-rotation data for all beads are collected (Figure 6.2(5,6), black) and smoothed by five turns (Figure 6.2(5,6), yellow). An upper and lower limit (extension values larger than 3 and smaller than 0.5 micrometer and torque values larger than 60 and smaller than -30) is defined to ignore extreme outliers in the data before smoothing. An additional binning on five turns is performed (see above for details). In addition, an algorithm to delete outliers that deviate by two sigma from the mean value is used. Shown is the mean and standard error of the mean for all molecules (Figure 6.2(5,6), red). Buckling points, post-buckling slopes, the torsional stiffness and the buckling torque is extracted from each individual curve and from the averaged curves.

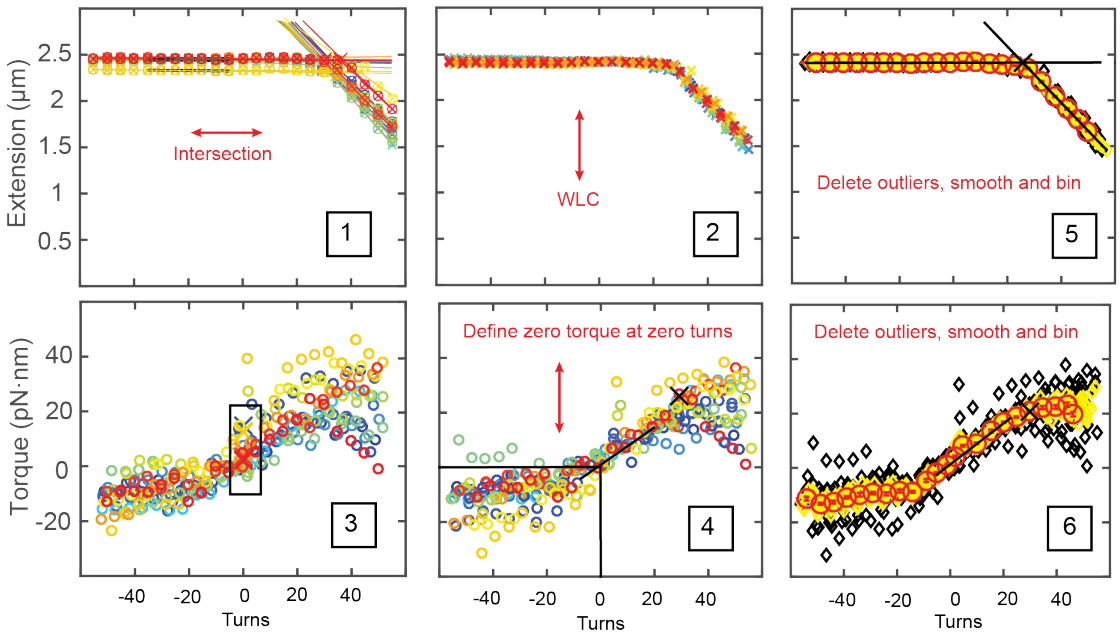

Figure 6.2: Data averaging for asymmetric extension-rotation and torque-rotation data. Two slopes are fitted to the extension-rotation data. The intersection is defined as buckling point and the slope of the fit to the post-buckling region for positive turns is further analyzed (1). The curves are shifted to the mean of the buckling points along the turns axis and according to the WLC along the extension axis (2). A line is fitted to the pre-buckling regime to determine the torque value at zero turns (3). Torque data is shifted along the torque axis such that zero torque corresponds to zero turns (4). (5,6) Data for all beads are collected (black diamonds). The data is smoothed (yellow), outliers are removed and data is averaged using bins of 5 turns (red symbols). The torsional stiffness, buckling point, post-buckling slope and the buckling torque is extracted from each individual and finally also from the averaged curve for comparison. Shown is data at 3.5 pN and 20°C in PBS buffer, mean and SEM.

6.3 Results and discussion

6.3.1 Extension-rotation and torque-rotation measurements

Shown in Figure 6.3 are preliminary averaged extension- and torque-rotation traces of DNA, measured at 0.6, 0.9 and 3.5 pN and at 20°C (blue) and 40°C (red). The number of molecules for the averaged curves is 14 (20°C) and 9 (40°C) at 0.6 pN, 7 (20°C) and 9 (40°C) at 0.9 pN and 14 (20°C) and 8 (40°C) at 3.5 pN. Averaging extension-rotation data is very robust, also for a small number of measured molecules. Averaged torque measurements, however, require a larger number of molecules (> 10 molecules) as the error on torque, in particular in the post-buckling regime, is about 10% higher compared to that on extension measurements (value derived by comparing the error from the extension- with the corresponding torque-rotation data).

Here, I present averaged extension- and torque-rotation curves using a small number of measured molecules and find that the averaging algorithm results in mean values, with small standard errors of the mean. Note, that the mechanical properties, such as the buckling points, post-buckling slopes and the torsional stiffness, were extracted from each curve individually. I finally computed the mean and standard error of the mean over all molecules. The reason is that there is a risk that averaged curves underestimate buckling points and in particular

the torsional stiffness of DNA, see Supplementary Figure 6.7. However, this error is generally reduced when taking the average over a larger number of molecules using multiplexed MTT.

Pre-buckling

Pre-buckling, is defined as the region where overwinding by additional turns increases molecular torque, whereas the molecular's extension stays nearly constant (indicated as grey shaded area in Figure 6.3). The extension data in the pre-buckling regime are almost identical at 20°C and 40°C for all measured forces. All curves at 20°C and 40°C were shifted along the turn axis, here the supercoil density axis, such that Lk0 is at zero turns, thus resulting in centered curves for 0.6 and 0.9 pN. The shift in helical twist (ΔTw) with temperature (see Chapter 5) is not shown here, as conventional MT as used in Chapter 5 are much more suited to study ΔTw than magnetic torque tweezers used in this study.

Interesting in this case is the corresponding torque behavior from which the torsional stiffness of DNA is extracted. The averaged curves indicate that there is almost no difference between the data at different temperatures and forces. A more quantitative analysis and discussion on the torsional stiffness follows.

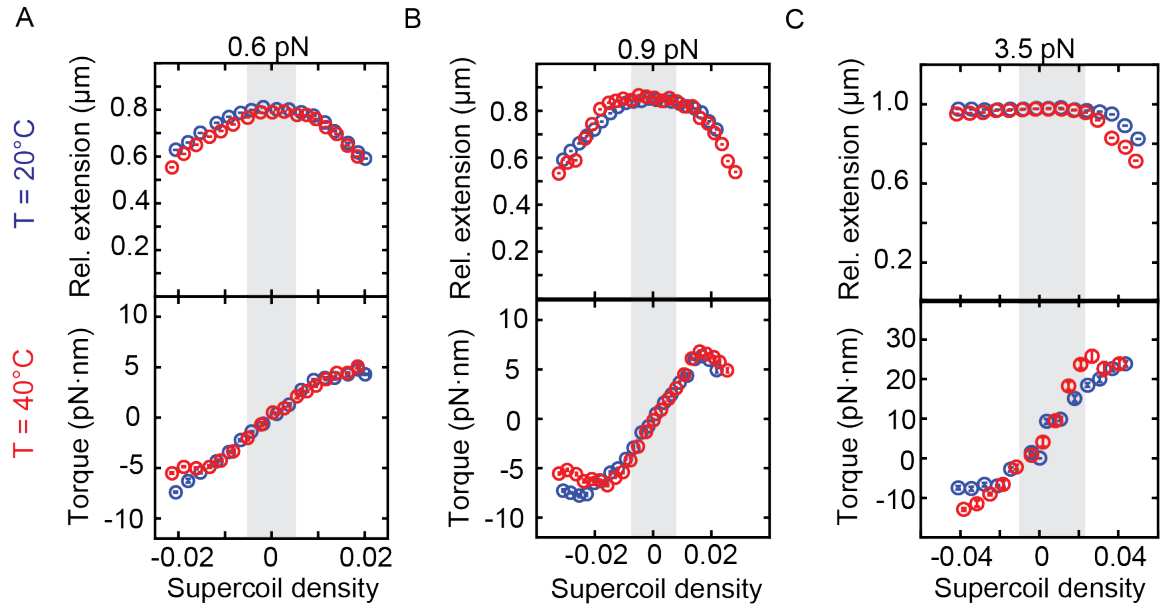

Figure 6.3: Averaged extension- and torque-rotation data at 20 (blue) and 40°C (red) and at 0.6, 0.9 and 3.5 pN. Shown here is the relative extension (top) and torque (bottom) against the supercoil density of the molecule. The shaded grey area in the background illustrates the area used for the line fit to the torque-rotation data in the pre-buckling region to determine the torsional stiffness.

At the buckling transition

At the buckling transition, further torsional stress within the molecular tether is released in the formation of plectonemes upon over- or underwinding. This is observed in a decrease in the extension. At the buckling transition, the molecular torque stays constant, no further increase is observed. For stretching forces larger 1 pN upon underwinding, however, torsional

stress is released through melting of base pairs, which does not lead to a decrease in the extension, but to a saturation of molecular torque at -10 pN·nm [34, 46, 90]. From the averaged extension-rotation data it seems that buckling occurs earlier, i.e. at a smaller number of applied turns, for measurements performed at 40°C than at 20°C. A more quantitative analysis follows. Note, that at 3.5 pN the shift in the buckling point for 40°C illustrated here, does not correct for the known shift of ΔTw, discussed in Chapter 5.

Post-buckling

With every additional turn of the magnet after buckling, further plectonemes are formed, leading to a constant decrease in the extension in the post-buckling regime. The slopes are a quantitative description of the size of the plectonemes formed, which in turn, strongly depends on electrostatics. The corresponding torque behavior, however, is the part of the measurement with the largest error, thus making the analysis extremely hard. Post-buckling, the magnetic bead gets in close proximity to the surface, resulting in interactions that strongly disturb the measurement signal. Improvements in the measurement and analysis protocol are in preparation. Further quantification and discussion on the post-buckling slopes and the corresponding buckling torque are in the next section.

6.3.2 Change in helical twist, buckling points, post-buckling slopes, and buckling torque

The previous section discussed briefly the behavior of DNA pre-buckling, post-buckling and at the buckling transition. To further quantify the effect of temperature on mechanical properties such as buckling points, post-buckling slopes and buckling torque, each individual curve was treated with the protocol explained in materials and methods of this chapter.

Change in helical twist with temperature

Studying the change in helical twist (ΔTw) of DNA with temperature is described in Chapter 5. The unwinding effect, ΔTw, is -11 degree/(°C·kbp), independent of force (at least for the forces tested, all < 1 pN). Studying ΔTw for higher forces, i.e. where extension-rotation curves are asymmetric, has not been done yet. The reason is that there is no proper way to determine Lk0 at stretching forces that result in asymmetric extension-rotation behavior. Assuming that the unwinding effect is independent of force (also for forces > 1 pN) one can calculate the expected shift of the extension data to negative number of turns, where ΔTw is in units of turns and ΔTw' in supercoil density:

$$\Delta Tw = \frac{\left[-11\frac{degree}{°C\cdot kbp}\cdot 20°C\cdot 7.9\,kbp\right]}{360\frac{degree}{turn}} \approx -4.8\,turns \tag{6.1}$$

$$\Delta Tw' = -4.8\,turns\cdot\frac{10.5\frac{bp}{turn}}{7900\,bp} = -0.0064 \tag{6.2}$$

Each experimentally derived buckling point is thus shifted by +0.0064, assuming that this shift occurs only due to the change of Lk0 with increasing temperature.

Buckling Points

Buckling points are extracted from extension-rotation data using the intersection of the line fits. Shown in Figure 6.4A is data for positive buckling points, i.e. buckling at a positive number of turns, at 20°C (blue symbols) and at 40°C (red symbols). Note, that the extension-rotation data at 3.5 pN were first corrected for the known change in helical twist with temperature as explained in the previous part. Co-plotted are the values determined at room temperature and at "low salt" from Chapter 3. Measurements in this chapter were performed at 150 mM NaCl, slightly higher than 100 mM NaCl used in "low salt". However, the effect of salt is small and discussed in Chapter 3, therefore one would expect similar results for the blue and black symbols. The buckling points from this dataset are lower as previously measured; however, they still give a reasonable comparison between low (20°C) and high temperatures (40°C), preliminary. Values for the buckling points are 10% smaller at 40°C than at 20°C for all measured forces. This is understood as the bending persistence length, decreases with increasing temperatures [233, 234]. Beyond the buckling point, torsional stress is released in the formation of plectonemes. If the molecule is more flexible, i.e. a smaller bending persistence length, bending stress within the plectoneme is reduced, allowing the molecule to buckle at a lower supercoil density. Similar to the study on the salt dependence (see Chapter 3), the Marko model [91] is co-plotted to the dataset using 50 nm, 110 nm, 24 nm, and 20°C (blue) and 45 nm, 110 nm, 22 nm and 40°C as fixed parameters for A, C, P and T, respectively. Note, the reduction of P with increasing temperature, is in analogy to the reduction of P with increasing salt concentration, which also lowers A (see Chapter 3). The experimental data presented here are in qualitative, however, not in quantitative agreement with the model (reduced χ^2 = 50 for 20°C and reduced χ^2 = 46 for 40°C).

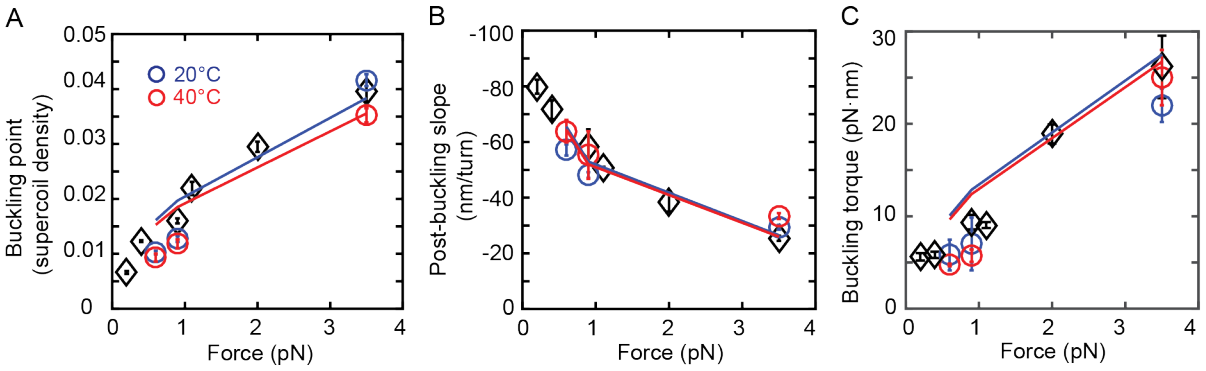

Figure 6.4: Buckling points (A), post-buckling slopes (B) and buckling torque (C) at 20°C and 40°C. Blue and red symbols illustrate the mean and SEM of recorded data at 20°C and 40°C, respectively. Black symbols indicate data from Chapter 3 taken at "low salt" and at room temperature, thus, comparable to the data here, taken at 20°C and in PBS buffer (blue circles). Co-plotted is the Marko model with fixed parameters A (50 nm at 20°C and 45 nm at 40°C), C (110 nm) and P (24 nm at 20°C and 22 nm at 40°C). The blue line indicates the model using T = 20°C and red using T = 40°C.

Post-buckling slopes

Illustrated in Figure 6.4B are the determined post-buckling slopes for positive turns at each force and for both temperatures. Note, that the post-buckling slopes for positive turns are negative and that the absolute value is plotted and discussed in this work. Previous measurements suggest that post-buckling slopes decrease with increasing temperature for positive torques [103], which is also in agreement with the Marko model (see Figure 6.4B, solid lines). This effect is understood by a decreased bending persistence length, which allows smaller sized plectonemes. Here, the experimental data are in much better agreement with the model (reduced χ^2 = 17 for 20°C and reduced χ^2 = 15 for 40°C).

Buckling Torque

The buckling torque is extracted from torque-rotation response, whereas slopes and buckling points are taken from extension-rotation data. In general, the error on torque-rotation data is about 10% larger, which makes the analyses of buckling torques and the torsional stiffness more difficult compared to others. The presented data of the buckling torque (Figure 6.4C, red and blue circles) are slightly lower compared to previous measurements (black diamonds), but still in reasonable agreement. The Marko model (solid lines) predicts the buckling torques to decrease at higher temperatures which is in agreement with experimental data, at least for forces < 1 pN. This can be understood by the shift of the buckling points to a lower number of turns, i.e. a smaller bending persistence lengths at higher temperatures. If the buckling point shifts to a smaller number of turns with increased temperature and the torsional stiffness stays constant, the buckling torque has to decrease. The same holds if the torsional stiffness decreases with temperature (which seems to be the case, see next section for a discussion on the torsional stiffness of DNA). Only in the case that the torsional stiffness increases, buckling torque could stay constant or increase for higher temperatures.

6.3.3 The torsional stiffness of DNA

The torsional stiffness of DNA increases with stretching force. At large enough forces, the intrinsic torsional stiffness equals the effective torsional stiffness, as bending deformations are suppressed (see Chapter 4). Figure 6.5 shows data for the effective torsional stiffness of DNA, measured at 20°C (blue filled circles) and 40°C (red filled circles). Co-plotted are torsional stiffness values from Chapter 3 taken at room temperature (black diamonds) and results from coarse-grained simulations for the TWLC and aTWLC model at both temperatures, as described in Chapter 4. Both models predict a decrease in C_{eff} with increasing temperature on average larger than 5%.

At 0.6 pN the measured data at both temperatures is almost identical. However, the blue data point is slightly lower than previous results of C_{eff} at similar conditions (black diamonds). The effective torsional stiffness measured at 3.5 pN and at high temperature (40°C) has a very large SEM and lies above the value at 20°C. At 0.9 pN the effective torsional stiffness at 40°C is about 15% smaller than at 20°C, which is in quantitative agreement as predict by the TWLC and the aTWLC model.

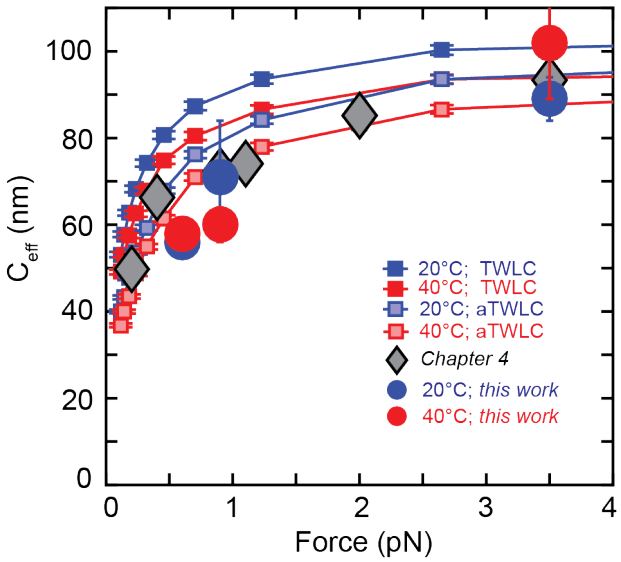

Figure 6.5: The torsional stiffness of DNA for varying forces and temperatures. Shown are predictions of the TWLC and the aTWLC at 20°C (blue squares) and 40°C (red squares) using A = 45 nm and C = 110 nm for the TWLC and ϵ = 10 nm and G = 40 nm for the aTWLC model. Co-plotted is data from Chapter 3 taken at room temperature and at "low salt" (black diamonds). The data taken from this work is illustrated by large filled circles, mean and SEM.

Further measurements on all forces and temperatures, will help to properly resolve the temperature dependence of the effective torsional stiffness of DNA. In particular the data collected at 0.9 pN is promising to detect the subtle decrease in C_{eff}.

Moreover, all-atom and coarse-grained simulations find that the torsional stiffness of DNA decreases for increasing temperatures. Figure 6.6 gives an overview on predictions on the decrease of the torsional stiffness with temperature. Shown is the data measured in this work with MT at 0.9 pN and at 20°C and 40°C, which cause a decrease of 15%. Coarse-grained

simulations of DNA, as explained in Chapter 4, find a decrease of 7% and 6% for the TWLC and the aTWLC model, respectively, going from 20°C to 40°C at 0.7 pN. oxDNA simulations (as described in Chapter 5) at 0.7 pN stretching force and in a temperature range from 27°C to 67°C predict a similar decrease in the effective torsional stiffness (about 10%), as well as all-atom simulations on a 33 base pair DNA construct (as described in Chapter 5) with 11% going from 7°C to 47°C.

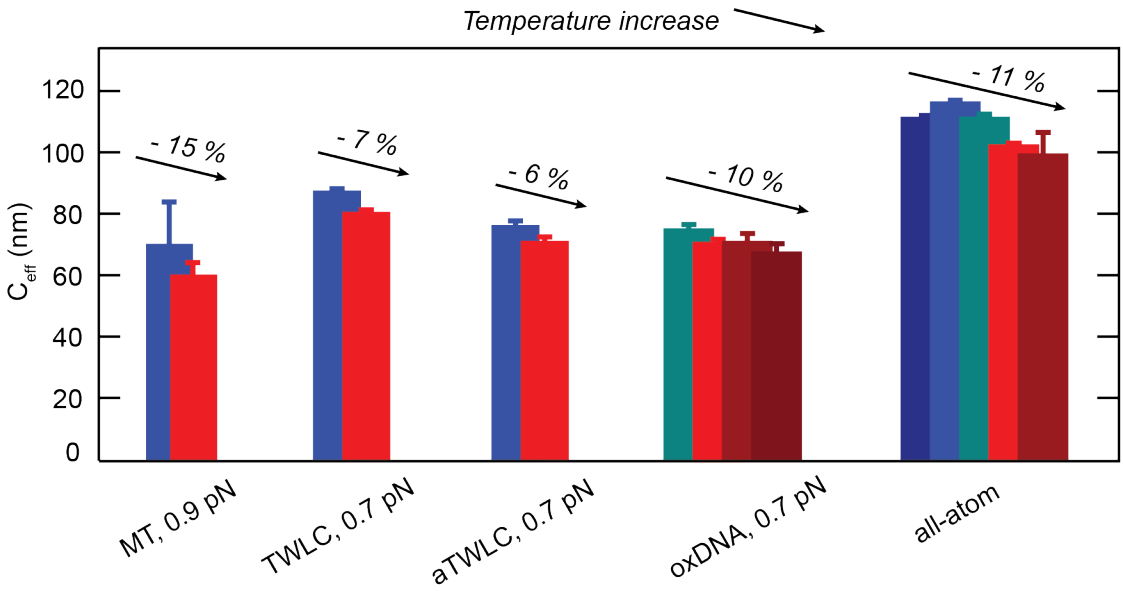

Figure 6.6: Predictions for the torsional stiffness of DNA using MT and various simulation modalities. From left to right: MT results (this work) at 0.9 pN at 20°C (blue) and at 40°C (red). Predictions for C_{eff} using the TWLC at 20°C (blue) and at 40°C (red) and at 0.7 pN. Results for the aTWLC model at 0.7 pN and at 20°C (blue) and at 40°C (red). oxDNA at 0.7 pN and at 27°C, 37°C, 47°C and 67°C (blue to dark red colors). All-atom simulations at 7°C, 17°C, 27°C, 37°C to 47°C (blue to dark red colors). All find that C_{eff} decreases upon the increase of temperature (indicated by an arrow, on average about 10%).

All measurement modalities show that the torsional stiffness decreases upon an increase in temperature. We find that the decrease going from 20°C to 40°C is between 5% and 15%, thus, smaller than previously reported [235]. Overall, all simulations result in a decrease of 5% for a $\Delta T = 20°C$, which is remarkably consistent. The finding that the buckling points shift to a smaller supercoil density implies that the torsional stiffness of DNA is affected by temperature. We know that DNA unwinds upon the addition of temperature by -11 degree/(°C·kbp) (see Chapter 5), which changes the overall structure. The backbone, with its helical nature, is one of the stabilizing factors in the molecule. However, the data presented here, lacks high statistics, therefore it is still unknown whether higher temperatures effect the intrinsic torsional stiffness or whether the decrease is only due to a softening in the bending stiffness.

6.4 Conclusion

Four mechanical parameters of DNA can be studied using magnetic torque-tweezers, namely the buckling point, the post-buckling slope, the buckling torque and the torsional stiffness. The first two are extracted from extension-rotation and the last two, from torque-rotation measurements. Predictions of the Marko model suggest that buckling points shift to a smaller number of applied turns for higher temperatures, which is in agreement with the data presented in this work. This result is in agreement with previous studies, suggesting that the bending persistence length decreases with increasing temperatures. Using the Marko model and changing A and P according to the temperature increase, we find that the effective torsional stiffness of DNA needs to decrease with increasing temperatures. Predictions of the TWLC and the aTWLC model, also find a decrease of 5% going from 20°C to 40°C, which is in reasonable agreement with findings using coarse-grained and all-atom simulations.

Chapter 3 described the difficulties on torque-rotation measurements and how careful data has to be treated in order to resolve small effects on C_{eff}. The data presented here does not consist of a large number of measured molecules, in particular at high temperature. Therefore, increasing statistics will help to study the dependence on temperature. Using the multiplexed setup we are able to measure several molecules at the same time, such that statistics can be improved with a low number of performed measurements.

Acknowledgments

I thank Stefanos K. Nomidis (TWLC and aTWLC), Christian Matek (oxDNA), Tomáš Geršata, Martin Zacharias, and Filip Lankaš (all-atom) for providing simulation data.

6.5 Supplementary data

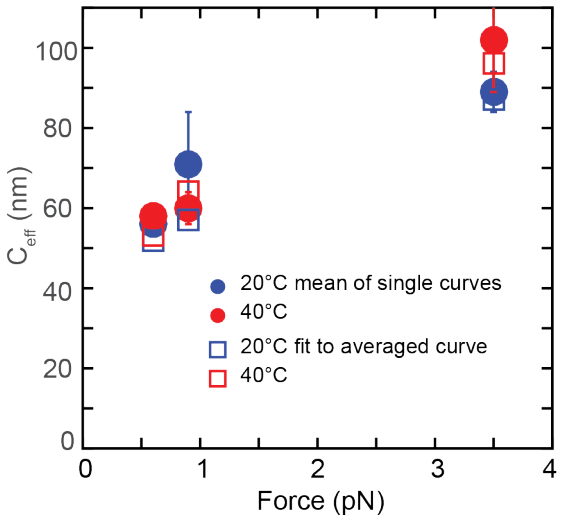

Figure 6.7: Comparison of C_{eff} taken from individual and averaged torque-rotation data. When fitting a line to the average torque dataset, the torsional stiffness is (mainly) underestimated to up to 15%. On the one hand, this comes from the low number of measured molecules, on the other hand it comes from a systematic error on the averaging algorithm, which is mainly due to the still unspecific location of zero torque. This problem, however, vanishes for higher statistics.

Part III

Conclusion and Outlook

Chapter 7
Conclusion and Outlook

DNA is the storage medium of all information needed to build or maintain a living organism. It consists of four building blocks, i.e. bases, which are aligned to code for genetic information. These bases pair up to form the double helical structure famously discovered by Watson and Crick in 1953. When reading the code, forces and torques are induced in order to make the genetic code accessible for enzymes. This calls for precise techniques to understand and measure forces and torques on the pN scale.

In Magnetic Tweezers (MT), a micrometer sized DNA molecule is tethered between a glass surface and a magnetic particle. Permanent magnets, placed above the sample, exert magnetic fields, which allow stretching and twisting of the magnetic bead and thus, the molecule. Freely Orbiting Magnetic Tweezers (FOMT) and Magnetic Torque Tweezers (MTT) are variations of MT that use a predominant vertical magnetic field. Both allow measuring changes in the rotation angle of the DNA molecule, which is a distinctive feature in contrast to conventional MT that use a horizontal magnetic field at the position of the magnetic particle and do not allow measuring angular changes. While the addition of torque is not possible in FOMT, it is in MTT. Within this work I have used and improved techniques, namely MT, FOMT and MTT, to address torsional properties of DNA.

It is difficult to accurately measure changes in the rotation angle as the respond is small. Therefore the torque respond of single molecules is noisy. In order to detect these small changes in the DNA molecule, in particular in the rotation angle, it is advantageous to measure many molecules in parallel to increase statistics. This work shows that both, freely orbiting magnetic tweezers and magnetic torque tweezers can be operated in a multiplexed fashion, but depend on measurement details, like magnetic beads.

Furthermore, this work presents and used a simplified version of MTT to probe the torsional response of DNA to induced torque at various salt conditions. The formation of plectonemes, in general, strongly depends on electrostatics, as the backbone of DNA is highly charged (one negative charge per base). Sharp bending brings charges in close proximity leading to electrostatic repulsion. The multiplexed setup helped to resolve that pure twist deformations, i.e. when bending is suppressed by high stretching forces ($F > 6$ pN) do not depend on the ionic environment, whereas the effective torsional stiffness decreases with increasing ionic strength

(F < 6 pN), mainly due to topological bending through twist deformations.

The change in extension of tether length upon the addition of torque is well described by the symmetric, isotropic elastic rod model. Moroz and Nelson derived an analytical formula to describe the twist behavior of DNA at different stretching forces. This model is in qualitative, however, not in quantitative agreement with previous findings. It fails, in particular, for forces smaller 2 pN, in the presence of bending effects, suggesting that twist and bend deformations are intrinsically coupled. Using the asymmetric, anisotropic elastic rod model and by comparing coarse-grained simulations of DNA with high-resolution MT data, an improved prediction for the twist persistence length upon stretching force is proposed, containing a twist-bend coupling and anisotropic bending along the helix.

Another question is to what extend torsional properties of DNA depend on temperature. Many molecules loose their structure and even their biological function, if exposed to extreme (and sometimes also small) changes in temperature. Hence, the setup was updated with a temperature control using an objective heating to locally heat the sample. From experiment and all-atom MD simulations it was found that DNA unwinds by -11 degree/(°C·kbp) and is independent of stretching force, at least for forces < 1 pN. All-atom simulations find that this is mainly due to a conformational change in the backbone sub-states and not due to melting of base pairs.

This conformational change within the DNA structure implies that the torsional stiffness of DNA is also affected by temperature. Preliminary data on the torque response of DNA at increased temperatures suggests that the torsional stiffness also decreases with increased temperature, which is in agreement with predictions of all-atom and coarse-grained MD simulations that overall predict a decrease of 10% going from 10 to roughly 60°C. Further measurements, will increase statistics and resolve the exact dependence of the torsional stiffness on temperature.

A novel way to directly measure molecular torque in a multiplexed fashion helped to collect statistics and improve measurement accuracies. Even small changes (< 10%), such as the effect of salt concentration or temperature on the torsional stiffness of DNA can now be resolved using MTT. In addition, MD simulations have improved, such that calculation times are much shorter for the same amount of data, reducing also the error on simulations. Overall, techniques are improving such that subtle effects, like the change in helical twist with temperature, can be accurately measured in MT and compared with MD simulations.

Learn from yesterday, live for today, hope for tomorrow. The important thing is not stop questioning.

Albert Einstein

This work focused on torsional properties of bare DNA. In the future, however, it is of interest to study higher order structures such as chromatin. The multiplexed FOMT setup can be used to observe changes in extension and the rotation angle during nucleosome formation or the formation of a nucleosome fiber with the help of remodeler proteins. Less is known about the mechanics of such a nucleosome fiber or the dynamics of remodelers. The temperature controlled setup allows studying systems that are sensitive to the temperature of the environment. The TBP, for example, shows enhanced activity if the temperature is similar to

its thermophilic growth condition. Another idea is to use the multiplexed MTT instrument, to test whether binding of proteins or small molecule binding to DNA is preferred if DNA is slightly underwound. A concrete example is to study the torque response of small molecules binding to DNA, like intercalators.

According to Albert Einstein: Having studied something belongs to the past. We learn from the past and place new scientific questions for the future.

Bibliography

[1] Franziska Kriegel, Niklas Ermann, and Jan Lipfert. Probing the mechanical properties, conformational changes, and interactions of nucleic acids with magnetic tweezers. *J. Struc. Biol.*, 197(1):26–36, January 2017.

[2] Franziska Kriegel, Niklas Ermann, Ruaridh Forbes, David Dulin, Nynke H. Dekker, and Jan Lipfert. Probing the salt dependence of the torsional stiffness of DNA by multiplexed magnetic torque tweezers. *Nucleic Acids Res.*, 45(10):5920–5929, April 2017.

[3] Stefanos K. Nomidis, Franziska Kriegel, Willem Vanderlinden, and Jan Lipfert. Twist-Bend Coupling and the Torsional Response of Double-Stranded DNA. *Physical Rev. Lett.*, 118:217801, May 2017.

[4] James D. Watson and Francis H. C. Crick. Molecular structure of nucleic acids. *Nature*, 171:737–738, April 1953.

[5] Abraham Worcel, Steven Strogatz, and Donald Riley. Structure of chromatin and the linking number of DNA. *Proc. Natl. Acad. Sci. U.S.A.*, 78(3):1461–1465, March 1981.

[6] Leroy F. Liu and James C. Wang. Supercoiling of the DNA template during transcription. *Proc. Natl. Acad. Sci. U.S.A.*, 84(20):7024–7027, October 1987.

[7] Karolin Luger, Armin W. Mäder, Robin K. Richmond, David F. Sargent, and Timothy J. Richmond. Crystal structure of the nucleosome core particle at 2.8 A resolution. *Nature*, 389(6648):251–260, September 1997.

[8] Nicholas R. Cozzarelli, Gregory J. Cost, Marcelo Nöllmann, Thierry Viard, and James E. Stray. Giant proteins that move DNA: bullies of the genomic playground. *Nat Rev Mol Cell Biol*, 7(8):580–588, August 2006.

[9] Daniel A. Koster, Aurélien Crut, Stewart Shuman, Mary-Ann Bjornsti, and Nynke H. Dekker. Cellular strategies for regulating DNA supercoiling: a single-molecule perspective. *Cell*, 142(4):519–530, August 2010.

[10] Joaquim Roca. The torsional state of DNA within the chromosome. *Chromosoma*, 120(4): 323–334, August 2011.

[11] Jan Lipfert, Maarten M. van Oene, Mina Lee, Francesco Pedaci, and Nynke H. Dekker. Torque spectroscopy for the study of rotary motion in biological systems. *Chem. Rev.*, 115(3):1449–1474, February 2015.

[12] Thomas R. Cech. Self-splicing of group I introns. *Annu. Rev. Biochem.*, 59:543–568, 1990.

[13] Wade C. Winkler and Ronald R. Breaker. Regulation of bacterial gene expression by riboswitches. *Annu. Rev. Microbiol.*, 59(1):487–517, October 2005.

[14] Andrew Fire, SiQun Xu, Mary K. Montgomery, Steven A. Kostas, Samuel E. Driver, and Craig C. Mello. Potent and specific genetic interference by double-stranded RNA in Caenorhabditis elegans. *Nature*, 391(6669):806–811, February 1998.

[15] Martin Jinek, Krzysztof Chylinski, Ines Fonfara, Michael Hauer, Jennifer A. Doudna, and Emmanuelle Charpentier. A programmable dual-RNA-guided DNA endonuclease in adaptive bacterial immunity. *Science*, 337(6096):816–821, August 2012.

[16] Marius Rutkauskas, Tomas Sinkunas, Inga Songailiene, Maria S. Tikhomirova, Virginijus Siksnys, and Ralf Seidel. Directional R-Loop Formation by the CRISPR-Cas Surveillance Complex Cascade Provides Efficient Off-Target Site Rejection. *Cell Rep*, 10(9):1534–1543, March 2015.

[17] Florence Tama, Mikel Valle, Joachim Frank, and Charles L. Brooks. Dynamic reorganization of the functionally active ribosome explored by normal mode analysis and cryo-electron microscopy. *Proc. Natl. Acad. Sci. U.S.A.*, 100(16):9319–9323, August 2003.

[18] Barbara S. Schuwirth, Maria A. Borovinskaya, Cathy W. Hau, Wen Zhang, Antón Vila-Sanjurjo, James M. Holton, and Jamie H. Doudna Cate. Structures of the bacterial ribosome at 3.5 A resolution. *Science*, 310(5749):827–834, November 2005.

[19] Rebecca W. Alexander, John Eargle, and Zaida Luthey-Schulten. Experimental and computational determination of tRNA dynamics. *FEBS letters*, 584(2):376–386, January 2010.

[20] Gwangrog Lee, Matthew A. Bratkowski, Fang Ding, Ailong Ke, and Taekjip Ha. Elastic coupling between RNA degradation and unwinding by an exoribonuclease. *Science*, 336 (6089):1726–1729, June 2012.

[21] Paul W. K. Rothemund. Folding DNA to create nanoscale shapes and patterns. *Nature*, 440(7082):297–302, March 2006.

[22] Carlos Ernesto Castro, Fabian Kilchherr, Do-Nyun Kim, Enrique Lin Shiao, Tobias Wauer, Philipp Wortmann, Mark Bathe, and Hendrik Dietz. A primer to scaffolded DNA origami. *Nat. Methods Methods*, 8(3):221–229, March 2011.

[23] Camille J. Delebecque, Ariel B. Lindner, Pamela A. Silver, and Faisal A. Aldaye. Organization of intracellular reactions with rationally designed RNA assemblies. *Science*, 333 (6041):470–474, July 2011.

[24] Anton Kuzyk, Robert Schreiber, Zhiyuan Fan, Günther Pardatscher, Eva-Maria Roller, Alexander Högele, Friedrich C. Simmel, Alexander O. Govorov, and Tim Liedl. DNA-based self-assembly of chiral plasmonic nanostructures with tailored optical response. *Nature*, 483(7389):311–314, March 2012.

[25] Martin Langecker, Vera Arnaut, Thomas G. Martin, Jonathan List, Stephan Renner, Michael Mayer, Hendrik Dietz, and Friedrich C. Simmel. Synthetic lipid membrane channels formed by designed DNA nanostructures. *Science*, 338(6109):932–936, November 2012.

[26] Thomas Gerling, Klaus F. Wagenbauer, Andrea M. Neuner, and Hendrik Dietz. Dynamic DNA devices and assemblies formed by shape-complementary, non-base pairing 3D components. *Science*, 347(6229):1446–1452, March 2015.

[27] Charbel Haber and Denis Wirtz. Magnetic tweezers for DNA micromanipulation. *Rev. Sci. Instrum.*, 71(12):4561–4570, December 2000.

[28] Charlie Gosse and Vincent Croquette. Magnetic tweezers: micromanipulation and force measurement at the molecular level. *Biophys. J.*, 82(6):3314–3329, June 2002.

[29] Chi-Han Chiou, Yu-Yen Huang, Meng-Han Chiang, Huei-Huang Lee, and Gwo-Bin Lee. New magnetic tweezers for investigation of the mechanical properties of single DNA molecules. *Nanotechnology*, 17(5):1217–1224, March 2006.

[30] Keir C. Neuman and Attila Nagy. Single-molecule force spectroscopy: optical tweezers, magnetic tweezers and atomic force microscopy. *Nature Methods*, 5:491–505, May 2008.

[31] David Dulin, Jan Lipfert, M. Charl Moolman, and Nynke H. Dekker. Studying genomic processes at the single-molecule level: introducing the tools and applications. *Nat. Rev. Genet.*, 14(1):9–22, January 2013.

[32] David Dulin, Bojk A. Berghuis, Martin Depken, and Nynke H. Dekker. Untangling reaction pathways through modern approaches to high-throughput single-molecule force-spectroscopy experiments. *Curr. Opin. Struct. Biol.*, 34:116–122, October 2015.

[33] Alfredo Celedon, Ilana M. Nodelman, Bridget Wildt, Rohit Dewan, Peter Searson, Denis Wirtz, Gregory D. Bowman, and Sean X. Sun. Magnetic tweezers measurement of single molecule torque. *Nano Lett.*, 9(4):1720–1725, April 2009.

[34] Jan Lipfert, Jacob W. J. J Kerssemakers, Tessa Jager, and Nynke H. Dekker. Magnetic torque tweezers: measuring torsional stiffness in DNA and RecA-DNA filaments. *Nat. Methods*, 7(12):977–980, December 2010.

[35] Dominik J. Kauert, Thomas Kurth, Tim Liedl, and Ralf Seidel. Direct Mechanical Measurements Reveal the Material Properties of Three-Dimensional DNA Origami. *Nano Lett.*, 11(12):5558–5563, December 2011.

[36] Jan Lipfert, Matthew Wiggin, Jacob W. J. Kerssemakers, Francesco Pedaci, and Nynke H. Dekker. Freely orbiting magnetic tweezers to directly monitor changes in the twist of nucleic acids. *Nat. Commun.*, 2:439–9, July 2011.

[37] Francesco Mosconi, Jean François Allemand, and Vincent Croquette. Soft magnetic tweezers: a proof of principle. *Rev. Sci. Instrum.*, 82(3):034302, March 2011.

[38] Jan Janssen, Xander J. A .and Lipfert, Tessa Jager, Renier Daudey, Jaap Beekman, and Nynke H. Dekker. Electromagnetic torque tweezers: a versatile approach for measurement of single-molecule twist and torque. *Nano Lett.*, 12(7):3634–3639, July 2012.

[39] Scott Forth, Maxim Y Sheinin, James Inman, and Michelle D Wang. Torque measurement at the single-molecule level. *Annual review of biophysics*, 42(1):583–604, 2013.

[40] Paul Lebel, Aakash Basu, Florian C. Oberstrass, Elsa M. Tretter, and Zev Bryant. Gold rotor bead tracking for high-speed measurements of DNA twist, torque and extension. *Nat. Methods*, 11(4):456–462, April 2014.

[41] Terence R. Strick, Jean F. Allemand, David Bensimon, Aaron Bensimon, and Vincent Croquette. The elasticity of a single supercoiled DNA molecule. *Science*, 271(5257): 1835–1837, March 1996.

[42] Jan Lipfert, Xiaomin Hao, and Nynke H. Dekker. Quantitative modeling and optimization of magnetic tweezers. *Biophys. J.*, 96(12):5040–5049, June 2009.

[43] Bob M. Lansdorp and Omar A. Saleh. Power spectrum and Allan variance methods for calibrating single-molecule video-tracking instruments. *Rev. Sci. Instrum.*, 83(2):025115, February 2012.

[44] Zhongbo Yu, David Dulin, Jelmer Cnossen, Mariana Köber, Maarten M. van Oene, Orkide Ordu, Bojk A. Berghuis, Toivo Hensgens, Jan Lipfert, and Nynke H. Dekker. A force calibration standard for magnetic tweezers. *Rev. Sci. Instrum.*, 85(12):123114, December 2014.

[45] Maarten M. van Oene, Laura E. Dickinson, Francesco Pedaci, Mariana Köber, David Dulin, Jan Lipfert, and Nynke H. Dekker. Biological magnetometry: torque on superparamagnetic beads in magnetic fields. *Phys. Rev. Lett.*, 114(21):218301, May 2015.

[46] Zev Bryant, Michael D. Stone, Jeff Gore, Steven B. Smith, Nicholas R. Cozzarelli, and Carlos Bustamante. Structural transitions and elasticity from torque measurements on DNA. *Nature*, 424(6946):338–341, July 2003.

[47] Jeff Gore, Zev Bryant, Michael D Stone, Marcelo Nöllmann, Nicholas R Cozzarelli, and Carlos Bustamante. Mechanochemical analysis of DNA gyrase using rotor bead tracking. *Nature*, 439(7072):100–104, January 2006.

[48] Florian C Oberstrass, Louis E Fernandes, and Zev Bryant. Torque measurements reveal sequence-specific cooperative transitions in supercoiled DNA. *Proceedings of the National Academy of Sciences of the United States of America*, 109(16):6106–6111, April 2012.

[49] Jan Lipfert, Gary M. Skinner, Johannes M. Keegstra, Toivo Hensgens, Tessa Jager, David Dulin, Mariana Köber, Zhongbo Yu, Serge P. Donkers, Fang-Chieh Chou, Rhiju Das, and Nynke H. Dekker. Double-stranded RNA under force and torque: similarities to and striking differences from double-stranded DNA. *Proc. Natl. Acad. Sci. U.S.A.*, 111(43): 15408–15413, October 2014.

[50] X J A Janssen, A J Schellekens, K van Ommering, L J van IJzendoorn, and M W J Prins. Controlled torque on superparamagnetic beads for functional biosensors. *Biosens Bioelectron*, 24(7):1937–1941, March 2009.

[51] Richard Wing, Horace Drew, Tsunehiro Takano, Chris Broka, Shoji Tanaka, Keiichi Itakura, and Richard E. Dickerson. Crystal structure analysis of a complete turn of B-DNA. *Nature*, 287(5784):755–758, October 1980.

[52] Daniela Rhodes and Aaron Klug. Helical periodicity of DNA determined by enzyme digestion. *Nature*, 286(5773):573–578, August 1980.

[53] P Taylor, F Rixon, and U Desselberger. Rise per base pair in helices of double-stranded rotavirus RNA determined by electron microscopy. *Virus research*, 2(2):175–182, March 1985.

[54] P Nelson. *Biological Physics: Energy, Information Life*. Freeman & Co, 2004.

[55] Carlos Bustamante, John F. Marko, Erid D. Siggia, and Steven B. Smith. Entropic elasticity of lambda-phage DNA. *Science*, 265(5178):1599–1600, September 1994.

[56] John F. Marko and Eric D. Siggia. Stretching DNA. *Macromolecules*, 28(26):8759–8770, December 1995.

[57] J A Abels, Fernando Moreno-Herrero, T Van Der Heijden, Cees Dekker, and Nynke H. H Dekker. Single-molecule measurements of the persistence length of double-stranded RNA. *Biophys. J.*, 88(4):2737–2744, April 2005.

[58] Christoph G. Baumann, Steven B. Smith, Victor A. Bloomfield, and Carlos Bustamante. Ionic effects on the elasticity of single DNA molecules. *Proc. Natl. Acad. Sci. U.S.A.*, 94 (12):6185–6190, June 1997.

[59] C Bouchiat, Michelle D. Wang, Jean F. Allemand, Terence R. Strick, S M Block, and Vincent Croquette. Estimating the persistence length of a worm-like chain molecule from force-extension measurements. *Biophys. J.*, 76(1 Pt 1):409–413, January 1999.

[60] Jay R. Wenner, Mark C. Williams, Ioulia Rouzina, and Victor A. Bloomfield. Salt dependence of the elasticity and overstretching transition of single DNA molecules. *Biophys. J.*, 82(6):3160–3169, June 2002.

[61] Elías Herrero-Galán, Maria Eugenia Fuentes-Perez, Carolina Carrasco, José M. Valpuesta, José L Carrascosa, Fernando Moreno-Herrero, and J. Ricardo Arias-Gonzalez. Mechanical identities of RNA and DNA double helices unveiled at the single-molecule level. *J. Am. Chem. Soc.*, 135(1):122–131, January 2013.

[62] Theo Odijk. Polyelectrolytes near the rod limit. *J Polym Sci B Polym Phys*, 15(3):477–483, March 1977.

[63] Jeffrey Skolnick and Marshall Fixman. Electrostatic Persistence Length of a Wormlike Polyelectrolyte. *Macromolecules*, 10(5):944–948, September 1977.

[64] Christoph G. Baumann, Victor A. Bloomfield, Steven B. Smith, Carlos Bustamante, Michelle D. Wang, and Steven M. Block. Stretching of single collapsed DNA molecules. *Biophys. J.*, 78(4):1965–1978, April 2000.

[65] Annael Brunet, Catherine Tardin, Laurence Salomé, Philippe Rousseau, Nicolas Destainville, and Manoel Manghi. Dependence of DNA persistence length on ionic strength of solutions with monovalent and divalent salts: A joint theory–experiment study. *Macromolecules*, 48(11):3641–3652, May 2015.

[66] D. B. McIntosh and Omar A. Saleh. Salt species-dependent electrostatic effects on ssDNA elasticity. *Macromolecules*, 44(7):2328–2333, March 2011.

[67] MC Murphy, Ivan Rasnik, Wei Cheng, Timothy M. Lohman, and Taekjip Ha. Probing Single-Stranded DNA Conformational Flexibility Using Fluorescence Spectroscopy. *Biophys. J.*, 86(4):2530–2537, April 2004.

[68] Omar A. Saleh, D B McIntosh, P Pincus, and N Ribeck. Nonlinear Low-Force Elasticity of Single-Stranded DNA Molecules. *Phys. Rev. Lett.*, 102(6):068301, February 2009.

[69] A. Y. Sim, Jan Lipfert, Daniel Herschlag, and Sebastian Doniach. Salt dependence of the radius of gyration and flexibility of single-stranded DNA in solution probed by small-angle x-ray scattering. *Phys. Rev. E Stat. Nonlin. Soft Matter Phys.*, 86(2-1):021901, August 2012.

[70] Theo Odijk. Stiff Chains and Filaments Under Tension. *Macromolecules*, 28(20):7016–7018, September 1995.

[71] Steven B. Smith, Y. Cui, and Carlos Bustamante. Overstretching B-DNA: the elastic response of individual double-stranded and single-stranded DNA molecules. *Science*, 271 (5250):795–799, February 1996.

[72] Fang-Chieh Chou, Jan Lipfert, and Rhiju Das. Blind predictions of DNA and RNA tweezers experiments with force and torque. *PLoS computational biology*, 10(8):e1003756, August 2014.

[73] Bryant S Fujimoto and J. Michael Schurr. Dependence of the torsional rigidity of DNA on base composition. *Nature*, 344(6262):175–177, March 1990.

[74] Paul R. Selvin, David N. Cook, Ning G. Pon, William R. Bauer, Melvin P. Klein, and John E. Hearst. Torsional rigidity of positively and negatively supercoiled DNA. *Science*, 255 (5040):82–85, January 1992.

[75] Patrick J. Heath, James B. Clendenning, Bryant S. Fujimoto, and Michael J. Schurr. Effect of Bending Strain on the Torsion Elastic Constant of DNA. *J. Mol. Biol.*, 260(5):718–730, August 1996.

[76] Francesco Mosconi, Jean F. Allemand, David Bensimon, and Vincent Croquette. Measurement of the torque on a single stretched and twisted DNA using magnetic tweezers. *Phys. Rev. Lett.*, 102(7):078301, February 2009.

[77] J. David Moroz and Philip Nelson. Entropic elasticity of twist-storing polymers. *Macromolecules*, 31(18):6333–6347, August 1998.

[78] J. David Moroz and Philip Nelson. Torsional directed walks, entropic elasticity, and DNA twist stiffness. *Proc. Natl. Acad. Sci. U.S.A.*, 94(26):14418–14422, December 1997.

[79] Thibaut Lepage, François Képès, and Ivan Junier. Thermodynamics of Long Supercoiled Molecules: Insights from Highly Efficient Monte Carlo Simulations. *Biophys. J.*, 109(1): 135–143, July 2015.

[80] J. Michael Schurr. A Possible Cooperative Structural Transition of DNA in the 0.25–2.0 pN Range. *J Phys Chem Lett*, 119(21):6389–6400, May 2015.

[81] Rebecca S. Mathew-Fenn, Rhiju Das, and Pehr A. B. Harbury. Remeasuring the double helix. *Science*, 322(5900):446–449, October 2008.

[82] R. D. Kamien, T. C. Lubensky, Philip Nelson, and C. S. O'Hern. Direct determination of DNA twist-stretch coupling. *Europhysics Letters*, 38(3):237, 1997.

[83] John F. Marko. Stretching must twist DNA. *Europhysics Letters*, 38(3):183–188, April 1997.

[84] Jeff Gore, Zev Bryant, Marcelo Nöllmann, Mai U. Le, Nicholas R. Cozzarelli, and Carlos Bustamante. DNA overwinds when stretched. *Nature*, 442(7104):836–839, August 2006.

[85] Timothée Lionnet, Sylvain Joubaud, Richard Lavery, David Bensimon, and Vincent Croquette. Wringing out DNA. *Phys. Rev. Lett.*, 96(17):178102, May 2006.

[86] Kasper Olsen and Jakob Bohr. The geometrical origin of the strain-twist coupling in double helices. *Rev. Sci. Instrum.*, 1(1):012108, Februar 2011.

[87] Christian Matek, Thomas E. Ouldridge, Jonathan P. K. Doye, and Ard A. Louis. Plectoneme tip bubbles: coupled denaturation and writhing in supercoiled DNA. *Sci Rep*, 5 (1):7655, January 2015.

[88] Christian Matek, Petr Šulc, Ferdinando Randisi, Jonathan P. K. Doye, and Ard A. Louis. Coarse-grained modelling of supercoiled RNA. *Rev. Sci. Instrum.*, 143(24):243122, December 2015.

[89] Korbinian Liebl, Tomas Drsata, Filip Lankas, Jan Lipfert, and Martin Zacharias. Explaining the striking difference in twist-stretch coupling between DNA and RNA: A comparative molecular dynamics analysis. *Nucleic Acids Res.*, 43(21):10143–10156, December 2015.

[90] Maxim Y. Sheinin, Scott Forth, John F. Marko, and Michelle D. Wang. Underwound DNA under Tension: Structure, Elasticity, and Sequence-Dependent Behaviors. *Phys. Rev. Lett.*, 107(10):108102, September 2011.

[91] John F. Marko. Torque and dynamics of linking number relaxation in stretched supercoiled DNA. *Phys. Rev. E Stat. Nonlin. Soft Matter Phys.*, 76(2 Pt 1):021926, August 2007.

[92] Terence R. Strick, Vincent Allemand, Jean F.and Croquette, and David Bensimon. Twisting and stretching single DNA molecules. *Prog. Biophys. Mol. Biol.*, 74(1-2):115–140, August 2000.

[93] Robert Schöpflin, Hergen Brutzer, Oliver Müller, Ralf Seidel, and Gero Wedemann. Probing the elasticity of DNA on short length scales by modeling supercoiling under tension. *Biophys. J.*, 103(2):323–330, July 2012.

[94] Christopher Maffeo, Robert Schöpflin, Hergen Brutzer, René Stehr, Aleksei Aksimentiev, Gero Wedemann, and Ralf Seidel. DNA-DNA interactions in tight supercoils are described by a small effective charge density. *Phys. Rev. Lett.*, 105(15):158101–158104, October 2010.

[95] John F. Marko and Sébastien Neukirch. Competition between curls and plectonemes near the buckling transition of stretched supercoiled DNA. *Phys. Rev. E Stat. Nonlin. Soft Matter Phys.*, 85(1 Pt 1):011908, January 2012.

[96] Marijn T. J. van Loenhout, MV de Grunt, and Cees Dekker. Dynamics of DNA Supercoils. *Science*, 338(6103):94–97, October 2012.

[97] Marc Emanuel, Giovanni Lanzani, and Helmut Schiessel. Multiplectoneme phase of double-stranded DNA under torsion. *Phys. Rev. E Stat. Nonlin. Soft Matter Phys.*, 88(2): 022706, August 2013.

[98] Maxim Y. Sheinin and Michelle D. Wang. Twist–stretch coupling and phase transition during DNA supercoiling. *Phys Chem Chem Phys*, 11(24):4800–4803, May 2009.

[99] Jean F. Allemand, David Bensimon, Richard Lavery, and Vincent Croquette. Stretched and overwound DNA forms a Pauling-like structure with exposed bases. *Proc. Natl. Acad. Sci. U.S.A.*, 95(24):14152–14157, November 1998.

[100] Jeff Wereszczynski and Ioan Andricioaei. On structural transitions, thermodynamic equilibrium, and the phase diagram of DNA and RNA duplexes under torque and tension. *Proc. Natl. Acad. Sci. U.S.A.*, 103(44):16200–16205, October 2006.

[101] Linus Pauling and Robert B. Corey. Two Rippled-Sheet Configurations of Polypeptide Chains, and a Note about the Pleated Sheets. *Proc. Natl. Acad. Sci. U.S.A.*, 39(4):253–256, April 1953.

[102] John F. Marko and Sébastien Neukirch. Global force-torque phase diagram for the DNA double helix: Structural transitions, triple points, and collapsed plectonemes. *Phys Rev E*, 88(6):062722, December 2013.

[103] E A Galburt, E J Tomko, W T Stump, and A Ruiz Manzano. Force-dependent melting of supercoiled DNA at thermophilic temperatures. *Biophys. Chem.*, 187-188:23–28, March 2014.

[104] Domenico Salerno, Alessia Tempestini, I Mai, Doriano Brogioli, Roberto Ziano, Valeria Cassina, and Francesco Mantegazza. Single-molecule study of the DNA denaturation phase transition in the force-torsion space. *Phys. Rev. Lett.*, 109(11):118303, September 2012.

[105] Alessia Tempestini, Valeria Cassina, Doriano Brogioli, Roberto Ziano, Simona Erba, Roberto Giovannoni, Maria G. Cerrito, Domenico Salerno, and Francesco Mantegazza. Magnetic tweezers measurements of the nanomechanical stability of DNA against denaturation at various conditions of pH and ionic strength. *Nucleic Acids Res.*, 41(3): 2009–2019, February 2013.

[106] T. J. Thomas and Victor A. Bloomfield. Chain flexibility and hydrodynamics of the B and Z forms of poly(dG-dC).poly(dG-dC). *Nucleic Acids Res.*, 11(6):1919–1930, March 1983.

[107] Mina Lee, Sook Ho Kim, and Seok-Cheol Hong. Minute negative superhelicity is sufficient to induce the B-Z transition in the presence of low tension. *Proc. Natl. Acad. Sci. U.S.A.*, 107(11):4985–4990, March 2010.

[108] Florian C. Oberstrass, Louis E. Fernandes, Paul Lebel, and Zev Bryant. Torque spectroscopy of DNA: base-pair stability, boundary effects, backbending, and breathing dynamics. *Proc. Natl. Acad. Sci. U.S.A.*, 110(17):178103, April 2013.

[109] Michael Bonin, Rong Zhu, Yvonne Klaue, Jürgen Oberstrass, Egbert Oesterschulze, and Wolfgang Nellen. Analysis of RNA flexibility by scanning force spectroscopy. *Nucleic Acids Res.*, 30(16):e81, August 2002.

[110] P Cluzel, A Lebrun, C Heller, R Lavery, J L Viovy, D Chatenay, and F Caron. DNA: an extensible molecule. *Science*, 271(5250):792–794, February 1996.

[111] Jay R. Williams, Mark C.and Wenner, Ioulia Rouzina, and Victor A. Bloomfield. Entropy and heat capacity of DNA melting from temperature dependence of single molecule stretching. *Biophys. J.*, 80(4):1932–1939, April 2001.

[112] Matthias Rief, Hauke Clausen-Schaumann, and Hermann E. Gaub. Sequence-dependent mechanics of single DNA molecules. *Nat. Struct. Biol.*, 6(4):346–349, April 1999.

[113] Mark C. Williams, Jay R. Wenner, Ioulia Rouzina, and Victor A. Bloomfield. Effect of pH on the overstretching transition of double-stranded DNA: evidence of force-induced DNA melting. *Biophys. J.*, 80(2):874–881, February 2001.

[114] J F Leger, G Romano, Sarkar, J Robert, and L Bourdieu. Structural transitions of a twisted and stretched DNA molecule. *Physical Rev. Lett.*, 83(5):1066–1069, August 1999.

[115] A Sarkar, J F Leger, D Chatenay, and J F Marko. Structural transitions in DNA driven by external force and torque. *Physical review. E, Statistical, nonlinear, and soft matter physics*, 63(5 Pt 1):051903, May 2001.

[116] Joost van Mameren, Peter Gross, Geraldine Farge, Pleuni Hooijman, Mauro Modesti, Maria Falkenberg, Gijs J L Wuite, and Erwin J G Peterman. Unraveling the structure of DNA during overstretching by using multicolor, single-molecule fluorescence imaging. *Proc. Natl. Acad. Sci. U.S.A.*, 106(43):18231–18236, October 2009.

[117] D. Hern Paik and Thomas T. Perkins. Overstretching DNA at 65 pN does not require peeling from free ends or nicks. *J. Am. Chem. Soc.*, 133(10):3219–3221, March 2011.

[118] Niklas Bosaeus, Afaf H. El-Sagheer, Tom Brown, Steven B. Smith, Björn Åkerman, Carlos Bustamante, and Bengt Nordén. Tension induces a base-paired overstretched DNA conformation. *Proc. Natl. Acad. Sci. U.S.A.*, 109(38):15179–15184, September 2012.

[119] Graeme A. King, Peter Gross, Ulrich Bockelmann, Mauro Modesti, Gijs J. L. Wuite, and Erwin J. G. Peterman. Revealing the competition between peeled ssDNA, melting bubbles, and S-DNA during DNA overstretching using fluorescence microscopy. *Proc. Natl. Acad. Sci. U.S.A.*, 110(10):3859–3864, March 2013.

[120] Xinghua Zhang, Hu Chen, Hongxia Fu, Patrick S Doyle, and Jie Yan. Two distinct overstretched DNA structures revealed by single-molecule thermodynamics measurements. *Proc. Natl. Acad. Sci. U.S.A.*, 109(21):8103–8108, May 2012.

[121] Cornelis Storm and Philip Nelson. Theory of high-force DNA stretching and overstretching. *Phys. Rev. E Stat. Nonlin. Soft Matter Phys.*, 67(5 Pt 1):051906, May 2003.

[122] Zev Bryant, Florian C. Oberstrass, and Aakash Basu. Recent developments in single-molecule DNA mechanics. *Curr. Opin. Struct. Biol.*, 22(3):304–312, June 2012.

[123] Maria Manosas, Adrien Meglio, Michelle M. Spiering, Fangyuan Ding, Stephen J. Benkovic, François-Xavier Barre, Omar A. Saleh, Jean François Allemand, David Bensimon, and Vincent Croquette. Magnetic tweezers for the study of DNA tracking motors. *Methods Enzymol*, 475:297–320, November 2010.

[124] Jan Lipfert, Sven Klijnhout, and Nynke H Dekker. Torsional sensing of small-molecule binding using magnetic tweezers. *Nucleic Acids Res.*, 38(20):7122–7132, November 2010.

[125] Domenico Salerno, Doriano Brogioli, Valeria Cassina, D Turchi, G L Beretta, D Seruggia, R Ziano, F Zunino, and Francesco Mantegazza. Magnetic tweezers measurements of the nanomechanical properties of DNA in the presence of drugs. *Nucleic Acids Res.*, 38(20): 7089–7099, November 2010.

[126] Rupert Krautbauer, Lisa H. Pope, Tobias E. Schrader, Stephanie Allen, and Hermann E. Gaub. Discriminating small molecule DNA binding modes by single molecule force spectroscopy. *FEBS letters*, 510(3):154–158, January 2002.

[127] A. Gregory Matera, Rebecca M. Terns, and Michael P. Terns. Non-coding RNAs: lessons from the small nuclear and small nucleolar RNAs. *Nat. Rev. Mol. Cell Biol.*, 8(3):209–220, March 2007.

[128] Andy Sischka, Katja Toensing, Rainer Eckel, Sven David Wilking, Norbert Sewald, Robert Ros, and Dario Anselmetti. Molecular mechanisms and kinetics between DNA and DNA binding ligands. *Biophys. J.*, 88(1):404–411, January 2005.

[129] Ioana D. Vladescu, Micah J. McCauley, Megan E. Nuñez, Ioulia Rouzina, and Mark C. Williams. Quantifying force-dependent and zero-force DNA intercalation by single-molecule stretching. *Nat. Methods*, 4(6):517–522, June 2007.

[130] Katrin Günther, Michael Mertig, and Ralf Seidel. Mechanical and structural properties of YOYO-1 complexed DNA. *Nucleic Acids Res.*, 38(19):6526–6532, October 2010.

[131] Franci Johansen and Jens P. Jacobsen. 1H NMR studies of the bis-intercalation of a homodimeric oxazole yellow dye in DNA oligonucleotides. *J. Biomol. Struct. Dyn.*, 16(2): 205–222, October 1998.

[132] Alfredo Celedon, Denis Wirtz, and Sean Sun. Torsional mechanics of DNA are regulated by small-molecule intercalation. *J Phys Chem B*, 114(50):16929–16935, December 2010.

[133] Yoshie Harada, Osamu Ohara, Akira Takatsuki, Hiroyasu Itoh, Nobuo Shimamoto, and Kazuhiko Kinosita. Direct observation of DNA rotation during transcription by Escherichia coli RNA polymerase. *Nature*, 409(6816):113–115, January 2001.

[134] Jie Ma, Lu Bai, and Michelle D. Wang. Transcription under torsion. *Science*, 340(6140): 1580–1583, June 2013.

[135] A Candelli, T P Hoekstra, Geraldine Farge, Peter Gross, Erwin J. G. Peterman, and Gijs J. L. Wuite. A toolbox for generating single-stranded DNA in optical tweezers experiments. *Biopolymers*, 99(9):611–620, September 2013.

[136] Mina Lee, Jan Lipfert, Humberto Sanchez, Claire Wyman, and Nynke H. Dekker. Structural and torsional properties of the RAD51-dsDNA nucleoprotein filament. *Nucleic Acids Res.*, 41(14):7023–7030, August 2013.

[137] Maxim Y. Sheinin, Ming Li, Mohammad Soltani, Karolin Luger, and Michelle D. Wang. Torque modulates nucleosome stability and facilitates H2A/H2B dimer loss. *Nat. Commun.*, 4:2579, October 2013.

[138] Rifka Vlijm, Mina Lee, Jan Lipfert, Alexandra Lusser, Cees Dekker, and Nynke H. Dekker. Nucleosome Assembly Dynamics Involve Spontaneous Fluctuations in the Handedness of Tetrasomes. *Cell Rep*, 10(2):216–225, January 2015.

[139] Aakash Basu, Allyn J. Schoeffler, James M. Berger, and Zev Bryant. ATP binding controls distinct structural transitions of Escherichia coli DNA gyrase in complex with DNA. *Nat. Struct. Mol. Biol.*, 19(5):538–546, April 2012.

[140] Taisaku Ogawa, Katsunori Yogo, Shou Furuike, Kazuo Sutoh, Akihiko Kikuchi, and Kazuhiko Kinosita. Direct observation of DNA overwinding by reverse gyrase. *Proc. Natl. Acad. Sci. U.S.A.*, 112(24):7495–7500, June 2015.

[141] David Goodstein. *Adventures of Cosmology*. World Scientific, 2011.

[142] Steven B. Smith, Laura Finzi, and Carlos Bustamante. Direct mechanical measurements of the elasticity of single DNA molecules by using magnetic beads. *Science*, 258(5085): 1122–1126, November 1992.

[143] Michael Hinczewski, Yann von Hansen, and Roland R. Netz. Deconvolution of dynamic mechanical networks. *Proc. Natl. Acad. Sci. U.S.A*, 107(50):21493–21498, December 2010.

[144] Michael Hinczewski, J. Christof M. Gebhardt, Matthias Rief, and D. Thirumalai. From mechanical folding trajectories to intrinsic energy landscapes of biopolymers. *Proc. Natl. Acad. Sci. U.S.A*, 110(12):4500–4505, March 2013.

[145] Terence R. Strick, Vincent Croquette, and David Bensimon. Homologous pairing in stretched supercoiled DNA. *Proc. Natl. Acad. Sci. U.S.A*, 95(18):10579–10583, September 1998.

[146] Jan Lipfert, Jacob J. W. Kerssemakers, Maylon Rojer, and Nynke H. Dekker. A method to track rotational motion for use in single-molecule biophysics. *Rev. Sci. Instrum.*, 82(10): 103707, October 2011.

[147] Jelmer P. Cnossen, David Dulin, and Nynke H. Dekker. An optimized software framework for real-time, high-throughput tracking of spherical beads. *Rev. Sci. Instrum.*, 85(10): 103712, October 2014.

[148] Iwijn De Vlaminck, Thomas Henighan, Marijn T. J. van Loenhout, Indriati Pfeiffer, Julius Huijts, Jacob W. J. Kerssemakers, Allard J. Katan, Anja van Langen-Suurling, Emile van der Drift, Claire Wyman, and Cees Dekker. Highly parallel magnetic tweezers by targeted DNA tethering. *Nano Lett.*, 11(12):5489–5493, December 2011.

[149] Noah Ribeck and Omar A Saleh. Multiplexed single-molecule measurements with magnetic tweezers. *Rev. Sci. Instrum.*, 79(9):094301, September 2008.

[150] Alexander Huhle, Daniel Klaue, Hergen Brutzer, Peter Daldrop, Sihwa Joo, Oliver Otto, Ulrich F. Keyser, and Ralf Seidel. Camera-based three-dimensional real-time particle tracking at kHz rates and Ångström accuracy. *Nat. Commun.*, 6:5885, January 2015.

[151] Benjamin Gollnick, Carolina Carrasco, Francesca Zuttion, Neville S. Gilhooly, Mark S. Dillingham, and Fernando Moreno-Herrero. Probing DNA helicase kinetics with temperature-controlled magnetic tweezers. *Small*, 11(11):1273–1284, March 2015.

[152] Iwijn De Vlaminck, Thomas Henighan, Marijn T. J. T van Loenhout, Daniel R. Burnham, and Cees Dekker. Magnetic forces and DNA mechanics in multiplexed magnetic tweezers. *PloS one*, 7(8):0041432, August 2012.

[153] Felix E. Kemmerich, Marko Swoboda, Dominik J. Kauert, M. Svea Grieb, Steffen Hahn, Ralf Schwarz, Friedrich W.nd Seidel, and Michael Schlierf. Simultaneous Single-Molecule Force and Fluorescence Sampling of DNA Nanostructure Conformations Using Magnetic Tweezers. *Nano Lett.*, 16(1):381–386, December 2015.

[154] David Dulin, Igor D. Vilfan, Bojk A. Berghuis, Susanne Hage, Dennis H. Bamford, Minna M. Poranen, Martin Depken, and Nynke H. Dekker. Elongation-Competent Pauses Govern the Fidelity of a Viral RNA-Dependent RNA Polymerase. *Cell Rep*, 10(6): 983–992, February 2015.

[155] Bruce Alberts, Alexander Johnson, Julian Lewis, Martin Raff, Keith Roberts, and Peter Walter. *Molecular Biology of the Cell.* Garland Science, NY, 4th edition, 2002.

[156] James D. Watson and Francis H. C. Crick. Genetical implications of the structure of deoxyribonucleic acid. *Nature*, 171(4361):964–967, May 1953.

[157] Alexander Vologodskii. DNA extension under the action of an external force. *Macromolecules*, 27(20):5623–5625, September 1994.

[158] Sergei Borukhov and Evgeny Nudler. RNA polymerase holoenzyme: structure, function and biological implications. *Curr Opin Microbiol*, 6(2):93–100, April 2003.

[159] Philip Nelson. *Biological Physics: Energy, Information, Life.* Freeman and Co, NY, 2004.

[160] Jan Lipfert, Sebastian Doniach, Rhiju Das, and Daniel Herschlag. Understanding nucleic acid-ion interactions. *Annu. Rev. Biochem.*, 83:813–841, March 2014.

[161] Dietmar Porschke. Persistence length and bending dynamics of DNA from electrooptical measurements at high salt concentrations. *Biophys. Chem.*, 40(2):169–179, November 1991.

[162] Jean-Louis Barrat and Jean-Francois Joanny. Persistence Length of Polyelectrolyte Chains. *Europhys Lett*, 24(5):333–338, November 1993.

[163] Jean-Louis Barrat and Jean-Francois Joanny. Theory of polyelectrolyte solutions. *Advances in Chemical Physics*, 94:1–66, 1996.

[164] Alexey Savelyev and Garegin A. Papoian. Electrostatic, steric, and hydration interactions favor Na(+) condensation around DNA compared with K(+). *J. Am. Chem. Soc.*, 128(45): 14506–14518, November 2006.

[165] Alexander J. Mastroianni, David A. Sivak, P. L. Geissler, and Paul Alivisatos. Probing the conformational distributions of subpersistence length DNA. *Biophys. J.*, 97(5):1408–1417, September 2009.

[166] Alexey Savelyev, Christopher K. Materese, and Garegin A. Papoian. Is DNA's rigidity dominated by electrostatic or nonelectrostatic interactions? *J. Am. Chem. Soc.*, 133(48): 19290–19293, December 2011.

[167] Alexey Savelyev. Do monovalent mobile ions affect DNA's flexibility at high salt content? *Phys Chem Chem Phys*, 14(7):2250–2254, February 2012.

[168] Onno D. Broekmans, Graeme A. King, Greg J. Stephens, and Gijs J. L. Wuite. DNA Twist Stability Changes with Magnesium(2+) Concentration. *Phys. Rev. Lett.*, 116(25):258102, June 2016.

[169] Aleksander V. Drozdetski, Igor S. Tolokh, Lois Pollack, Nathan Baker, and Alexey V. Onufriev. Opposing Effects of Multivalent Ions on the Flexibility of DNA and RNA. *Phys. Rev. Lett.*, 117(2):028101, July 2016.

[170] Valentin V. Rybenkov, Alexander V. Vologodskii, and Nicholas R. Cozzarelli. The effect of ionic conditions on DNA helical repeat, effective diameter and free energy of supercoiling. *Nucleic Acids Res.*, 25(7):1412–1418, April 1997.

[171] Hergen Brutzer, Nicholas Luzzietti, Daniel Klaue, and Ralf Seidel. Energetics at the DNA supercoiling transition. *Biophys. J.*, 98(7):1267–1276, April 2010.

[172] Sébastien Neukirch. Extracting DNA Twist Rigidity from Experimental Supercoiling Data. *Phys. Rev. Lett.*, 93(19):198107–4, November 2004.

[173] Nicolas Clauvelin, Basile Audoly, and Sebastian Neukirch. Elasticity and electrostatics of plectonemic DNA. *Biophys. J.*, 96(9):3716–3723, May 2009.

[174] Sébastien Neukirch and John F. Marko. Analytical description of extension, torque, and supercoiling radius of a stretched twisted DNA. *Phys. Rev. Lett.*, 106(13):138104, April 2011.

[175] J J Delrow, P J Heath, and J M Schurr. On the origin of the temperature dependence of the supercoiling free energy. *Biophys. J.*, 73(5):2688–2701, November 1997.

[176] Aartjan J. W. te Velthuis, Jacob W. J. Kerssemakers, Jan Lipfert, and Nynke H. Dekker. Quantitative guidelines for force calibration through spectral analysis of magnetic tweezers data. *Biophys. J.*, 99(4):1292–1302, August 2010.

[177] Wesley P. Wong and Ken Halvorsen. The effect of integration time on fluctuation measurements: calibrating an optical trap in the presence of motion blur. *Opt Express*, 14 (25):12517–12531, December 2006.

[178] Jan Lipfert, Daniel A. Koster, Igor D. Vilfan, Susanne Hage, and Nynke H. Dekker. Single-molecule magnetic tweezers studies of type IB topoisomerases. *Methods Mol. Biol.*, 582 (Chapter 7):71–89, 2009.

[179] Scott Forth, Christopher Deufel, Maxim Y. Sheinin, Bryan Daniels, James P. Sethna, and Michelle D. Wang. Abrupt buckling transition observed during the plectoneme formation of individual DNA molecules. *Phys. Rev. Lett.*, 100(14):148301, April 2008.

[180] John F. Marko and Eric D. Siggia. Bending and twisting elasticity of DNA. *Macromolecules*, 27(4):981–988, July 1994.

[181] John F. Marko and Eric D. Siggia. Fluctuations and supercoiling of DNA. *Science*, 265 (5171):506–508, July 1994.

[182] Carlos Bustamante, Zev Bryant, and Steven B. Smith. Ten years of tension: single-molecule DNA mechanics. *Nature*, 421(6921):423–427, January 2003.

[183] Chris A. Brackley, Alexander N. Morozov, and Davide Marenduzzo. Models for twistable elastic polymers in Brownian dynamics, and their implementation for LAMMPS. *J Chem Phys*, 140(13):135103, April 2014.

[184] Rob Phillips, Jane Kondev, Julie Theriot, and Hernan Garcia. *Physical Biology of the Cell.* Garland Science, 2013.

[185] Laszlo Oroszi, Peter Galajda, Huba Kirei, Sandor Bottka, and Pal Ormos. Direct measurement of torque in an optical trap and its application to double-strand DNA. *Phys. Rev. Lett.*, 97(5):058301, August 2006.

[186] Farshid Mohammad-Rafiee and Ramin Golestanian. Elastic correlations in nucleosomal DNA structure. *Phys. Rev. Lett.*, 94:238102, June 2005.

[187] Jayashree Srinivasan, Thomas E. Cheatham, and Piotr Cieplak. Continuum solvent studies of the stability of DNA, RNA, and phosphoramidate– DNA helices. *J. Am. Chem. Soc.*, 120(37):9401–9409, 1998.

[188] Richard Lavery, Krystyna Zakrzewska, David Beveridge, Thomas C. Bishop, David A. Case, Thomas Cheatham, Surjit Dixit, B. Jayaram, Filip Lankas, Charles Laughton, John H. Maddocks, Alexis Michon, Roman Osman, Modesto Orozco, Alberto Perez, Tanya Singh, Nada Spackova, and Jiri Sponer. A systematic molecular dynamics study of nearest-neighbor effects on base pair and base pair step conformations and fluctuations in B-DNA. *Nucleic Acids Res.*, 38(1):299–313, January 2010.

[189] Alberto Marin-Gonzalez, J.G. Vilhena, Ruben Perez, and Fernando Moreno-Herrero. Understanding the mechanical response of double-stranded DNA and RNA under constant stretching forces using all-atom molecular dynamics. *Proc. Natl. Acad. Sci. U.S.A*, 114(27): 7049–7054, July 2017.

[190] Wilma K. Olson, Andrey A. Gorin, Xiang-Jun Lu, Lynette M. Hock, and Victor B. Zhurkin. DNA sequence-dependent deformability deduced from protein-DNA crystal complexes. *Proc. Natl. Acad. Sci. U.S.A*, 95(19):11163–11168, September 1998.

[191] Enrico Carlon, Enzo Orlandini, and Attilio L. Stella. Roles of stiffness and excluded volume in DNA denaturation. *Phys. Rev. Lett.*, 88(19):198101, May 2002.

[192] Filip Lankas, Jiri Sponer, Jörg Langowski, and Thomas E. Cheatham. DNA basepair step deformability inferred from molecular dynamics simulations. *Biophys. J.*, 85(5): 2872–2883, November 2003.

[193] Filip Lankas, Jiri Sponer, Jörg Langowski, and Thomas E. Cheatham. DNA deformability at the base pair level. *J. Am. Chem. Soc.*, 126(13):4124–4125, April 2004.

[194] Nils B. Becker and Ralf Everaers. From rigid base pairs to semiflexible polymers: coarse-graining DNA. *Phys. Rev. E Stat. Nonlin. Soft Matter Phys.*, 76(2 Pt 1):021923, August 2007.

[195] Thomas E. Ouldridge, Ard A. Louis, and Jonathan P. K. Doye. Structural, mechanical, and thermodynamic properties of a coarse-grained DNA model. *J Chem Phys*, 134(8): 085101, February 2011.

[196] James D. Watson and Francis H. C. Crick. Molecular structure of nucleic acids; a structure for deoxyribose nucleic acid. *Nature*, 171(4356):737–738, April 1953.

[197] Rosalind E. Franklin and R. G. Gosling. Molecular configuration in sodium thymonucleate. *Nature*, 171(4356):740–741, April 1953.

[198] Horace R. Drew, Richard M. Wing, Tsunehiro Takano, Christopher Broka, Shoji Tanaka, Keiichi Itakura, and Richard E. Dickerson. Structure of a B-DNA dodecamer: conformation and dynamics. *Proc. Natl. Acad. Sci. U.S.A*, 78(4):2179–2183, April 1981.

[199] Robert M. Clegg, Alastair I Murchie, Annelies Zechel, and David M. J. Lilley. Observing the helical geometry of double-stranded DNA in solution by fluorescence resonance energy transfer. *Proc. Natl. Acad. Sci. U.S.A*, 90(7):2994–2998, April 1993.

[200] Gil Lee, Patricia G. Arscott, Victor A. Bloomfield, and D. Fennell Evans. Scanning tunneling microscopy of nucleic acids. *Science*, 244(4903):475–477, April 1989.

[201] James C. Wang. Variation of the average rotation angle of the DNA helix and the superhelical turns of covalently closed cyclic lambda DNA. *J. Mol. Biol.*, 43(1):25–39, July 1969.

[202] James C. Wang. The degree of unwinding of the DNA helix by ethidium. I. Titration of twisted PM2 DNA molecules in alkaline cesium chloride density gradients. *J. Mol. Biol.*, 89(4):783–801, November 1974.

[203] Michel Duguet. The helical repeat of DNA at high temperature. *Nucleic Acids Res.*, 21(3): 463–468, Februar 1993.

[204] Richard E. Depew and James C. Wang. Conformational fluctuations of DNA helix. *Proc. Natl. Acad. Sci. U.S.A*, 72(11):4275–4279, November 1975.

[205] Sam Meyer, Daniel Jost, Nikos Theodorakopoulos, Michel Peyrard, Richard Lavery, and Ralf Everaers. Temperature dependence of the DNA double helix at the nanoscale: structure, elasticity, and fluctuations. *Biophys. J.*, 105(8):1904–1914, October 2013.

[206] Alexey K. Mazur. On the origin of thermal untwisting of DNA. *J Phys Chem B*, 117(6): 1857–1861, February 2013.

[207] Lauren A. Britton, Wilma K. Olson, and Irwin Tobias. Two perspectives on the twist of DNA. *J Chem Phys*, 131(24):245101, December 2009.

[208] Marie Zgarbová, Jiri Sponer, Michal Otyepka, Thomas E. Cheatham, Rodrigo Galindo-Murillo, and Petr Jurečka. Refinement of the Sugar-Phosphate Backbone Torsion Beta for AMBER Force Fields Improves the Description of Z- and B-DNA. *J Chem Theory Comput*, 11(12):5723–5736, December 2015.

[209] Ivan Ivani, Pablo D. Dans, Agnes Noy, Alberto Perez, Ignacio Faustino, Adam Hospital, Jürgen Walther, Pau Andrio, Ramon Goñi, Alexandra Balaceanu, Guillem Portella, Federica Battistini, Josep Lluis Gelpí, Carlos González, Michele Vendruscolo, Charles A Laughton, Sarah A Harris, David A Case, and Modesto Orozco. Parmbsc1: a refined force field for DNA simulations. *Nat. Methods*, 13(1):55–58, January 2016.

[210] Alberto Perez, Iván Marchán, Daniel Svozil, Jiri Sponer, Thomas E. Cheatham, Charles A Laughton, and Modesto Orozco. Refinement of the AMBER force field for nucleic acids: improving the description of alpha/gamma conformers. *Biophys. J.*, 92(11):3817–3829, June 2007.

[211] Jonathan P. K. Doye, Thomas E. Ouldridge, Ard A. Louis, Flavio Romano, Petr Šulc, Christian Matek, Benedict E. K. Snodin, Lorenzo Rovigatti, John S. Schreck, Ryan M. Harrison, and William P. J. Smith. Coarse-graining DNA for simulations of DNA nanotechnology. *Phys Chem Chem Phys*, 15(47):20395–20414, December 2013.

[212] Benedict E. K. Snodin, Ferdinando Randisi, Majid Mosayebi, Petr Šulc, John S. Schreck, Flavio Romano, Thomas E. Ouldridge, Roman Tsukanov, Eyal Nir, Ard A. Louis, and Jonathan P. K. Doye. Introducing improved structural properties and salt dependence into a coarse-grained model of DNA. *J Chem Phys*, 142(23):234901, June 2015.

[213] Christian Matek, Thomas E. Ouldridge, Adam Levy, Jonathan P. K. Doye, and Ard A. Louis. DNA cruciform arms nucleate through a correlated but asynchronous cooperative mechanism. *J Phys Chem B*, 116(38):11616–11625, September 2012.

[214] Thana Sutthibutpong, Christian Matek, Craig Benham, Gabriel G. Slade, Agnes Noy, Charles Laughton, Jonathan P. K. Doye, Ard A. Louis, and Sarah A. Harris. Long-range correlations in the mechanics of small DNA circles under topological stress revealed by multi-scale simulation. *Nucleic Acids Res.*, 44(19):9121–9130, November 2016.

[215] Sangjin Kim, Erik Broströmer, Dong Xing, Jianshi Jin, Shasha Chong, Hao Ge, Siyuan Wang, Chan Gu, Lijiang Yang, Yi Qin Gao, Xiao-dong Su, Yujie Sun, and X Sunney Xie. Probing allostery through DNA. *Science*, 339(6121):816–819, February 2013.

[216] Tomas Drsata, Marie Zgarbová, Petr Jurečka, Jiri Sponer, and Filip Lankas. On the Use of Molecular Dynamics Simulations for Probing Allostery through DNA. *Biophys. J.*, 110 (4):874–876, February 2016.

[217] Liem X. Dang. Mechanism and thermodynamics of ion selectivity in aqueous solutions of 18-crown-6 ether: a molecular dynamics study. *J. Am. Chem. Soc.*, 117(26):6954–6960, 1995.

[218] Chad W. Hopkins, Scott Le Grand, Ross C. Walker, and Adrian E. Roitberg. Long-Time-Step Molecular Dynamics through Hydrogen Mass Repartitioning. *J Chem Theory Comput*, 11(4):1864–1874, April 2015.

[219] Jean-Paul Ryckaert, Giovanni Ciccotti, and Herman J.C. Berendsen. Numerical integration of the cartesian equations of motion of a system with constraints: molecular dynamics of n-alkanes. *J Comput Phys*, 23(3):327–341, 1977.

[220] Shuichi Miyamoto and Peter A. Kollman. SETTLE: an analytical version of the SHAKE and RATTLE algorithm for rigid water models. *J Comput Chem*, 13(8):952–962, October 1992.

[221] Xiang-Jun Lu and Wilka K. Olson. 3DNA: a software package for the analysis, rebuilding and visualization of three-dimensional nucleic acid structures. *Nucleic Acids Res.*, 31(17): 5108–5121, September 2003.

[222] Richard Lavery, M Moakher, John H Maddocks, D Petkeviciute, and Krystyna Zakrzewska. Conformational analysis of nucleic acids revisited: Curves+. *Nucleic Acids Res.*, 37(17): 5917–5929, September 2009.

[223] John Russo, Piero Tartaglia, and Francesco Sciortino. Reversible gels of patchy particles: role of the valence. *J Chem Phys*, 131(1):014504, July 2009.

[224] Peter Daldrop, Hergen Brutzer, Alexander Huhle, Dominik J. Kauert, and Ralf Seidel. Extending the Range for Force Calibration in Magnetic Tweezers. *Biophys. J.*, 108(10): 2550–2561, May 2015.

[225] Wilma K. Olson, M. Bansal, S.K. Burley, Richard E Dickerson, M. Gerstein, S.C. Harvey, U. Heinemann, Xiang-Jun Lu, S. Neidle, Z. Shakked, H. Sklenar, M. Suzuki, C. S. Tung, E. Westhof, C. Wolberger, and H. M. Berman. A standard reference frame for the description of nucleic acid base-pair geometry. *J. Mol. Biol.*, 313(1):229–237, October 2001.

[226] Tomas Drsata, Kamila Réblová, Ivana Beššeová, Jiri Sponer, and Filip Lankas. rRNA C-Loops: Mechanical Properties of a Recurrent Structural Motif. *J Chem Theory Comput*, 13(7):3359–3371, July 2017.

[227] Brahim Heddi, Christophe Oguey, Christophe Lavelle, Nicolas Foloppe, and Brigitte Hartmann. Intrinsic flexibility of B-DNA: the experimental TRX scale. *Nucleic Acids Res.*, 38(3):1034–1047, January 2010.

[228] Pablo Daniel Dans, Ignacio Faustino, Federica Battistini, Krystyna Zakrzewska, Richard Lavery, and Modesto Orozco. Unraveling the sequence-dependent polymorphic behavior of d(CpG) steps in B-DNA. *Nucleic Acids Res.*, 42(18):11304–11320, October 2014.

[229] Marie Zgarbová, Petr Jurečka, Filip Lankas, Thomas E. Cheatham, Jiri Sponer, and Michal Otyepka. Influence of BII Backbone Substates on DNA Twist: A Unified View and Comparison of Simulation and Experiment for All 136 Distinct Tetranucleotide Sequences. *J Chem Inf Model*, 57(2):275–287, February 2017.

[230] Hendrik Dietz, S. M. Douglas, and W. M. Shih. Folding DNA into twisted and curved nanoscale shapes. *Science*, 325(5941):725–730, August 2009.

[231] Alexander Mario Maier, Wooli Bae, Daniel Schiffels, Johannes Friedrich Emmerig, Maximilian Schiff, and Tim Liedl. Self-Assembled DNA Tubes Forming Helices of Controlled Diameter and Chirality. *ACS Nano*, 11(2):1301–1306, February 2017.

[232] Andreas Gietl, Phil Holzmeister, Fabian Blombach, Sarah Schulz, Lena Voit von Voithenberg, Don C. Lamb, Finn Werner, Philip Tinnefeld, and Dina Grohmann. Eukaryotic and archaeal TBP and TFB/TF(II)B follow different promoter DNA bending pathways. *Nucleic Acids Res.*, 42(10):6219–6231, June 2014.

[233] Stephanie Geggier, Alexander Kotlyar, and Alexander Vologodskii. Temperature dependence of DNA persistence length. *Nucleic Acids Res.*, 39(4):1419–1426, March 2011.

[234] Rosalie P. C. Driessen, Gerrit Sitters, Niels Laurens, Geri F. Moolenaar, Gijs J. L. Wuite, Nora Goosen, and Remus Th. Dame. Effect of temperature on the intrinsic flexibility of DNA and its interaction with architectural proteins. *Biochemistry*, 53(41):6430–6438, October 2014.

[235] Flavia Barone, Luciano Cellai, C. Giordano, Mirella Matzeu, Filomena Mazzei, and Francesco Pedone. γ-Ray footprinting and fluorescence polarization anisotropy of a 30-mer synthetic DNA fragment with one 2-deoxy-7-hydro-8- oxoguanosine lesion. *Eur. Biophys. J.*, 28(8):621–628, January 2000.

List of Figures

List of Tables

Danksagung

Es gibt eine Menge Menschen, denen ich von Herzen dankbar bin für ihre ständige Unterstützung und ihren Glauben an mich. Danke, dass ihr mein Selbstbewusstsein stärkt und mir zeigt, dass ihr mich liebt.

Ein besonderer Dank gilt den Menschen, die mich durch diese Promotion und die Verfassung dieser Doktorarbeit begleitet haben:

Jan

Ich bedanke mich bei Jan, der mir immer ein guter Chef war und mir in den letzten Jahren viel beigebracht hat. Ich bedanke mich für die enge Betreuung und die hohen und perfektionistischen Erwartungen beim Publizieren, die immer zur Verbesserung der Arbeit beigetragen sowie die Qualität gehoben haben. Über eine gute emotionale Ebene gelangt man auf eine ebenso gute sachliche. Dies in der Arbeit vorzufinden ist nicht selbstverständlich.

Ich hatte dieses Glück mit dir. Du hast mir viel Vertrauen entgegen gebracht, mich gestärkt, gefordert und gefördert. Unsere erste gemeinsame Reise nach Amsterdam werde ich immer gerne und in guter Erinnerung behalten. Ich hoffe ihr habt euch bei mir im Auto sicher gefühlt :-) Ebenso unsere Feierabendbiere, gemeinsame Grillfeiern und diverse andere Feste. Schön, dass du die emotionale Ebene zu uns suchst. Vielen Dank!

Dieter

Dieter Braun hat mich sehr früh in seine Arbeitsgruppe aufgenommen und somit den Grundstein für mein wissenschaftliches Interesse gelegt. Ich schätze sein Vertrauen, seine ehrlichen Worte und sein offenes Ohr. Bei ihm habe ich gelernt, dass man alles fragen darf und dass man in der Wissenschaft alles hinterfragen muss, wofür ich sehr dankbar bin.

Prof. Gaub

Ich bedanke mich bei Prof. Gaub für die Unterstützung in den letzten Jahren und die angenehme Atmosphäre in unseren Räumen.

Frau Podolski

Danke, dass Ihre Türe immer offen steht und Sie einen immer willkommen heißen. Mit Ihren schnellen Antworten und Lösungen sind Sie eine große Bereicherung in dieser Fakultät.

Prof. Zacharias

Ich bedanke mich für die gute Zusammenarbeit und freue mich auf weitere Projekte.

Stefanos K. Nomidis, Christian Matek, Filip Lankas, and Enrico Carlon

I thank Stefanos, Christian, Filip, and Enrico for the various simulations they ran for papers or for this thesis and the fruitful discussions we had.

Sabrina Simoncelli and Jochen Feldmann

I thank Sabrina Simoncelli and Jochen Feldmann for the good collaboration and the great paper we are working on.

AG Lipfert

Ein großer Dank geht an Philipp und Thomas, die immer hilfsbereit waren.

Danke Thomas, dass du mich gerade in den letzten Wochen unterstützt hast.

Danke Philipp, dass du mich speziell am Anfang in die Magnetische Pinzette eingearbeitet hast und dass ich immer Hilfe bekommen habe, wenn es um das Setup oder um Auswertungen ging.

Einen herzlichen Dank, dass ihr immer zugehört habt und immer bereit wart zu helfen!

Thank you Willem, for always reminding me why my work was important. It was helpful to have you around to help us refocus on the scientifically relevant questions. Thank you also for fruitful discussions.

Außerdem hat mir die AG Lipfert die Freundschaft zu Stella geschenkt, ein Glück!

LS Gaub

Vielen Dank an Angelika und Tom die mir so oft geholfen haben. Hauptsächlich im Labor aber auch immer mal durch Gespräche über private Anliegen. Ebenso einen großen Dank an Sylvia, die immer aufgeschlossen und bereit zu helfen ist. Ihr seid eine Bereicherung für das gesamte Team.

Ich danke natürlich auch allen anderen, vor allem für die vielen Feste die wir gemeinsam gefeiert haben. Schön, dass es einige hier gibt, die ungern ein Ende finden...

AG Braun

Ich habe mich immer wohl gefühlt in eurer Arbeitsgruppe, wenn auch jetzt nur noch Matzi, Lonzo und Christof übrig geblieben sind. Ich habe viele Personen, die ich schätze, in dieser Gruppe kennen gelernt.

Linda

Ein Glück durften wir damals gleich nach Amsterdam fliegen und konnten den Grundstein für unsere Freundschaft legen. Ich danke dir für deine Ehrlichkeit und Team-Arbeit, die du mir in den letzten Jahren entgegen gebracht hast. Keiner kann sagen wie oft wir beide gemeinsam Mittagessen waren oder Kaffee getrunken haben. Es hätte nur noch gefehlt, dass wir uns in den Meetings Zettel zuschieben oder uns das Pausenbrot teilen (Das haben wir ja sogar gemacht!) :-) Wir haben viele schöne Reisen gemacht und uns immer blind verstanden, das ist nicht selbstverständlich.

Constantin

Danke, dass du so sehr an mich glaubst und mich unterstützt. Ich bin froh in den letzten Jahren so einen guten Freund in dir gefunden zu haben. Ich weiß es zu schätzen, dass du mir immer zuhörst und mit mir Lösungen suchst. Neben den ernsten Themen die wir besprechen, bin ich glücklich so einen Sport- und Essensliebhaber in dir gefunden zu haben. Vielleicht treffen sich unsere Wege beruflich ja wieder. Freundschaftlich werden sie sich jedenfalls nicht mehr trennen!

Manu

Manüüü, kann fliegen wie die Sonne über Fujiama! Deine gute Laune ist ansteckend! Ich weiß, dass du mich immer aufmuntern kannst und es auch schon oft genug getan hast. Deine sportlichen Ambitionen sind mitreißend und deine Ausdrucksweise einmalig. Es tut gut Personen im Leben zu haben, die einem immer wieder daran erinnern wofür das Leben da ist.

Magnus

Magnus ist einer der ehrlichsten und gerechtesten Menschen, die ich kenne. Ich schätze deine Meinung und wünsche dir alles Gute für deine weitere Zeit am Lehrstuhl und darüber hinaus.

Hanna

Die Frau mit dem besten Schreibstil, die nur wenige Sätze braucht um sich auszudrücken, damals wie heute! Danke.

Philip und Flo

Ihr Chaoten sollt auch erwähnt sein! Menschen wie euch braucht man um sich herum!

Ilki und Silki

Die Personen, die ich hier am meisten vermisse: Drilka und Drilke! Danke für eure Unterstützung aus der Ferne. Unsere gemeinsame Zeit hier war toll. Silke, danke dass du so eine gute und zuverlässige Freundin geworden bist! Ilka, du bist und warst schon immer die beste Schwester der Welt. Ich liebe dich unendlich!